The yeast prion domain Sup35 NM models features of human neurodegenerative diseases in vivo

Dissertation

zur

Erlangung des Doktorgrades (Dr. rer. nat.)

der

Mathematisch-Naturwissenschaftlichen Fakultät

der

Rheinischen Friedrich-Wilhelms-Universität Bonn

vorgelegt von

Annika Hornberger

aus

Ludwigshafen am Rhein

Bonn, Januar 2024

Angefertigt mit Genehmigung der Mathematisch-Naturwissenschaftlichen Fakultät

der Rheinischen Friedrich-Wilhelms-Universität Bonn

1. Gutachterin: Prof. Dr. Ina Vorberg

2. Gutachter: Prof. Dr. Jörg Höhfeld

Tag der Promotion: 29.04.2024

Erscheinungsjahr: 2024

Summary

In neurodegenerative diseases, such as prion diseases and Alzheimer's disease, disease-associated proteins misfold and form amyloid deposits that progressively invade the CNS, leading to severe neurodegeneration. Accumulating evidence suggests that amyloid proteins propagate in a prion-like, self-perpetuating manner, but the mechanism of aggregate multiplication in mammals remains unclear. Amyloid deposits are associated with neurodegeneration and can induce a toxic gain-of-function or loss-of-function phenotype. Yet, the contribution of both effects to neurodegeneration is not fully understood. Surprisingly, the same pathogenic protein can aggregate into different structural variants that, similar to prion strains, may cause heterogenous clinical symptoms. However, how the amyloid structure can influence disease progression needs to be elucidated. Previously, our group established the NM-HA mouse model that expresses the hemagglutinin-tagged prion domain NM of the *Saccharomyces cerevisiae* prion Sup35 that behaves like a prion in mammalian cells. As NM does not possess a cellular function in mammals, it can be used to study the gain-of-function of protein aggregates in the absence of loss-of-function effects.

In this project, we used the NM-HA mouse line to investigate the ability of fibril-induced NM-HA aggregates to propagate in the mammalian brain, and thus to model human prion-like proteins. Additionally, we tested if the gain-of-function of intracellular NM-HA aggregates can cause neurodegeneration and compared the disease pathogenesis induced by two different NM fibril conformers. Here we show that the intracranial injection of NM fibrils into NM-HA animals induces progressive NM-HA aggregation, demonstrating that yeast NM prions can replicate in mice. Interestingly, our data points to the involvement of the chaperone valosin-containing protein (VCP) as potential NM prion disaggregase in this process. NM-HA aggregates seeded by the NM fibril variants spread from the hippocampus to similar neuroanatomically connected regions, with striking similarity to pathologies observed in wild type mice challenged with disease-associated protein aggregates. Fibril-injected animals develop mild cognitive decline, likely caused by neuronal loss in hippocampal subregions with prominent NM-HA deposition. Remarkably, neurodegeneration is accompanied by local microgliosis and astrogliosis. Hence, a non-mammalian and non-disease-related protein is able to cause neurodegeneration upon aggregation in mice, likely via a neurotoxic gain-of-function effect. As fibril-injected NM-HA mice recapitulate key aspects of the pathogenesis of human neurodegenerative disorders, our data argue that mechanisms underlying intracellular amyloid fragmentation, dissemination, and toxicity might be shared between amyloidogenic proteins.

Table of Contents

List of Figures

List of Abbreviations

aa	Amino acid
AD	Alzheimer's disease
ALP	Autophagy-lysosomal pathway
ALS	Amyotrophic Lateral Sclerosis
Br	Bregma
BSA	Bovine serum albumin
BSE	Bovine spongiform encephalopathy
CA	Cornu ammonis
CBD	Corticobasal degeneration
CHY	Chymotrypsin
CJD	Creutzfeldt-Jakob disease
CNS	Central nervous system
Cryo-EM	Cryogenic electron microscopy
CTN	C-terminal N domain
DAB	3, 3'-diaminobenzidine
ddH$_2$O	Double distilled H$_2$O
DG	Dentate gyrus
DLB	Dementia with Lewy bodies
dNTP	Deoxynucleotide triphosphate
dpi	Days post injection
E. coli	*Escherichia coli*
EC	Entorhinal cortex
EDTA	Ethylenediaminetetraacetic acid
ERAD	Endoplasmic reticulum-associated degradation
ESC	Embryonic stem cell
EV	Extracellular vesicle
FCS	Fetal calf serum
G	Gauge
GFAP	Glial fibrillary acidic protein
GFP	Green fluorescent protein
GL	Granule layer
GPI	Glycosyl-phosphatidyl-inositol
HA	Hemagglutinin
HD	Huntington's disease
HF	Hippocampal formation
HIP	Hippocampus
HRP	Horseradish peroxidase
Hsp	Heat-shock proteins
HY	Hypothalamus
Iba 1	Ionized calcium binding adaptor molecule 1
IF	Immunofluorescence
IMAC	Immobilized Metal Affinity Chromatography

IPTG	Isopropyl ß-D-1-thiogalactopyranoside
kDa	Kilodalton
KI	Knock-in
KO	Knock-out
LC	Locus coeruleus
LS	Lateral septal nucleus
lx	Lux
MAP2	Microtubule-associated protein 2
mPFC	Medial prefrontal cortex
mpi	Months post injection
MSA	Multiple system atrophy
NDDs	Neurodegenerative diseases
NM	N and M domain of Sup35
NM^{sol}	Soluble NM
NOR	Novel object recognition
OD	Optical density
ON	Overnight
OPR	Oligopeptide-repeat region
ORF	Open reading frame
PAGE	Polyacrylamide gel electrophoresis
PBS	Phosphate buffered saline
PD	Parkinson's disease
PERI	Perirhinal area
PFA	Paraformaldehyde
PFFs	Pre-formed fibrils
PL	Pyramidal layer
PQC	Protein quality control
PrD	Prion-like domain
PrP^C	Cellular prion protein
PrP^{Sc}	Scrapie-associated, pathological prion protein
PVDF	Polyvinylidene difluoride
QNR	QN-rich region
RSP	Retrosplenial cortex
RT	Room temperature
S. cerevisiae	*Saccharomyes cerevisiae*
SD	Standard deviation
SDS	Sodium dodecyl sulfate
SUB	Subiculum
TDP-43	TAR DNA-binding protein 43
TEM	Transmission Electron Microscopy
TH	Thalamus
ThT, ThS	Thioflavin T, S
TRIS	Tris-(hydroxymethyl)-aminomethan
TSE	Transmissible spongiform encephalopathy

UPS	Ubiquitin-proteasome system
v/v	Volume per volume
VCP	Valosin-containing protein
VSV-G	Vesicular stomatitis virus glycoprotein
w/v	Weight per volume
WT	Wild type
x g	Times gravitational acceleration

1 Introduction

1.1 Prion diseases

Prion diseases, or transmissible spongiform encephalopathies (TSEs), are a class of infectious neurodegenerative disorders (NDDs) characterized by the deposition and dissemination of misfolded prion protein within the CNS, resulting in profound neurological impairment and ultimate death (Prusiner, 1998). In humans, TSEs include Creutzfeldt-Jakob disease (CJD), Kuru, Gerstmann-Sträussler-Scheinker syndrome, and fatal familial insomnia. In animals, prion diseases comprise scrapie in sheep, bovine spongiform encephalopathy (BSE) in cattle, chronic wasting diseases in deer, and others. Human TSEs mostly develop sporadically (~85 %), but can also be inherited due to mutations in the prion protein gene (*PRNP),* or can be acquired by exposure to prion-contaminated tissue or material (Collinge, 2001). Some TSEs also possess zoonotic potential, as discovered in the 1990s, when the consumption of BSE-contaminated meat caused variant CJD in humans (Chazot *et al.*, 1996). Clinical manifestations of TSEs in humans include a variety of symptoms, such as progressive dementia, motor dysfunction, and psychiatric disturbances. Typically, TSEs are asymptomatic over many years, but upon clinical onset, the disease progresses rapidly and causes death within weeks to months (Collinge, 2001; Wadsworth and Collinge, 2007). Upon ingestion, prions accumulate in the lymphoreticular system and gradually spread to the CNS and invade the whole brain. Brain tissue from terminally diseased TSE patients displays characteristic prion protein plaques, spongiform vacuolation, neuronal loss, microgliosis, and astrogliosis (Prusiner, 1998; Aguzzi and Calella, 2009). To date, no therapeutic approaches are available to treat or cure TSEs.

At the molecular level, prion diseases are characterized by the misfolding and conformational conversion of the cellular prion protein (PrP^C) into its pathological prion isoform PrP^{Sc}. It is now widely accepted that PrP^{Sc} is the sole agent causing TSEs as proposed by the "protein-only" hypothesis (Bolton *et al.*, 1982; Prusiner, 1982). Native PrP^C is rich in α-helices (~40 %) and is attached to the plasma membrane of neurons and glia via its glycosyl-phosphatidyl-inositol (GPI) anchor. It regulates numerous, yet unclear cellular processes, such as cell signaling, cell proliferation, and cell cycle regulation (Soto *et al.*, 2006; Wulf *et al.*, 2017). Unlike PrP^C, PrP^{Sc} is a homopolymer rich in β-sheets (~45 %). Aggregation occurs through the alignment of PrP^{Sc} β-sheets, resulting in highly structured and stable cross-β fibrils, in which the β-sheets are organized perpendicular to the fibril axis (figure 1) (Eanes and Glenner, 1968). These so-called amyloid fibrils are resistant to proteolytic cleavage and most denaturing conditions. They can be stained using amyloid dyes, such as Congo red or

thioflavin S and T (Collinge, 2001; Westermark, 2005). Prions propagate by a self-replicating process termed "seeded polymerization" (figure 1) (Jarrett and Lansbury, 1993; B. Caughey *et al.*, 1995). According to this model, initial PrP^{Sc} forms spontaneously from PrP^{C} in a slow, rate-determining step via an intermediate fold that assembles into small PrP^{Sc} oligomers. These oligomers then rapidly recruit monomeric PrP^{C} by catalyzing the misfolding of PrP^{C} into PrP^{Sc} to ultimately adopt a highly structured amyloid fold. Continuous elongation finally leads to the formation of large amyloid fibrils. It is hypothesized that, for efficient prion replication, fibrils are fragmented into short infectious seeds by as yet unknown mechanisms. These seeds in turn recruit and convert PrP^{C} and propagate the PrP^{Sc} phenotype (Soto *et al.*, 2006; Aguzzi and Calella, 2009). In addition, infectious entities are transmitted to neighboring cells, in which they induce PrP^{Sc} aggregation. This instigates a self-perpetuating prion infection that progressively spreads throughout the whole brain (Weissmann *et al.*, 2002).

| PrP^{C} Monomer | PrP^{Sc} Oligomer | Monomer recruitment + Fibril elongation | Amyloid fibril | Fragmentation + Seeding |
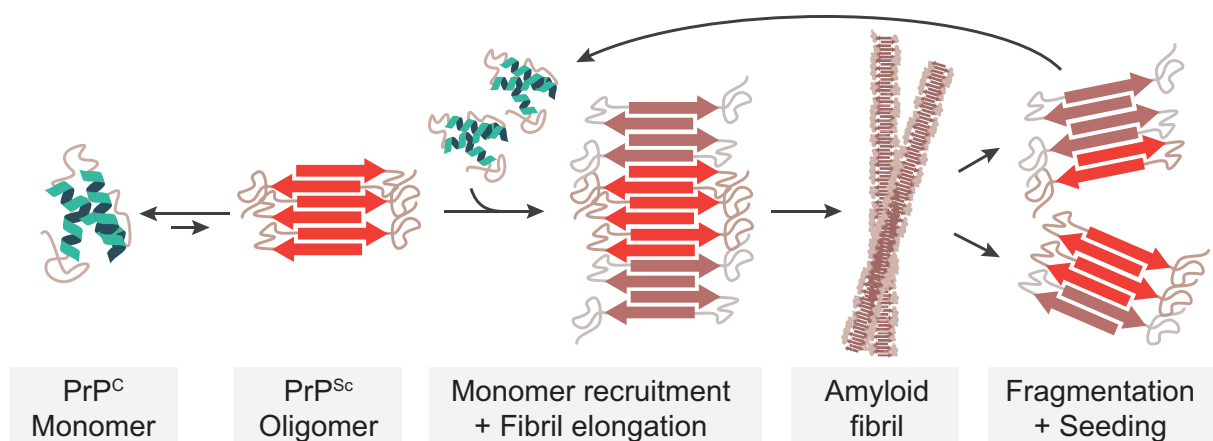
Figure 1. The seeded polymerization model of prion replication. In a slow process, native PrP^{C} spontaneously misfolds to an intermediate state that adopts the pathological β-sheet-rich PrP^{Sc} conformation and generates a short oligomer. The oligomer rapidly expands by recruiting more homotypic protein through conversion of PrP^{C} into PrP^{Sc}. This leads to the formation of large amyloid fibril, in which β-sheets are organized perpendicular to the fibril axis. For prion replication, fibrils likely are fragmented into short seeds that serve as new nucleation sites. Prion spreading is achieved by seed transmission to neighboring cells.

1.2 Amyloid associated with human neurodegenerative disorders

The deposition of amyloid in the CNS, accompanied by progressive neuronal loss, is not exclusive to prion diseases but is also a feature of other human NDDs. Each of these amyloidosis is characterized by the misfolding of one or more specific proteins, such as tau and amyloid-β in Alzheimer's disease (AD), α-synuclein in Parkinson's disease (PD), huntingtin in Huntington's disease (HD), or TAR DNA-binding protein 43 (TDP-43) in amyotrophic lateral sclerosis (ALS) (Soto, 2003; Jucker and Walker, 2018). AD is the most common NDD in

humans and its sporadic form is characterized by late-onset progressive dementia and decline in cognitive functions, caused by the degeneration of neurons in the hippocampus and basal forebrain (DeTure and Dickson, 2019). In the brain, patients gradually develop extracellular plaques consisting of misfolded amyloid-β and intracellular neurofibrillary tangles made of aggregated tau. Alike PrP^{Sc}, pathological amyloid-β and tau have amyloid structures that stain with amyloid-binding dyes (Eisenberg and Jucker, 2012). In its native form, tau binds to and stabilizes microtubules, but in disease it becomes hyperphosphorylated and prone to aggregation (V. M. Lee *et al.*, 2001). Amyloid tau is also found in other NDDs, termed tauopathies, that include corticobasal degeneration (CBD), Pick's disease, and progressive supranuclear palsy. Although all caused by aggregation of tau, tauopathies are very heterogeneous and differ in clinical symptoms, neuropathological patterns of tau deposition, and tau amyloid morphologies (Crowther and Goedert, 2000).

PD is the second most prevalent NDD after AD and manifests as movement disorder with resting tremors (involuntary movement), bradykinesia (slowed movement), and muscle rigidity (Herva and Spillantini, 2015). Main cause is the progressive degeneration of dopaminergic neurons in the substantia nigra in the midbrain. There, neurons accumulate α-synuclein that forms cytoplasmic or neuritic amyloid inclusions termed Lewy bodies or Lewy neurites (Spillantini *et al.*, 1997). Native α-synuclein is mainly found in presynaptic terminals of neurons, where it is involved in the vesicles trafficking and synaptic plasticity. However, its exact functions remain unclear (Burré, 2015). The deposition of α-synuclein is also a feature of other so-called synucleinopathies, such as dementia with Lewy bodies (DLB) and multiple system atrophy (MSA). Alike tauopathies, synucleinopathies strongly differ in neuropathological lesions and disease phenotypes (Hoppe *et al.*, 2021).

These examples emphasize that multiple proteins with different structures can adopt amyloid conformations and cause NDDs with diverse clinical phenotypes (Chiti and Dobson, 2006). Similar to TSEs, non-prion amyloidosis develop after a long asymptomatic phase. However, after first symptoms, they progress more slowly and less dramatically than TSEs. Most importantly, TSEs in animals can be contagious, as PrP^{Sc} can be transmitted naturally between individuals. For example in deer, transmission occurs by the oral uptake of prion-contaminated urine, saliva, and feces (Gilch *et al.*, 2011). So far, transmission of AD and PD from one human to another has not been demonstrated, hence, these diseases are not considered infectious (Scheckel and Aguzzi, 2018).

1.3 Prion-like properties of amyloidogenic proteins

It is now widely accepted that NDD-associated proteins have prion-like properties and can propagate in a self-replicating manner. First hints came from the analysis of brain tissue from AD and PD patients that demonstrated the spatio-temporal dissemination of pathological tau, amyloid-β and α-synuclein in the brain (Braak and Braak, 1991, 1995; Braak *et al.*, 2003). According to the Braak staging, tau deposits in AD arise in the locus coeruleus (brain stem) and entorhinal cortex (hippocampal formation) (stages I-II) before invading the hippocampus and large cortical areas at later disease stages (stages III-VI) (figure 2 A). Affected neurons in targeted brain regions degenerate, causing the AD-typical dementia (Goedert, 2015). This non-diffuse spreading pattern suggests a specific cell-to-cell propagation and continuous replication of pathogenic amyloid. Since then, a growing number of studies have provided strong evidence for the prion-like induction, replication, and intercellular dissemination of various disease-associated amyloid, such as tau, α-synuclein, and TDP-43, in cell systems
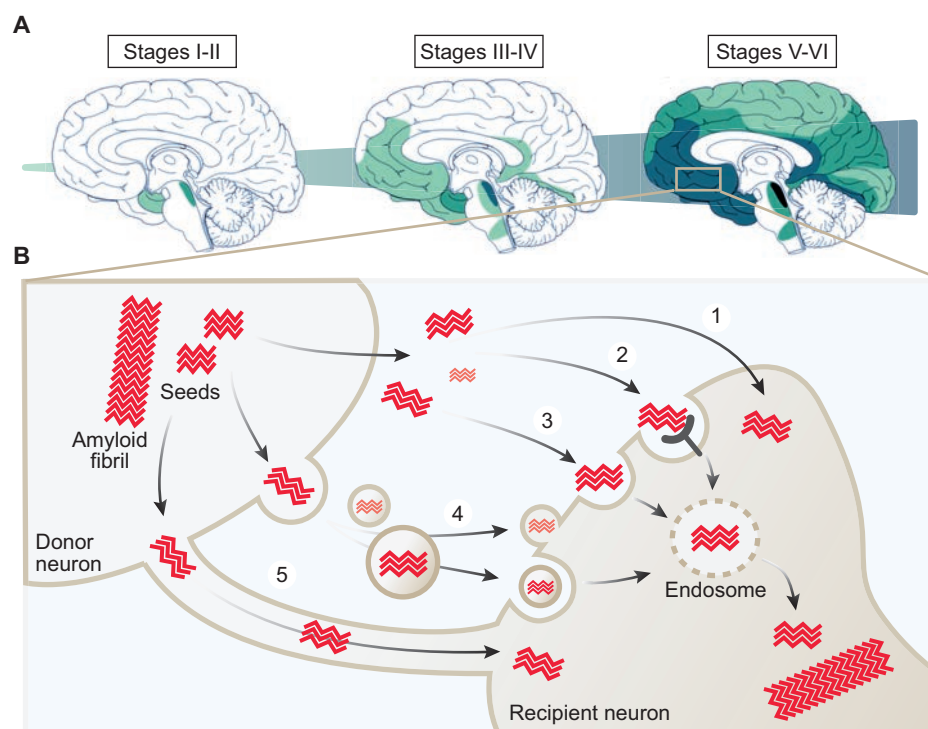
Figure 2. Amyloidogenic proteins disseminate in the brain in a prion-like manner. A Dissemination of tau aggregates in the brain according to the Braak stages. Tau accumulations develop in the locus coeruleus and entorhinal cortex (stages I-II) before entering the hippocampal formation (stages III-IV) and large parts of the cortex (stages V-VI). Image modified from Goedert *et al.,* 2015. **B** Amyloid transmission routes from a donor to a recipient neuron. Infectious entities can be transmitted via diffusion (1), receptor-mediated endocytosis (2), or macropinocytosis (3). Seeds can also be released in extracellular vesicles (4) or be transferred via tunneling nanotubes connecting both neurons (5).

and *in vivo*. In line with the seeded polymerization model (figure 1), exogenous seeds of the pathologic protein induce intracellular aggregates of homotypic protein in cells and

subsequent transmission of the aggregated state to bystander cells (Luk *et al.*, 2009; J. L. Guo and Lee, 2011; Hansen *et al.*, 2011; Kaufman *et al.*, 2016; Smethurst *et al.*, 2016). Similarly, intracranial injection of amyloid seeds in living animals induces homotypic amyloid formation and a time-dependent propagation of the amyloid conformation to synaptically connected brain regions (Luk *et al.*, 2012a; Clavaguera *et al.*, 2013; Prusiner *et al.*, 2015; J. L. Guo *et al.*, 2016; Porta *et al.*, 2018). Several routes of trans-synaptic transmission have been proposed for amyloid tau, α-synuclein, and PrP^{Sc} that may be shared (figure 2 B). Recent findings indicate that tau and α-synuclein seeds are released from neurons via exocytosis and freely enter the extracellular space (figure 2 B, 1) (Tapiola *et al.*, 2009; Mollenhauer *et al.*, 2013). The recipient cell can take up seeds either directly through the plasma membrane or upon seed binding to receptors, such as heparan sulfate proteoglycans (PrP^{Sc}, tau, α-synuclein) or lymphocyte activation gene 3 (α-synuclein) (figure 2 B, 2) (Holmes *et al.*, 2013; Mao *et al.*, 2016). Intracellular uptake may then be mediated via receptor-mediated endocytosis and macropinocytosis (figure 2 B, 3) (Vella *et al.*, 2007; Desplats *et al.*, 2009; Frost *et al.*, 2009). Furthermore, data from cell systems suggest the release of seeds via extracellular vesicles (EVs) that fuse with the plasma membrane of the recipient cell (figure 2 B, 4) (Vella *et al.*, 2007; Danzer *et al.*, 2012; Saman *et al.*, 2012). Lastly, tunneling nanotubes have been proposed to be involved in seed transmission (figure 2 B, 5) (Gousset *et al.*, 2009; Abounit *et al.*, 2016). In the recipient neuron, amyloid formation is seeded in the cytosol. Although a fraction of seeds accesses the cytosol directly, most internalized seeds enter the endolysosomal pathway for lysosomal degradation (Karpowicz *et al.*, 2017). Recent data suggests that seeds escape the endosome or lysosome via aggregate-mediated membrane rupture (Flavin *et al.*, 2017), however the exact mechanism remains to be determined.

1.4 Amyloidogenic proteins can form distinct strains

It has early been discovered that prions, when inoculated into the brain of animals, cause different disease phenotypes with different incubation times, clinical signs, and neuropathological lesions (Bessen and Marsh, 1992b). These phenotypes remained consistent across serial passages, and the associated prion variants have been referred to as "strains". *In vitro* analyses of these strains revealed distinct biochemical properties, such as different glycosylation patterns, proteolytic profiles on Western blot after protease K digestion, or resistance to denaturation with chaotropic agents (Bessen and Marsh, 1992a; Collinge *et al.*, 1996). This suggested that prion strains are defined by distinct folds or conformations of PrP^{Sc} and led to the prion strain hypothesis, which states that PrP^{Sc} can

adopt multiple conformations, each causing a unique neuropathology and disease phenotype (figure 3 A). Although this hypothesis has long remained unproven, recent advances in prion purification from brain tissue and cryogenic electron microscopy (cryo-EM) revealed the structure of hamster- and mouse-adapted PrP^{Sc} strains on a molecular level. These data demonstrated that these prion strains are characterized by distinct PrP^{Sc} folds (Kraus *et al.*, 2021; Manka *et al.*, 2022; Manka *et al.*, 2023). Hence, a protein with the same primary sequence can fold into different amyloid conformations and cause different disease phenotypes. Remarkably, the strain phenomenon of prion diseases has also been extended to other NDDs. Accumulating evidence suggests that the disease heterogeneity of human tauopathies and synucleinopathies is caused by different conformers of amyloid tau or α-synuclein, respectively. First support for α-synuclein strains came from *in vitro* studies, in which distinct α-synuclein polymorphs were generated under different salt concentrations
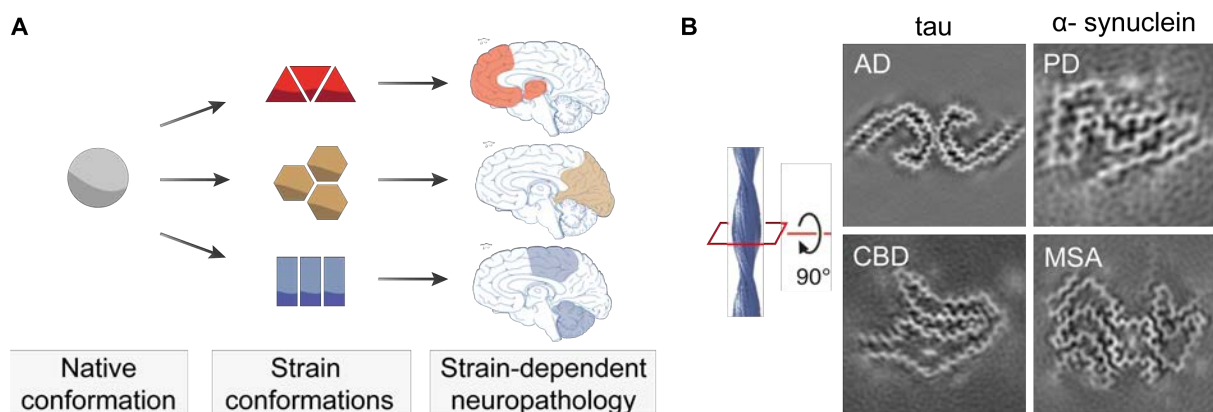
Figure 3. The strain hypothesis of prions and non-prion amyloidogenic proteins. A According to the strain hypothesis, PrP^{Sc} can adopt different conformations that cause distinct neuropathological lesions and disease phenotypes. It is now widely accepted that also other amyloidogenic proteins, such as tau, amyloid-ß, synuclein, and TDP-43, fold into disease-specific structures. **B** Cryo-EM maps of filamentous tau (left panels) and α-synuclein (right panels) isolated from patients with AD (Falcon *et al.,* 2018), CBD (Zhang *et al.,* 2020), PD (Schweighauser et al., 2020), and MSA (Yang *et al.,* 2022). Each disease is characterized by a distinct amyloid conformation that also can include paired filaments (AD, MSA). Images show cross-sections of reconstructed filaments, perpendicular to fibril axis.

(Bousset *et al.*, 2013). In the following years, various *in vivo* studies demonstrated that the intracerebral inoculation of tau and α-synuclein aggregates isolated from patient's brains reproduced similar aggregate morphologies and caused distinct clinical phenotypes and different deposition patterns in mice (Luk *et al.*, 2012b; Clavaguera *et al.*, 2013; Masuda-Suzukake *et al.*, 2013; Prusiner *et al.*, 2015; Narasimhan *et al.*, 2017). Recently, cryo-EM has been used to resolve the structures of many tau and α-synuclein aggregate variants (figure 3 B) (Fitzpatrick *et al.*, 2017; Falcon *et al.*, 2018; Falcon *et al.*, 2019; Schweighauser *et al.*, 2020; W. Zhang *et al.*, 2020; Yang *et al.*, 2022). These data confirmed that each tauopathy is

characterized by an individual tau fold that is identical between patients with the same disease (Scheres *et al.*, 2020). Interestingly, the structure of α-synuclein variants differs between PD and MSA but is identical between PD and DLB (Yang *et al.*, 2022). Future studies will reveal more structures of protein aggregates associated with other NDDs. However, it is crucial to identify the factors that determine the formation of these specific folds and how they cause different disease phenotypes. For tau, it has been proposed that the isoform composition and post-translational modifications influence the amyloid structure (Arakhamia *et al.*, 2020), but for other amyloidogenic proteins this remains unclear.

1.5 Toxic loss-of-function and gain-of-function of intracellular amyloid

Intracellular protein aggregates have been associated with neurodegeneration, but the exact mechanisms underlying amyloid-induced neurotoxicity remain enigmatic. According to the loss-of-function hypothesis, neurons degenerate in response to the partial loss of the native function of the aggregating protein. For example, hyperphosphorylation and aggregation of tau leads to the destabilization of microtubules, resulting in impaired axonal transport (Feinstein and Wilson, 2005; Cowan *et al.*, 2010). In line with this, tau knock-out (KO) mice develop cognitive and motor deficits with age, suggesting that tau is necessary for proper brain function (Lei *et al.*, 2014). However, it is believed that the functional loss is accompanied by the acquisition of neurotoxic functions (gain-of-function) of the protein aggregate that contribute to neurodegeneration. Remarkably, accumulating evidence suggests that it is small, soluble oligomers, rather than large protein aggregates, that drive neurotoxicity. This includes intracellular oligomers of tau, α-synuclein, and TDP-43, but also extracellular oligomers of amyloid-β and PrP^{Sc} (Brunden *et al.*, 2008; B. Caughey *et al.*, 2009; Kayed and Lasagna-Reeves, 2013; Fang *et al.*, 2014). This is supported by data showing that synaptic loss, cognitive decline, and neurodegeneration appear to precede tau neurofibrillary tangles in AD mouse models and post-mortem studies of human AD (Gómez-Isla *et al.*, 1997; Yoshiyama *et al.*, 2007; Polydoro *et al.*, 2009). Additionally, injecting tau oligomers, but not monomer or fibrils into the brain of WT mice led to cognitive decline, loss of synapses, and mitochondrial dysfunction (Lasagna-Reeves *et al.*, 2011). Furthermore, the expression of oligomer-forming variants of α-synuclein in rat brain caused increased neurotoxicity compared to fibrillar α-synuclein (Winner *et al.*, 2011). Within the cell, various mechanisms of oligomer and aggregate-associated toxicity have been proposed that may be shared between different pathogenic proteins. In addition to mechanical stress caused by large, rigid aggregates, hydrophobic residues at the tips of oligomers can interact with lipid membranes,

leading to the rupture of intracellular organelles or pore formation in the plasma membrane (Lashuel *et al.*, 2002; Laganowsky *et al.*, 2012; Pieri *et al.*, 2012). This may result in ion dyshomeostasis, neuron depolarization, oxidative stress with reactive oxygen species, and mitochondrial dysfunction (Byron Caughey and Peter T. Lansbury, 2003; H. Zhang *et al.*, 2021; Cascella *et al.*, 2022). In addition, α-synuclein and amyloid-β oligomers have been suggested to cause endoplasmic reticulum stress, and to impair the proteostasis network by directly inhibiting the proteasome (Lindersson *et al.*, 2004; Jiang *et al.*, 2010; Thibaudeau *et al.*, 2018). It is believed that cells, to protect themselves, sequester toxic protein species and store them in large protein deposits. Hence, intracellular aggregates may have a beneficial effect for cells (Alonso Adel *et al.*, 2006). However, these large protein deposits can in turn physically hinder cellular and axonal transport and sequester essential cellular components, such as chaperones or proteasomes (Ballatore *et al.*, 2007; Louros *et al.*, 2023). This may lead to impaired protein homeostasis and to the mislocalization and functional loss of other essential cellular components (Riemenschneider *et al.*, 2022).

1.6 Neuroinflammation in NDD pathogenesis

NDDs are characterized by chronic neuroinflammation, such as microgliosis and astrogliosis, in brain regions containing protein deposits (McGeer *et al.*, 1988; McGeer *et al.*, 1989; Liddelow *et al.*, 2017). Accumulating evidence points to a central role for neuroinflammation in disease pathogenesis, and the involved mechanisms are gradually being elucidated. Inflammation in the brain is regulated by, among others, microglia and astroglia, the resident immune cells of the CNS that maintain brain homeostasis. Microglia are brain macrophages that, in their quiescent state, continuously survey their microenvironment with their processes, contributing to synaptic plasticity and tissue homeostasis (Nimmerjahn *et al.*, 2005). Astrocytes are the most abundant glia cells in the brain and provide vital support to neuronal function by regulating neurotransmitter levels, offering metabolic support, and contributing to the formation and maintenance of the blood-brain-barrier (Sofroniew and Vinters, 2010). Upon an insult, microglia and astrocytes become activated and help to restore tissue homeostasis by repairing or removing cellular debris, dead cells, or other toxic agents. In their pro-inflammatory state, microglia change from a highly-branched phenotype to an unbranched, amoeboid state. In addition, microglia release pro-inflammatory cytokines that recruit more glia to the insulted area (S. Hickman *et al.*, 2018). Astrocytes become activated in a process termed reactive astrogliosis. In this state, astroglia express high amounts of glial-fibrillary protein (GFAP) and release pro-inflammatory cytokines and other signaling molecules

(Sofroniew and Vinters, 2010). While inflammation in general can be beneficial, a prolonged inflammatory response has a detrimental effect and can lead to neuronal loss and tissue damage (Kempuraj *et al.*, 2016).

Neuroinflammation in AD and PD occurs before neurons die, suggesting that glia become activated in early disease stages (Gerhard *et al.*, 2006; Yoshiyama *et al.*, 2007; Heneka *et al.*, 2015). Activated microglia were found to surround extracellular amyloid-β plaques, presumably to clear them by phagocytosis (Frautschy *et al.*, 1998). It has been shown that microglia bind directly to amyloid-β fibrils via specific receptors and then become active, triggering an inflammatory response (Bamberger *et al.*, 2003). This interaction may initiate a vicious cycle that further promotes the aggregation and spread of amyloid-β. In addition, it likely induces neurodegeneration due to the continuous release of pro-inflammatory cytokines and other neurotoxic molecules (S. E. Hickman *et al.*, 2008; Venegas *et al.*, 2017). Microglia also take up amyloid tau for degradation (Bolós *et al.*, 2016). However, microglial activation was shown to also enhance tau hyperphosphorylation, which in turn promotes the formation of tau deposits (D. C. Lee *et al.*, 2010). In PD, microglia may act via a similar mechanism. Activated microglia are found in the substantia nigra of PD patients, where they surround extracellular α-synuclein deposits and contain engulfed α-synuclein (McGeer *et al.*, 1988; Stokholm *et al.*, 2017). Accumulating evidence suggests that the activation of microglia and the release of pro-inflammatory cytokines attracts and activates astroglia (D. Zhang *et al.*, 2010; Liddelow *et al.*, 2017). Reactive astrocytes have been found around amyloid-β deposits in AD and α-synuclein aggregates in PD (Wakabayashi *et al.*, 2000; Medeiros and LaFerla, 2013). Additionally, astroglia can take up amyloid tau and α-synuclein and thereby might contribute to tau dissemination in the brain (Puangmalai *et al.*, 2020). Like microglia, astroglia release potentially neurotoxic molecules, such as cytokines and nitric oxide, potentiating the inflammatory response and potentially accelerating disease progression (D. Zhang *et al.*, 2010; Reid *et al.*, 2020).

1.7 The cellular protein quality control system

A balanced proteome, the collective of cellular proteins, is a prerequisite for viable cells and is particularly important for post-mitotic cells, such as neurons. To maintain protein homeostasis, or proteostasis, cells rely on a complex protein quality control (PQC) machinery that regulates protein folding and refolding, as well as degradation and sequestration of misfolded proteins (Balch *et al.*, 2008). Central to these processes are molecular chaperones, the ubiquitin-proteasome system (UPS), and the autophagy-lysosomal pathway (ALP). Ageing

is associated with the functional decline of the proteostasis network, leading to the accumulation of misfolded aggregation-prone proteins (Morley *et al.*, 2002; Taylor and Dillin, 2011). In addition to inducing neurotoxic gain-of-function effects, these protein deposits also overload the PQC machinery, promoting the development of NDDs (Douglas and Dillin, 2010).

Molecular chaperones are the key players in protein folding, refolding, transport, and proteolytic degradation. They also prevent protein aggregation by interacting with and blocking of hydrophobic amino acid patches typically exposed by misfolded or fibrillar proteins (Hartl and Hayer-Hartl, 2009). While certain chaperones assist *de novo* protein folding during translation, heat-shock proteins (Hsps) are expressed in response to cellular stress. Hsps have direct implications in NDDs, as chaperones of the Hsp70 subfamily have been shown to interact with oligomeric tau and α-synuclein to prevent the formation of toxic species (Muchowski and Wacker, 2005; Patterson *et al.*, 2011). Additionally, Hsp70 members have been proposed to catalyze the disaggregation of tau fibrils in an ATP-dependent manner together with co-chaperones Hsp40 and Hsp110 (Nachman *et al.*, 2020). Furthermore, chaperones Hsp70 and Hsp90 target misfolded proteins to induce ubiquitylation and to mark the protein for degradation via the UPS or ALP (Shiber and Ravid, 2014).

The degradation of aberrant protein in the cell is controlled by the ALP and the UPS. While the UPS catalyzes the degradation of soluble, short-lived proteins that resist refolding by chaperones, the ALP, specifically macroautophagy, is involved in the degradation of large protein aggregates and aged organelles (Ciechanover, 2006). During macroautophagy, cytosolic cargo is engulfed by a double-membraned autophagosome which fuses with lysosomes for enzymatic digestion of the content. ALP cargo is marked by the autophagy marker p62, which targets ubiquitinylated proteins, including amyloid tau and α-synuclein (Kuusisto *et al.*, 2001). ALP impairment has been reported in multiple NDDs and includes lysosomal dysfunction in AD and PD (Nixon, 2013). Degradation via the UPS requires protein ubiquitylation at lysine residues. Upon recruitment to the 26S proteasome, the target protein is unfolded and channeled through the cylindric 20S core, which catalyzes proteolytic cleavage (Dikic, 2017). UPS impairment is common to many NDDs and intracellular protein deposits typically include ubiquitin. Examples are Lewy bodies in PD, neurofibrillary tangles and amyloid-β plaques in AD, and aggregated huntingtin in HD (Cole and Timiras, 1987; Kuzuhara *et al.*, 1988; DiFiglia *et al.*, 1997). Several mechanisms of proteasomal impairment have been proposed, such as blocking of the 20S core unit by large protein aggregates, sequestration of proteasomes within protein deposits, or impaired protein ubiquitylation (Deriziotis *et al.*, 2011; Zheng *et al.*, 2016; Q. Guo *et al.*, 2018).

1.8 Prions of lower eukaryotes

Amyloidogenic proteins are not exclusive to mammals, but have also been identified in the phylogenetic kingdom of fungi, specifically in the baker's yeast *Saccharomyces cerevisiae*. After the publication of the "protein-only" hypothesis of prions (Prusiner, 1982), Wickner proposed in 1994 that two non-mendelian heritable traits in yeast resulted from the conversion of the proteins Ure2 and Sup35 into their prion isoforms [URE3] and [PSI$^+$] (Wickner, 1994). [URE3] and [PSI$^+$] formation mimicked a loss-of-function phenotype in yeast that was inherited via the cytosol. Additionally, prion propagation was inhibited by depleting Ure2 and Sup35 expression and was increased by their overexpression (Wickner, 1994). Together with the polymerization of Sup35 into [PSI$^+$]-associated oligomers (Paushkin *et al.*, 1996), these results strongly argued for a prion-like mechanism of [URE3] and [PSI$^+$] propagation. Since then, more yeast proteins have been discovered that share these features, such as [PIN$^+$] or [SWI$^+$] (Derkatch *et al.*, 1997; Du *et al.*, 2008). Interestingly, while some fungal prions exhibit beneficial functions (Dalstra *et al.*, 2003), the role of [URE3], [PSI$^+$], and [PIN$^+$] prions is unclear. It is argued that most prion phenotypes are - alike PrP^{Sc}- toxic, lethal, or lead to reduced growth (McGlinchey *et al.*, 2011). However, a small proportion of wild yeast populations contains [PSI$^+$] and [PIN$^+$] prions (Halfmann *et al.*, 2012). It is therefore possible that, in rare cases, the prion phenotype provides a certain advantage in a changing environment (True and Lindquist, 2000). Similar to PrP^{Sc}, yeast prions assemble into highly-ordered cross-β aggregates (Shewmaker *et al.*, 2006; Wickner *et al.*, 2008). The core of these amyloid is formed by a glutamine (Q) and asparagine (N) QN-rich sequence termed prion domain (PrD), which is found in many yeast prions (Ross *et al.*, 2005b; Liebman and Chernoff, 2012). PrDs are intrinsically disordered, low-complexity domains rich in polar, uncharged amino acid residues. Scrambling the residues within the PrD does not impair prion induction, demonstrating that the prion-forming ability is dependent on the amino acid composition but not on the exact sequence (Ross *et al.*, 2005a). In yeast, prions can form *de novo* by spontaneous assembly (Chernoff *et al.*, 1993). Alternatively, prions can be induced *in vitro* and *in vivo* via exogeneous prion seeds generated from homotypic protein, which ultimately proves the "protein-only" hypothesis (C. Y. King and Diaz-Avalos, 2004; Tanaka *et al.*, 2004). Once the prion phenotype is established, it persists and is propagated in a self-perpetuating manner via seeded polymerization, alike mammalian prions. Amyloid fragmentation and seed formation in yeast is mainly mediated by the chaperone Hsp104. Hsp104 is a AAA$^+$ ATPase that works together with chaperones Hsp70 and Hsp40 to extract single monomers from within an amyloid fibril (J. R. Glover and Lindquist, 1998; Tipton *et al.*, 2008; Mogk *et al.*, 2015). This causes the fibril to break into small seeding-competent, infectious species that

transmit the prion phenotype (Kryndushkin *et al.*, 2003). Interestingly, depletion as well as overexpression of Hsp104 eliminates the [PSI⁺] phenotype, emphasizing its crucial role for [PSI⁺] prion replication (Chernoff *et al.*, 1995). Finally, induced prions are transmitted vertically to offspring by cell division (Liebman and Chernoff, 2012). To date, no homologue of Hsp104 has been described in the mammalian cytosol and the mechanism of chaperone-mediated amyloid disassembly in mammalian cells remains to be elucidated.

1.9 The yeast prion Sup35

Of the various yeast prions, Sup35 and its prion form [PSI⁺] have been the subject of most research. Discovered in 1965, Sup35 regulates the termination of mRNA translation. Upon aggregation to [PSI⁺], this function is lost, leading to a nonsense-suppression phenotype caused by increased readthrough at stop codons (Cox, 1965). The native Sup35 consists of three domains: The N, M, and C domain (figure 4). The N domain is the PrD and contains a QN-rich region (QNR, aa 1-39), crucial for amyloid induction and assembly in yeast (DePace *et al.*, 1998). The oligopeptide-repeat region (OPR, aa 40-97) also contains polar residues but in addition comprises 5 and a half oligopeptide repeats. In yeast, the OPR mediates prion propagation by interacting with Hsp104 (Shkundina *et al.*, 2006). Interestingly, a similar OPR is also found in the N-terminus of PrP, however its exact function is unclear. The OPR is followed by the C-terminal N domain (CTN, aa 98-123), which is also rich in N and Q. In contrast to the N domain, the middle M domain (aa 123-253) is highly charged and regulates the solubility of native Sup35 and the stability of the [PSI⁺] phenotype during mitosis. Finally,
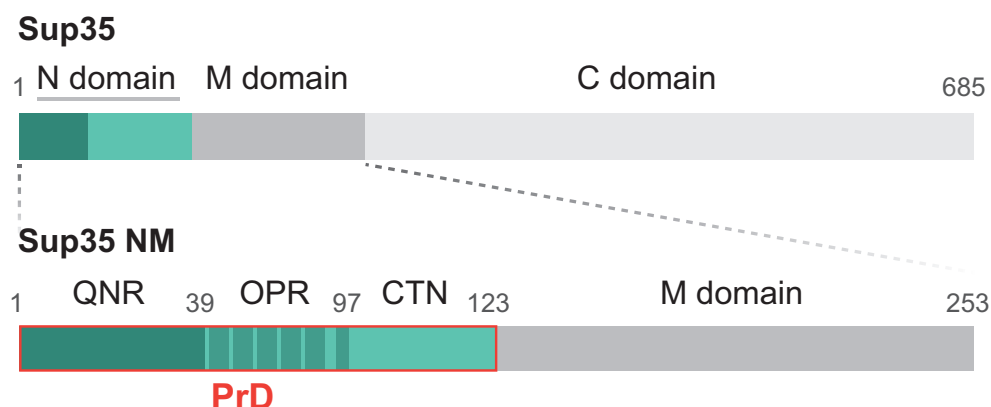
Figure 4. Subdomains of the yeast prion Sup35. Native Sup35 (top) consists of the N, M, and catalytic C domain that regulates translation termination. Expression of the N and M subdomains in yeast (Sup35 NM, bottom) is sufficient to induce the [PSI⁺] phenotype. The N domain or prion domain (PrD) mediates prion formation and amyloid assembly and comprises the glutamine (a) and asparagine (N) rich region (QNR), the oligopeptide repeat region (OPR), and the C-terminal N domain (CTN). The highly charged middle M domain regulates protein solubility. Numbers indicate amino acids.

the catalytic C domain (aa 254-685) executes the translation termination function, but is dispensable for prion formation (John R. Glover *et al.*, 1997; J. J. Liu *et al.*, 2002). Consequently, the expression of the N and M subdomains (Sup35 NM) is sufficient to induce and propagate the [PSI$^+$] phenotype (Patino *et al.*, 1996). Hence, Sup35 NM has been used to study amyloid formation and propagation in yeast. Strikingly, Sup35 NM and other yeast prions can assemble into multiple different [PSI$^+$] variants, identical to strains of mammalian PrP^{Sc} (Derkatch et al., 1996). Structural analysis of Sup35 NM aggregate variants revealed differences in amyloid morphology and conformation, biophysical properties, and the ability to generate seeds. Weak variants usually contain less seeds, strong variants propagate high amounts of seeds (Tanaka *et al.*, 2006; Toyama *et al.*, 2007). Hence, conformationally distinct prion variants induce different phenotypes in yeast, which closely resembles features of mammalian prions and prion-like proteins.

1.10 Sup35 NM as model protein of disease-associated proteins

Due to its ability to form self-replicating prions in yeast, Sup35 NM (hereafter NM) proved to be a suitable model protein to study amyloid replication and transmission in mammalian cell systems. As NM shares no sequence homology with any mammalian protein and has no physiological function in mammals, NM-HA aggregation can be studied without a loss-of-function phenotype. Our group established a mouse neuroblastoma (N2a) cell line that stably expresses NM fused to a C-terminal hemagglutinin (HA) tag (N2a NM-HA) (Krammer *et al.*, 2009). In N2a NM-HA cells, NM-HA is expressed cytosolically, resembling intracellular amyloidogenic proteins, such as tau or α-synuclein. NM-HA remains in a soluble state and, even when overexpressed, it rarely spontaneously aggregates (Duernberger *et al.*, 2018). In analogy to Sup35 in yeast, NM-HA aggregation is induced by exposing N2a NM-HA cells to recombinant fibrillar NM (figure 5) (Krammer *et al.*, 2009). NM-HA assembles into amyloid fibrils that persist in the cytosol over multiple passages and propagate in a self-perpetuating manner by seeded polymerization. Of note, neither soluble nor aggregated NM-HA is cytotoxic. To replicate faithfully, prions depend on constant fibril fragmentation, but there is no Hsp104 homologue in mammals. Therefore, NM-HA fibril disaggregation must be carried out by other, as yet unclear, mechanisms. Similar to mammalian prions, NM-HA seeds exhibit infectious properties and are transmitted vertically to progeny and horizontally to bystander cells (Krammer *et al.*, 2009). NM-HA seed transfer to neighboring cells is most effective by direct cell-cell contact (Hofmann *et al.*, 2013). NM-HA seeds are also released in small EVs that transport infectious entities to more distant cells (S. Liu *et al.*, 2016). Interestingly, EVs

containing small NM-HA oligomers were more potent in seeding than EVs shuttling higher-molecular amyloid, indicating that the NM-HA seed length influences seeding efficiency. Together, NM-HA behaves like a prion in mammalian cells and uses transmission pathways shared by human disease-associated amyloid.
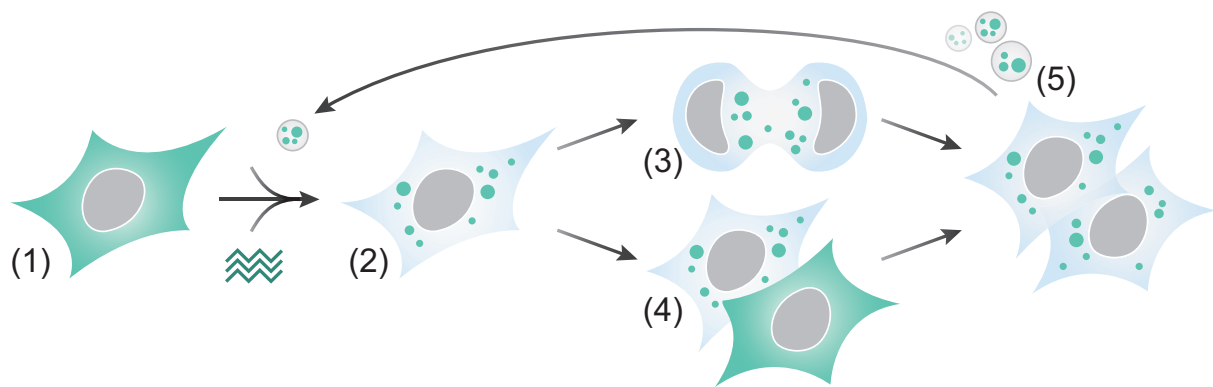
Figure 5. The prion life cycle of Sup35 NM in mammalian cells. (1) In N2a cell expressing HA-tagged NM (NM-HA), NM-HA resides in the cytosol in a soluble state. (2) Exposure to exogenous NM fibrils seeds NM-HA aggregation in a prion-like manner, leading to intracellular amyloid aggregates that are fragmented by unknown mechanisms. (3) Short NM-HA seeds are transferred vertically during mitosis or (4) horizontally to bystander cells by direct cell-cell contact. (5) In addition, cells secrete extracellular vesicles (EVs) containing infectious NM-HA entities, that seed NM-HA aggregation in distant cells.

Interestingly, the NM subdomain that nucleates amyloid formation and drives prion replication differs between N2a NM-HA cells and yeast. While *de novo* NM prion induction in yeast relies on the QNR, prion formation and propagation of NM-HA aggregates in murine cells is mediated by the last 2.5 repeats of the OPR and the CTN (Duernberger *et al.*, 2018). Understanding NM prion formation in a mammalian environment is of particular importance, as prion domains are not exclusive to yeast prions but are also found in the human proteome. Approx. 1 % of human proteins were predicted to have a QN-rich domain similar in composition to those of yeast prions (O. D. King *et al.*, 2012; An and Harrison, 2016). Many of these proteins are RNA-binding proteins that regulate the formation of reversible membrane-less compartments in the cell. Others, however, have direct implications for human NDDs, such as TDP-43 and FUS, whose aggregation is a hallmark of ALS, and a comorbidity of AD and PD. Hence, investigating NM aggregation and propagation in a mammalian environment could improve the understanding of common mechanism underlying human NDDs.

1.11 The NM-HA mouse model to study protein aggregation in vivo

To study more complex pathological aspects of NDDs, such as long-range cell-to-cell prion dissemination and induced neurotoxicity, our group has previously established the NM-HA mouse model to study NM aggregation *in vivo* (data unpublished). Since stable NM expression and seeded NM aggregation in post-mitotic mouse primary neurons and primary astrocytes have been shown to be non-toxic, the ectopic expression of NM in mice was expected not to harm the animals (Hofmann *et al.*, 2013). The NM-HA mouse model is based on a NM-HA knock-in (KI). In short, the open reading frame of the murine prion protein (PrP, gene *Prnp*) in exon 3 was replaced by the DNA sequence coding for NM (amino acids 1 – 253) (figure 6). In addition, a sequence coding for a hemagglutinin (HA) tag was inserted 3' of NM (NM-HA). Expression of the NM-HA transgene is driven by the prion protein promoter. Thus, NM-HA is expressed in the same cells that normally express PrP, such as neurons and astrocytes in the CNS, which theoretically should allow prion transmission. In homozygous animals, NM-HA is expressed

Figure 6. The NM-HA mouse model. NM-HA mice express NM with a C-terminal hemagglutinin tag (NM-HA) controlled by the murine prion protein promoter. The NM-HA coding sequence thereby replaces the sequence of the prion protein gene (*Prnp*) in exon 3.

from two alleles without overexpression. Alike NM-HA in mammalian cells, it should not possess a cellular function in mammals. Further, due to a lack of sequence homology with mammalian proteins, it is not expected to disturb cellular processes. Remarkably, because NM-HA is non-functional, it allows us to study the gain-of-function of cytosolic protein aggregates independently of the loss-of-function of the protein, which is not possible in any other mouse model.

2 Aim

NDDs are devastating diseases characterized by the progressive deposition and dissemination of aggregated proteins in the brain, which are linked to neuronal loss, cognitive decline, and ultimately death. While it is now widely accepted that disease-associated, amyloidogenic proteins have prion-like properties, the mechanisms underlying intracellular amyloid fragmentation and spreading remain enigmatic. Furthermore, it is still unclear how the gain-of-function of the amyloid and the functional loss of the aggregating protein contribute to neurotoxicity. Finally, NDDs show heterogeneous clinical symptoms and pathogenesis, which have been attributed to different amyloid conformers formed by the same protein. However, how the amyloid structure influences seed propagation in the brain remains to be elucidated.

In this project, we used the NM-HA mouse line, which expresses the yeast prion domain Sup35 NM, to model intracellular amyloidogenic proteins in a highly complex living animal. NM behaves like a prion in mammalian cells, hence, we aimed to test whether NM aggregation could also be induced in the brain of NM-HA mice and whether these aggregates would faithfully propagate in a prion-like manner. Since NM-HA mice express a non-functional yeast prion, we further investigated whether the gain-of-function of NM-HA aggregates, without interference from loss-of-function effects, would be sufficient to cause neurodegeneration in NM-HA mice. Lastly, to replicate human disease heterogeneity and study the influence of fibril conformation on disease progression, we tested two distinct NM fibril polymorphs in our mouse model. Therefore, NM-HA animals were intracranially injected with two structural variants of NM fibrils and were tested for cognitive deficits 12 months post injection. Brain tissue of inoculated animals was analyzed biochemically and histochemically at different time points to assess NM-HA aggregation, amyloid distribution, neurodegeneration, and inflammation. Ultimately, by using NM-HA as model amyloid we aimed to reveal common mechanisms underlying disease pathogenesis and neurotoxicity associated with intracellular amyloid.

3 Material

3.1 Equipment

Table 1. Instruments

Instruments	Company
Agarose Gel System	VWR
Anesthesia Mask	Kopf Instruments
Automated Cell Counter TC20	Bio-Rad
Axio Scan 7 Slide Scanner	Zeiss
Binocular Leica M651 MSD	Leica Microsystems
Biomek NXP Liquid Handler	Beckmann Coulter
CellVoyager 6000	Yokogawa Inc.
CO2 Incubator HERAcell 240i	Haraeus
Criterion™ Blotter	Bio-Rad
Earbars	Kopf Instruments
Eppendorf Centrifuge 5417R	Eppendorf
Fluostar Omega BMG	BMG Labtech
Fusion FX Imaging System	Vilber Lourmat
Germinator 500 Dry Sterilizer	CellPoint Scientific
Ideal Micro Drill	Braintree Scientific
Laser Scanning Microscope 800	Zeiss
Laser-Pipette-Puller P-2000	H. Saur Laborbedarf
Masterflex Easy Load Perfusion Pump	VWR
Maxisafe 2020 Class II Biological Safety Cabinet	Thermo Fisher Scientific
Mini-PROTEAN Gel System	Bio-Rad
Minitron Shaker	Infors HT
Mr. Frosty Freezing Container	Thermo Fisher Scientific
Multifuge X3R Hereus	Thermo Fisher Scientific
NanoDrop™ 2000	Thermo Fisher Scientific
Optima MAX-XP Ultracentrifuge	Beckmann Coulter
Orbital Shaker PSU-10i	Biosan
PowerPac™	Bio-Rad
Scale ABT 320-4M Analytical Balance	Kern & Sohn
Sliding and Freezing Microtome MICROM HM 450	Norbrain
Sonopuls HD 2070 Sonicator	Bandelin
Sonopuls HD 3200 Sonicator	Bandelin
Stereotaxic Frame	Kopf Instruments
T100 Thermo cycler	Bio-Rad
Thermomixer F1.5	Eppendorf

UMP3 UltraMicroPump	World Precision Instruments
Veterinary Anesthesia Evaporator	VetEquip
XCell4 SureLock™ Midi-Cell Electrophoresis System	Thermo Fisher Scientific

3.2 Consumables

Table 2. Consumables

Item	Company
0.22 µm filter (syringe and vacuum filter)	Merck
12 ml Bacteria Culture Tubes	Roth
4 - 12 % Bis-Tris NuPAGE Gels	Invitrogen
Adhesive PCR Plate Seals	Thermo Fisher Scientific
Black Multiwell Plates	Corning
Cell Counting Slides	Bio-Rad
Cell Culture Dishes	Corning
Cell Culture Multiwell Plates	Nunc, Thermo Fisher Scientific
Conical Centrifugation Tubes	Thermo Fisher Scientific
Corning™ Stripette™	Thermo Fisher Scientific
Coverslips	Paul Marienfeld
Criterion™ TGX™ Protein Gels (Tris-Glycine)	Bio-Rad
Cryotubes	Corning
Falcon Tubes (15, 50 ml)	BD Biosciences
Glassware	Schott
His Trap Protein Purification Column (5 ml)	GE HealthCare
HiTrap Desalting Column (5 ml)	GE HealthCare
Low profile disposable blades	Leica
Micro Cuvettes	Brand
Microliter Syringe (5 µl)	Hamilton
Microplate, 96-well, F-bottom, black	Greiner Bio-One
Parafilm	VWR, Darmstadt
PCR Tubes	Sigma Aldrich
Pipets	Eppendorf
Protein Low-bind Tubes (0.5 - 5 ml)	Eppendorf
PVDF Membrane (0.4 µm)	GE Healthcare
Reaction Tubes	Eppendorf
Sterican Needles	Braun
Sterile Cotton Swap	Deltalab
Sterile Syringes (1 ml, 5 ml)	Braun
Sugi Eyespear Pointed Tip	Kettenbach GmbH & Co.KG
SuperFrost® Plus Slides	Thermo Fisher Scientific
Surgcial Instruments	Fine Science Tools
Surgical Gloves	Sempermed

Thin Wall Glass Capillaries	World Precision Instruments
Ultracentrifugation Tubes (1.5 ml)	Beckmann Coulter
Vivaspin 20 Concentrator	Merck
Whatman Paper	Roth

3.3 Chemicals, Reagents, Enzymes

All standard chemicals were of at least analytical grade and purchased from Carl Roth or Sigma Aldrich unless stated otherwise.

Table 3. Chemicals, Reagents, Enzymes

Item	Company
0.25 % Trypsin-EDTA	Life Technologies
100 bp DNA Ladder	New England Biolabs
10x *Taq* Reaction Buffer	New England Biolabs
3M Vetbond Tissue Adhesive	VWR
Agarose	Biozym
Aqua Poly Mount Mounting Solution	Polysciences
Benzonase	Merck
BL21(DE3) Competent Cells	Thermo Fisher Scientific
Bovine Serum Albumin (BSA)	Sigma Aldrich
Buprenovet	WDT
ChemiBLOCKER™ Solution	Merck
cOmplete™, EDTA-free Protease Inhibitor Cocktail	Roche
Dimethyl Sulfoxide (DMSO)	Honeywell
DMEM® I (1X) + GlutaMAX™ -I	Life Technologies
dNTP mix 10 mM	Thermo Fisher Scientific
DRAQ5™ Fluorescent Probe Solution	Thermo Fisher Scientific
Dulbecco's Phosphate Buffered Saline (DPBS)	Life Technologies
Eye Moisturizing Cream	Bepanthen
Foetal Bovine Serum (FBS)	PAN Biotech GmbH
Formaldehyde Solution	Sigma Aldrich
Gel Loading Dye, 6x	New England Biolabs
Halt™ Protease and Phosphatase Inhibitor Cocktail (100X)	Thermo Fisher Scientific
Hoechst Solution	Thermo Fisher Scientific
Isoflurane	Piramal Healthcare
Lipofectamine 2000	Thermo Fisher Scientific
Lysogenic broth (LB) medium	Roth
$MgCl_2$ Solution	New England Biolabs
Mirus Bio TransIT-2000	Thermo Fisher Scientific
NMS-873	Selleckchem

Nonident® P-40 (NP-40)	Thermo Fisher Scientific
Octenisept Disinfectant	Schuelke
Page Ruler Prestained Protein Ladder	Thermo Fisher Scientific
Paraformaldehyde, 16 % [w/v]	Thermo Fisher Scientific
Penicillin- Streptomycin	Life Technologies
Prolong Gold Antifade Mountant	Invitrogen
Proteinase K	Roche
Re-Blot Plus Strong Solution	Merck
Release	WDT
Rimadyl	Zoetis
SOC medium (super optimal broth with catabolic repressor)	Thermo Fisher Scientific
SuperSignal West Femto	Thermo Fisher Scientific
SuperSignal West Pico	Thermo Fisher Scientific
Taq DNA Polymerase	New England Biolabs
Tissue-Tek® O.C.T. Compound	Sakura Finetek
TrueBlack® Lipofuscin Autofluorescence Quencher	Biotium
Xylocain Gel 2 %	Aspen Pharmacare

3.4 Kits

Table 4. Kits

Kit	Company
DC protein assay kit	BioRad
Hematoxylin-Eosin-Staining Kit	Roth
ImmPACT DAB, Peroxidase Substrate Kit	Vector Laboratories
Mouse on Mouse Immunodetection Kit	Vector Laboratories
Quick Start™ Bradford protein assay	BioRad
Vectastain® Elite® ABC-HRP Kit (Rabbit IgG)	Vector Laboratories

3.5 Antibodies

Table 5. Primary Antibodies

Primary Antibody	Host and clone	Application	Source	Dilution
Anti-Actin	Mouse monoclonal	WB	MP Biomedicals, 691001	1:5000
Anti-HA	Rat monoclonal	WB	Roche, clone 3F10	1:1000
Anti-HA	Rat monoclonal	IHC IF	Cell Signalling, C29F4	1:20000 1:1000
Anti-HA Alexa 647 Fluor conjugated	Mouse monoclonal	IF	MBL International M180-A64	1:500

Anti-NM 4A5 (hybridoma supernatant)	Rat monoclonal	WB IF	Provided by Dr. Feederle, Helmholtz Zentrum, Munich, Germany	1:10 1:5
GFAP	Chicken polyclonal	IF	abcam, ab4674	1:1000
Hsp70	Mouse monoclonal	IF	Enzo Life Sciences, C92F3A-5	1:500
Iba1	Rabbit polyclonal	IF	WAKO	1:2000
MAP2	Mouse monoclonal	IF	abcam, ab11268	1:1000
NeuN	Mouse monoclonal	IF	Merck, MAB377	1:1000
p62	Rabbit monoclonal	IF	abcam, ab109012	1:500
Ubiquitin	Mouse monoclonal	IF	Merck, MAB1510	1:500
VCP	Mouse monoclonal	IF	Thermo Fisher Scientific, MA3-004	1:100

Table 6. Secondary Antibodies

Secondary Antibody	Host	Application	Reference	Dilution
Anti-Mouse IgG, HRP - conjugated	Goat	WB	Dianova	1:10000
Anti-Rat IgG, HRP - conjugated	Goat	WB	Dianova	1:10000
Anti-Chicken IgY, DyLight® 488 - conjugated	Goat	IF	abcam, ab96947	1:500
Anti-mouse IgG, Alexa Fluor 647 - conjugated	Goat	IF	Life Technologies	1:500
Anti-rabbt IgG, Alexa Fluor 546 - conjugated	Goat	IF	Life Technologies	1:500
Anti-Rat IgG, Alexa Fluor 488 - conjugated	Goat	IF	Life Technologies	1:500
Anti-Rat IgG, Alexa Fluor 647 - conjugated	Goat	IF	Life Technologies	1:500

3.6 Genotyping Primers

Table 7. Genotyping Primers

Target	Sequence 5' to 3'
NMHA_reverse	GTTGGGCTTGAGCATTGTAAGCTTG
PrnP_forward	GAGGGTTGACGCCATGACTT
PrnP_reverse	CCCTCCAGGCTTTGGCCGCTT

3.7 Plasmids

Table 8. Plasmids

Construct	Backbone	Reference
NM-His	pETRO1.01	
pET20b(+)-SUP35NMΔ39-His6	pET20b	(Allen *et al.*, 2005)
pET20b(+)-SUP35NMΔ75-123-His6	pET20b	(Allen *et al.*, 2005)
VSV-G	pMD2.VSVG	
Empty	phCMV-3´UTR	

3.8 Cell lines

Table 9. Cell lines

Cell line	Reference
HEK NM-GFP^{sol}	(S. Liu *et al.*, 2017)
HEK NM-HA^{agg} clone 75	(S. Liu *et al.*, 2017)
N2a NM-GFP^{sol}	(Hofmann *et al.*, 2013)
N2a NM-HA^{agg}	(Krammer *et al.*, 2009)
N2a NM-HA^{sol}	(Krammer *et al.*, 2009)

3.9 Software

Table 10. Software

Software	Company
Adobe Illustrator 2022	Adobe
Adobe Photoshop 2022	Adobe
ARIVIS	Zeiss
CV7000 Analysis Software R2.08.09	Yokogawa Inc.
EthoVision XT	Noldus
Fiji (ImageJ)	http://rsbweb.nih.gov/ij/
FLUOstar Software	BMG Labtech
GraphPad Prism 9	GraphPad
Microsoft Office 2011	Microsoft
ZenBlue	Zeiss

4 Methods

4.1 Molecular Biological Methods

4.1.1 Transformation

For NM-His purification, BL21 competent *E. coli* were transformed with 100 ng plasmid coding for NM-His or the deletion mutants NM-His$^{\Delta 1\text{-}39}$ and NM-His$^{\Delta 75\text{-}123}$ (table 8). After incubating the bacteria-plasmid-mixture on ice for 20 min, bacteria were transformed at 42 °C for 45 s and subsequently cooled on ice for 10 min. 1 ml SOC media without antibiotics was added and the suspension was incubated at 37 °C and 300 rpm (Thermomixer F1.5, Eppendorf) for 45 min. Bacteria were pelleted by a short spin at 3000 x g and resuspended in 150 µl SOC medium. 10 – 25 µl suspension was spread on prewarmed LB plates supplemented with 100 µg/ml ampicillin. Plates were incubated at 37 °C ON and then stored at 4 °C.

4.1.2 Expression of NM-His in E. coli

To ensure sufficient NM-His expression, 6 to 8 colonies of transformed BL21 competent *E. coli* (section 4.1.1) were picked and inoculated in 10 ml LB media containing 100 µg/ml ampicillin. The cultures were incubated at 37 °C ON at 180 rpm (Minitron, Infors HT) and were pooled the next day. 2 l baffled flasks with 250 ml LB media supplemented with ampicillin were inoculated with 5 ml of the pooled starter cultures. The flasks were incubated at 37 °C and 180 rpm for 2 – 2.5 h until an OD$_{600}$ of 0.8 was reached. NM-His expression was induced by adding 1 mM IPTG to the cultures. After 3 h incubation, the bacteria were pelleted for 10 min at 3000 x g and stored at -80 °C until further use.

4.1.3 DNA extraction from mouse tissue biopsy

Tissue lysis buffer

100 mM	Tris (pH 8.0)	
5 mM	EDTA (pH 8.0)	
200 mM	NaCl	
0.2 %	SDS,	pH 8.0

For DNA extraction from ear punch biopsies, each tissue sample was digested in 500 µl tissue lysis buffer supplemented with 200 µg/ml proteinase K at 55 °C and 550 rpm (Thermomixer, Eppendorf) ON. Remaining tissue was pelleted by centrifugation for at RT 20 min at 18000 x g

before the DNA was precipitated from the supernatant by adding 500 µl isopropanol. After pelleting the DNA at 4 °C for 20 min at 18000 x g, the pellet was washed with 300 µl 70 % [v/v] ethanol. After another spin at 4 °C for 20 min at 18000 x g, the supernatant was removed and the pellet was dried at 37 °C. The DNA was dissolved in 30 µl nuclease-free water and stored at -20 °C until further use.

4.1.4 Polymerase chain reaction (PCR) and agarose gel electrophoresis

TAE buffer

40 mM	Tris	
20 mM	Acetic acid	
1 mM	EDTA,	pH 8.0

Extracted DNA (section 4.1.3) was analyzed for the NM-HA transgene via PCR. To this end, 2 µl extracted DNA was mixed with PCR reaction buffer, 1.5 mM $MgCl_2$, 200 nM dNTPs, 200 nM of each primer and 0.38 units of Taq polymerase in a final volume of 15 µl. Tubes were vortexed and quickly spun before transferring them to a PCR cycler. The DNA was amplified by activating the polymerase at 94 °C for 3 min, followed by 34 cycles of denaturation at 94 °C for 45 s, primer annealing at 62 °C for 30 s, and primer extension at 72 °C for 1 min. The DNA was finally extended at 72 °C for 10 min before cooling at 4 °C. PCR products were mixed with DNA loading dye and were separated on a 2 % [w/v] agarose gel supplied with Gel Red DNA Nucleic Acid Gel Stain (diluted 1:10000). The gel was run at 100 V for 1.5 h and was imaged using the Fusion FX imaging system.

4.2 Protein biochemical methods

4.2.1 Purification of NM-His via Immobilized Metal Affinity Chromatography (IMAC)

Buffer A				Buffer B		
10 mM	$Na_2H_2PO_4$ x 2 H_2O			10 mM	$Na_2H_2PO_4$ x 2 H_2O	
10 mM	NaH_2PO_4			10 mM	NaH_2PO_4	
0.5 M	NaCl			0.5 M	NaCl	
20 mM	Imidazole			500 mM	Imidazole	
8 M	Urea,	pH 7.2		8 M	Urea,	pH 7.2

To purify full length NM-His and NM-His deletion mutants Δ1-39 and Δ75-123, pellets of transformed bacteria (section 4.1.1) were lysed under denaturing conditions in 25 ml buffer A. After 1 h shaking at RT at 150 rpm (Orbital Shaker, Biosan), the lysate was sonicated for 3

x 10 s at 50 % intensity. Cell debris was pelleted by spinning for 20 min at 10000 x g at RT. The supernatant was harvested, pooled, and filtered through a 0.22 μm filter. NM-His was purified from the lysate by IMAC using the ÄKTA pure protein purification system together with a 5 ml HisTrap™ HP His tag protein purification column. After washing the column with 25 ml buffer A, the filtered cell lysate was loaded onto the column. Unbound protein was removed by washing with 75 ml buffer A. Bound NM-His was eluted with a linear imidazole gradient from 10 mM to 250 mM imidazole (2 % [v/v] to 50 % [v/v] buffer B). All protein-containing fractions were pooled and concentrated to 10 % of the initial volume by ultrafiltration using Vivaspin® 20 concentrator columns with a molecular cut-off of 10000 Da according to the manufacturer's instructions. The concentrated protein was eluted in sterile-filtered PBS by washing 500 μl fractions of the concentrate using a 5 ml HiTrap® desalting column. All protein-containing fractions were pooled in protein low-bind tubes and the protein concentration was determined via Bradford assay according to the manufacturer's instructions. Purified proteins were stored at -80°C until further use.

4.2.2 Generation of two recombinant NM-His fibril variants

The yeast prion domain Sup35 NM has been shown to form distinct fibril conformers *in vitro* when incubating the monomeric protein at 4 °C and 37 °C (Chien *et al.*, 2003; Tanaka *et al.*, 2004). In this project, we adapted the described protocol to generate two structural variants of full-length NM-His fibrils, F4 and F37. To ensure spontaneous aggregation without templating seeds, pre-existing seeds were removed from the NM-His monomer solution prior to *de novo* fibril generation. To do so, recombinant NM-His was diluted in PBS to 0.5 mg/ml (14.8 μM) and was boiled at 95 °C for 15 min. After cooling down at RT for 5 min, heat-resistant aggregates were pelleted at 15000 x g for 10 min at RT. The supernatant was transferred to protein low-binding tubes and was incubated for 72 h in the cold room at 4 °C or in a thermomixer (Eppendorf) at 37 °C without agitation. In parallel, the absence of seeds was confirmed via ThT assay (section 4.2.3). Generated fibrils were snap frozen and stored at -80°C.

4.2.3 Thioflavin-T assay

CRBB buffer
5 mM KH_2PO_4
150 mM   NaCl, pH 7.4

Thioflavin-T (ThT) is a fluorescent dye that emits light at 485 nm upon binding to amyloid fibers. Thus, measuring the fluorescence intensity of a protein-ThT-mixture allows monitoring

of aggregate formation *in vitro* in real-time (LeVine, 1993; Xue *et al.,* 2017). Monomeric recombinant NM-His (full-length or NM-His$^{\Delta1-39 \text{ or } \Delta75-123}$) was diluted to 0.5 mg/ml in CRBB buffer and pre-existing seeds were removed as described (section 4.2.2). To monitor spontaneous protein aggregation, 5 μM of seed-free NM-His (hereafter termed substrate) was mixed with 20 μM of ThT. 150 μl of the mixture was added per well in a black 96 well plate with glass bottom (Greiner Bio-One). To accelerate seeding and to increase reproducibility, each well received three sterile glass beads (Giehm and Otzen, 2010). The plate was sealed and immediately placed in the plate reader for analysis of ThT fluorescence. To characterize F4 and F37 fibrils, monomeric NM-His substrate was seeded with 5 % [mol/mol] (0.25 μM monomer equivalent) F4 and F37 fibrils (the seeds). Seeding was improved by sonicating the fibrils before use for 3 min at 10% power with intervals of 5 s sonication and 1 s break on ice. Fibrils were added to the NM-His-ThT mixture and the plate was sealed and immediately placed in the Fluostar Omega plate reader (BMG Labtech). Aggregate formation was followed by exciting ThT at 445-450 nm and detecting the emitted light at 475-485 nm from the bottom of the plate. The plate was incubated at 25 °C and was continuously shaken orbitally for 24 h at 300 rpm. ThT fluorescence emission was measured every 5 min.

4.2.4 SDS-Thermo-resistance assay

SDS – CRBB buffer			*3x Loading dye*		
5 mM	KH$_2$PO$_4$		30 % [v/v]	Glycerol	
150 mM	NaCl		0.3 % [w/v]	Bromphenol blue	
1 % [w/v]	SDS,	pH 7.4	90 mM	Tris HCl,	pH 6.8

Depending on their conformation, NM fibrils have been shown to differ in their resistance to heat and denaturing agents such as SDS (Tanaka 2004). To characterize generated NM-His fibril variants F4 and F37 (section 4.2.2), 2 μg of NM-His fibrils were incubated in CRBB buffer supplemented with 1 % [w/v] SDS for 15 min at 25, 35, 45, 55, 65, 75, 85, or 99 °C, respectively. Samples were mixed with loading dye and loaded on 4 – 12 % Bis-Tris NuPAGE gels (Invitrogen) without another denaturing boiling step before performing Western blot analysis (section 4.2.10).

4.2.5 Transmission electron microscopy analysis

To determine the seed length of NM fibrils F4 and F37 before and after sonification, transmission electron microscopy (TEM) was performed by Emiel Michiels (VIB Center for Brain and Disease Research, Leuven). In short, 5 μl fibril solution were spotted on glow-discharged TEM grids and incubated for 10 min. After washing with ddH$_2$O, grids were stained

with 2 % [w/v] filtered uranyl acetate and finally washed again with ddH$_2$O. Fibrils were imaged and the length of 80 – 130 seeds was manually measured per experiment. The experiment was repeated three times.

4.2.6 Preparation of cell lysates

NP-40 lysis buffer

50 mM	Tris-HCl pH 7.5
150 mM	NaCl
0.5 % [v/v]	NP-40

For cell lysis, cells were detached with trypsin (section 4.3.1), resuspended in PBS and pelleted at 4 °C at 300 x g for 10 min. After two washes in PBS, the cell pellet was either stored at -20 °C or was directly lysed. For lysis, the pellet was resuspended in 30 - 70 µl lysis buffer supplemented with 1 x protease and phosphatase inhibitor. After incubation on ice for 30 min, cell debris was pelleted by spinning at 4 °C and 2300 x g for 3 min. The supernatant was collected and stored at -20 °C. Alternatively, the protein concentration was directly determined via Bradford assay (section 4.2.8).

4.2.7 Preparation of brain homogenates

For molecular analysis, aliquoted pulverized brain samples (section 4.5.5) were lysed in 100 – 250 µl NP-40 lysis buffer supplemented with 1 x protease and phosphatase inhibitor (Thermo Fisher Scientific) and 125 U benzonase on ice for 45 min. For cell culture experiments, samples were lysed in 100 – 250 µl PBS with 1x protease inhibitor. To increase homogenization, samples were forced ten times through a 30 G needle. In addition, samples lysed in PBS underwent sonification for 3 min at 50 % power to improve lysis. Finally, samples were spun at 4 °C and 10600 x g for 15 min. The supernatant was taken off and was directly analyzed via Bradford assay (section 4.2.8).

4.2.8 Bradford assay

To determine the total protein concentration in cell and brain lysates (sections 4.2.6, 4.2.7), samples were diluted 1:10 in ddH$_2$O. 5 µl of the dilution were transferred in duplicates to a 96-well plate along with 5 µl BSA standard solutions ranging from 125 µg/ml to 2000 µg/ml. 250 µl Bradford reagent was added to each well and the plate was incubated for 5 min at RT before measuring the absorbance at 595 nm using the Fluostar Omega plate reader (Labtech). The total protein concentration was determined using the MARS analysis software.

4.2.9 Sodium dodecyl sulfate–polyacrylamide gel electrophoresis (SDS-PAGE)

3x SDS Loading buffer

90 mM	Tris-HCl pH 6.8
7 % [w/v]	SDS
30 % [v/v]	Glycerol
20 % [v/v]	2-Mercaptoethanol
0.003 % [w/v]	Bromphenol blue

Tris Glycine SDS Running buffer

25 mM	Tris	
192 mM	Glycine	
0.1% [w/v]	SDS,	pH 8.3

For protein analysis, proteins were denatured and separated according to their molecular weight via SDS-PAGE. If not stated otherwise, 30 - 50 µg total protein from cell lysates and 100 µg total protein from brain lysates was mixed with the appropriate amount of lysis buffer and 3x SDS loading buffer. Samples were boiled for 10 min at 95 °C and loaded on precast 12 % [v/v] polyacrylamide gels (Bio-Rad), together with 8 µl protein ladder. The gels were run for 1.5 h at 30 mA per gel and proteins were subsequently transferred to PVDF membranes via Western blot (section 4.2.10).

4.2.10 Western blot analysis

Transfer buffer

250 mM	Tris
1.92 M	Glycine
0.1 % [w/v]	SDS
10 % [v/v]	Methanol

TBST

250 mM	Tris HCl pH 7.6
1.5 M	NaCl
0.5 % [v/v]	Tween-20

Milk blocking buffer

5 % [w/v] milk powder
in TBST

BSA blocking buffer

3 % [w/v] milk powder
in TBST

Proteins separated via SDS-PAGE (section 4.2.9) were transferred to PVDF membranes via standard Western blot technique. PVDF membranes were activated in methanol for 20 s and proteins were blotted for 45 min at 100 V in a wet electroblotting chamber (Bio-Rad). Membranes were blocked in milk or BSA blocking buffer for 1 h at RT. Subsequently, the primary antibody (table 5) was diluted in the respective blocking buffer and applied overnight at 4 °C. Membranes were washed 3 x 10 min in TBST before incubating them with horseradish peroxidase (HRP) -coupled secondary antibody diluted in milk blocking buffer for 1 h at RT. After 3 x 10 min washing steps in TBST, proteins were visualized with ECL pico or ECL femto (Thermo Fisher Scientific) detection solution using the Fusion FX imaging system. For reprobing, membranes were stripped in 10 - 20 ml Re-Blot solution (Merck) for 20 min at RT.

Membranes were shortly rinsed with ddH$_2$O, activated with methanol, and blocked for 1 h in the respective blocking buffer. The detection protocol was followed as described above.

4.2.11 Sedimentation assay

To verify NM-HA aggregates in brain samples of injected animals, 150 μg total protein from brain lysates (section 4.2.7) were mixed with lysis buffer and 10 μl blue dextran to a final volume of 40 μl. 100 μg total protein from NM-HA^{agg} or NM-HA^{sol} cell lysates served as control. Samples were spun in an ultracentrifuge (Optima MAX-XP, Beckmann Coulter) at 4 °C and 100000 x g for 60 min. 20 μl of the supernatant was mixed with 7 μl SDS loading buffer and boiled at 95 °C for 5 min. The pellet was washed with 100 μl NP-40 lysis buffer and spun at 4 °C and 100000 x g for 30 min. Finally, the supernatant was discarded and the pellet was resuspended in 20 μl NP-40 lysis buffer and 7 μl SDS loading buffer. Proteins were denatured at 95 °C for 5 min before samples were stored at -20 °C until performing Western blot (section 4.2.10).

4.3 Cell Biological Methods

4.3.1 Cell culture

All cell culture work was performed under sterile conditions using DMEM + GlutaMAX media supplemented with 10 % [v/v] fetal calf serum and 1 % [v/v] Penicillin-Streptomycin. Cells (table 9) were grown on 10 cm dishes at 37 °C with 5 % CO$_2$ and were passaged every 2-3 days. To do so, cells were washed with PBS and detached with 1 ml 0.25 % Trypsin-EDTA solution. Cells were resuspended in 9 ml complete media and counted using an automated cell counter (Automated cell counter TC20, Bio-Rad). 5 x 10^5 or 2.5 x 10^5 cells were seeded on 10 cm dishes for 2 or 3 days. For long-term storage, detached cells were pelleted at 300 x g for 5 min and 5 x 10^5 cells were aliquoted in FCS containing 10 % [v/v] DMSO in cryogenic vials. Cells were cooled in freezing containers at -80 °C before vials were transferred to liquid nitrogen. To recover frozen cells, vials were thawed and cells were mixed with 10 ml prewarmed media. Cells were spun at 300 x g for 5 min to remove DMSO-containing media. The pellet was resuspended in 12 ml complete media and transferred to a 10 cm dish.

4.3.2 Seeding of NM-HA aggregates by sonicated NM-His fibrils

The seeding efficiency of F4 and F37 NM-His fibrils (section 4.2.2) was tested in N2a cells expressing soluble NM-HA (N2a NM-HA^{sol}). 4000 cells per well were seeded on a 384 well

plate and cells were incubated at 37 °C for 1 h. F4 and F37 fibrils were sonicated for 3 min at 10 % power with 5 s pulses and 1 s breaks on ice (Sonopuls HD 3200 sonicator, Bandelin). 1 h post seeding, 5 – 1000 nM of sonicated fibrils (monomer equivalent) were added to the cells in quadruplicates. As negative controls, seed-free soluble NM-His (section 4.2.2) or equivalent amounts of PBS was added. N2a cells propagating NM-HA aggregates (N2a NM-HA^{agg}) served as positive control. Cells were incubated at 37 °C for 16 – 18 h ON before cells were fixed with 2 % [v/v] PFA in PBS at 37 °C for 20 min. NM-HA aggregates were immunofluorescently stained (section 4.3.7) and imaged using the CellVoyager CV6000 automated confocal microscope (section 4.3.8).

4.3.3 Seeding of NM-HA aggregates by mouse brain homogenate

To characterize NM aggregates in the brain from injected animals, NM-HA aggregation in N2a NM-HA^{sol} cells was seeded with mouse brain homogenate. To this end, 2500 - 3000 cells were plated per well on a 384 well plate and cells were incubated at 37 °C ON. The next day, brain homogenate from injected animals was diluted in DMEM media to reach a final concentration of 55.56 ng/μl total protein per well. The samples were sonicated for 3 min at 10 % power with 5 s pulses and 1 s breaks on ice. To seed aggregation in one well, 0.07 μl of Lipofectamine 2000 was carefully mixed with 5 μl OptiMEM without supplements. The Lipofectamine-mix was added to 10 μl of diluted brain homogenate and was gently mixed by pipetting. After incubation at RT for 5 min, 15 μl of the mixture was added per well in quadruplicates and cells were incubated at 37 °C for 24 h. Finally, cells were fixed with 2 % [v/v] PFA in PBS at 37 °C for 20 min before staining for HA (section 4.3.7) and imaging of NM-HA aggregates via automated confocal microscopy (section 4.3.8).

4.3.4 Seeding of NM-HA aggregates by recombinant NM-His

The formation of seeds when soluble NM-His was forced through a glass tip during injection was investigated by seeding N2a NM-HA^{sol} cells. 4000 cells per well were seeded on a 384 well plate and were incubated at 37 °C ON. The next day, pre-existing seeds were removed from NM-His as described (section 4.2.2) and the tube was incubated on ice for 1.5 h. This corresponded to the time the sample was incubated when injecting two animals. Subsequently, the injection glass tip was filled with NM-His at a speed of 2000 nl/min before releasing the protein with 100 nl/min. Cells were seeded with 62.5 – 250 nM NM-His and Lipofectamine 2000 as described (section 4.3.3) and cells were incubated at 37 °C ON. As controls, cells were seeded with appropriate amounts of F37 fibril and deseeded NM-His that had not been pushed through the glass tip. Finally, cells were fixed with 2 % [v/v] PFA in PBS

at 37 °C for 20 min before staining for HA (section 4.3.7) and imaging NM-HA aggregates (section 4.3.8).

4.3.5 Stable propagation of NM aggregates over several passages

The prion-like nature of NM aggregates induced by mouse brain homogenates was tested by assessing the stable propagation of NM aggregates in N2a cells over several passages. To facilitate aggregate detection, N2a cells expressing NM-GFP (N2a NM-GFP^{sol}) were used. 5000 cells per well were seeded on a 96-well plate and cells were incubated at 37 °C ON. The next day, cells were exposed to brain homogenate from fibril-injected animals as described (section 4.3.3). To increase the seeding rate, 0.2 µg/µl total protein and 0.5 µl Lipofectamine 2000 were added per well. 24 h post seeding, cells were transferred to a 24 well plate for expansion. Cells were grown to confluency before isolating single cell clones. Cell clones were grown for 2 weeks and all clones that propagated NM-GFP aggregates were transferred to 96 well plates. The clones were passaged every 2 to 3 days and NM-GFP aggregates were quantified every second passage via automated confocal microscopy (section 4.3.8).

4.3.6 Assessment of NM seed transmission via co-culture

The effect of valosin-containing protein (VCP) inhibition on the degradation of NM-HA aggregates was investigated in a co-culture experiment using donor HEK cells propagating NM-HA^{agg} and recipient HEK NM-GFP^{sol} cells. N2a cells were unsuitable due to their expression of retroviral proteins, which facilitate seed uptake in the recipient cells (Pothlichet *et al.*, 2006). To improve aggregate dissemination, donor cells were transfected to express the vesicular stomatitis virus glycoprotein (VSV-G) (Vorberg et al. 2021). To do this, donor cells were plated with a density of 5×10^5 cells per well on a 6-well plate and were grown at 37 °C ON. The next day, the media was replaced by 1.75 ml complete DMEM media. 1 µg plasmid coding for VSV-G or an empty vector (pHCMV) was mixed with 7 µl prewarmed transfection reagent TransIT-2020 (Mirus Bio) in 250 µl Opti-MEM media without supplements. After gentle mixing, the solution was incubated at RT for 30 min and carefully applied on the cells. Non-transfected donor cells were used as control. 6 h post-transfection, 2 µM VCP inhibitor NMS-873 or the equivalent amount of DMSO was added to the media and cells were incubated at 37 °C for 24 h. For the co-culture, transfected donor and recipient cells were detached and counted as described (section 4.3.1). Per well of a 384-well plate, donor and recipient cells were mixed at a ratio of 5:1 using 3×10^4 cells in total in 40 µl complete DMEM media. 6 replicates per co-culture were plated on a 384-well plate and were

incubated at 37 °C for 24 h. Cells were fixed with 2 % [v/v] PFA in PBS at 37 °C for 20 min and induced NM-GFP aggregates were quantified automatically (section 4.3.8).

4.3.7 Automated immunofluorescence staining

Blocking buffer
5 % [v/v] Chemiblock solution
0.5 % [v/v] Triton X-100
in PBS

NM-HA aggregates in induced N2a NM-HA cells were visualized by immunofluorescence staining for HA. Using an automated pipetting workstation (Biomek NXP, Beckmann Coulter), fixed cells were washed twice with PBS for 3 min at RT before permealizing for 10 min with 0.5 % [v/v] Triton X-100 in PBS. Subsequently, cells were blocked in blocking buffer for 30 min at RT before adding the Alexa 647-conjugated anti-HA antibody (table 5) for 1 h at RT in the dark. After 3 washes with PBS for 3 min, nuclei were stained with 2 μM Hoechst in PBS for 10 min at RT. The plate was either stored at 4 °C or directly imaged and analyzed (section 4.3.8).

4.3.8 Automated confocal imaging and aggregate quantification

To quantify NM aggregates, fixed and stained cells were imaged automatically using an automated confocal microscope (CellVoyager 6000, Yokogawa Inc.). Per well, 16 images (> 500 cells) at random positions were taken using a 40x water immersion objective. Images were analyzed automatically using the CellVoyager analysis software. To this end, image segmentation pipelines based on the signals of Hoechst (excitation at 350 nm, HA (excitation at 647 nm), or GFP (excitation at 488 nm) were applied to detect cell nuclei and NM aggregates. The percentage of cells with aggregates was determined by calculating the ratio of cells carrying aggregates to all counted cells.

4.4 Histological methods

4.4.1 Immunofluorescence staining of free-floating sections

TBS	*TBST*	*Permeabilization buffer*
0.05 M Tris	0.25 % [v/v] Triton X-100	0.6 % [v/v] H_2O_2
0.15 M NaCl pH 7.4	in TBS	in TBS

For immunofluorescence staining, brain sections were washed three times in PBS at RT for 5 min at 200 rpm (Orbital Shaker PSU-10i, Biosan) to remove all anti-freezing solution. Subsequently, the tissue was permeabilized for 30 min in 500 µl permeabilization buffer at 200 rpm. After 3 washes in TBST for 10 min, the sections were blocked in 2.5 % [w/v] goat serum in TBST at RT for 1 h while shaking. When a mouse antibody was used, the sections were additionally blocked in M.O.M blocking solution (Vectorlabs) diluted 1:200 in TBS for 1 h. The primary antibody was diluted in 2 % [w/v] goat serum in TBST (table 5) and was incubated at RT at 150 rpm ON. The next day, sections were washed three times in TBST for 10 min at 150 rpm. The respective secondary antibody (table 6) was diluted in 2 % [w/v] goat serum in TBST and was incubated at RT for 4 – 5 h at 150 rpm in the dark to reach full tissue penetration. Following 3 washes in TBST for 10 min, nuclei were stained for 15 min with Hoechst diluted 1:10000 in TBS. Finally, sections were mounted on slides and were dried for 20 – 30 min in the dark before mounting the coverslip.

For ThS staining, the sections were washed as described after the secondary antibody incubation. Subsequently, sections were mounted on slides and were dried for 10 – 20 min in the dark. To increase the ThS signal, Lipofuscin was quenched by applying TrueBlack Lipofuscin Autofluorescence Quencher (Biotinum) according to the manufacturer's instructions. After 3 rinses in TBS, nuclei were stained with 10 nM Draq5 in TBS for 30 min in the dark. The stain was rinsed off with TBS and amyloid structures were stained for 8 min with filtered 0.05 % [w/v] ThS solution freshly diluted in 50 % [v/v] ethanol. Sections were washed two times in 50 % [v/v] ethanol for 5 min before rinsing three times with TBS for 2 min. Finally, the coverslip was mounted while sections were still wet. Sides were dried in the dark ON and were either stored at 4 °C or imaged using the laser-scanning confocal microscope LSM 800 (Zeiss).

4.4.2 Immunohistochemistry

Quenching solution

3 % [v/v] H_2O_2
10 % [v/v] Methanol
in TBS

For immunohistochemistry, brain sections were washed twice with PBS at RT for 5 min at 200 rpm to remove all anti-freezing solution. Endogenous peroxidases were quenched with quenching solution for 30 min at 200 rpm. After washing three times in TBST, sections were blocked in 5 % [w/v] goat serum in TBST for 1 h at 200 rpm. The respective primary antibody (table 5) was diluted in 1 % [w/v] goat serum in TBST and was applied at 150 rpm ON. The

next day, section were washed three times with TBST for 10 min before applying the biotin-conjugated secondary antibody (Vectastain Elite ABC-HRP Kit, Vectorlabs) diluted 1:200 in 1 % [w/v] goat serum in TBST for 1 h at 150 rpm. Following 3 washes in TBST for 10 min, the AB reagents (Vectastain Elite ABC-HRP Kit, Vectorlabs) were applied for 1 h according to the manufacturer's instructions. Sections were washed twice in TBST and once in TBS for 10 min before developing the HA signal for 2 – 4 min using the diaminobenzidine (DAB) Peroxidase Kit (Vectorlabs) according to the manufacturer's instructions. Finally, sections were washed three times with TBS and mounted on slides. After drying, the coverslip was mounted and slides were dried ON. For NM-HA aggregate quantification, sections were imaged using the automated slide scanner Axioscan 7 (Zeiss).

4.5 Animals

4.5.1 Animal husbandry

All animal experiments performed in this study were approved by the animal protection committee of the North Rhine-Westphalia State Environment Agency (LANUV), animal protocol 81-02.04.2019.A071. Mice were housed in groups of one to five animals in individually ventilated cages with 12 h light/dark cycle at 22 °C and 60 % humidity. Animals had free access to food and autoclaved or acidulated water. In this project, homozygous NM-HA mice and wild type (WT) mice of both genders were used for stereotactic injections. NM-HA mice were bred by homozygous crossing to produce homozygous offspring. Animals were genotyped every second generation to ensure the presence of the transgene (sections 4.1.3, 4.1.4). Non-transgenic WT C57Bl/6NCrl control animals were purchased from Charles River Laboratories and were continuously bred in the animal facility of the DZNE.

4.5.2 Generation of the NM-HA mouse line

NM-HA mice were generated in previous, yet unpublished, work at the LIMES-GRC of the Friedrich-Wilhelms-University Bonn (#50.203.2-BN 49, 32/01). To this end, the DNA sequence encoding Sup35 NM (aa 1-253) was cloned into the *Prnp* open reading frame replacement vector pWJPrP49 (Jackson *et al.*, 2009) together with the DNA sequence encoding a hemagglutinin (HA) tag linked 3' of NM (NM-HA). Mouse embryonic stem cells (ESCs) (line V6.5) generated from C57BL/6x129SvJae (129S4) embryos were transfected with this replacement vector and cells were analyzed for successful homologous recombination. In recombinant ESCs, the endogenous open reading frame of the murine prion protein (*Prnp* gene) on chromosome 2, exon 3 was replaced by the coding sequence of NM-HA.

Consequently, NM-HA KI into the *Prnp* locus resulted in a *Prnp* KO. Confirmed ESCs were injected into blastocysts (embryonic day 3.5) from C57B/L6N mice and embryos were implanted into sham-pregnant surrogate mothers. The chimeric offspring was crossed with WT animals and upon NM-HA germline KI, animals were backcrossed to WT animals to stabilize the transgene. Finally, heterogenous NM-HA animals were crossed to generate homozygous NM-HA mice.

4.5.3 Stereotactic injections into the hippocampus

NM-HA and WT animals were stereotactically inoculated at an age of 7 to 9 weeks. Animals were injected with either PBS, monomeric recombinant NM-His, NM fibril variant F4 or F37 (figure 7 A). 30 min before surgery, animals were injected subcutaneously with 0.08 mg/kg Buprenorphin to prevent pain during and after the surgery. Mice were deeply anesthetized with 3 % isoflurane in 1000 ml/min N_2O and 400 ml/min O_2. Sufficient anesthesia depth was constantly assured by testing the toe pinch reflex. After fixing the head of the animal in a stereotaxic frame, the scalp was cut open and the skull skin was locally anesthetized by applying 2 % Lidocain gel. After removing the skin, a small hole was drilled at -2.0 mm posterior and -1.3 mm lateral from Bregma (figure 7 B). Subsequently, a glass capillary attached to a Hamilton syringe was inserted into the brain to a depth of ventral -2.2 mm from the Dura mater. 5 μg monomeric or fibrillar NM in 2.5 μl sterile PBS was unilaterally injected
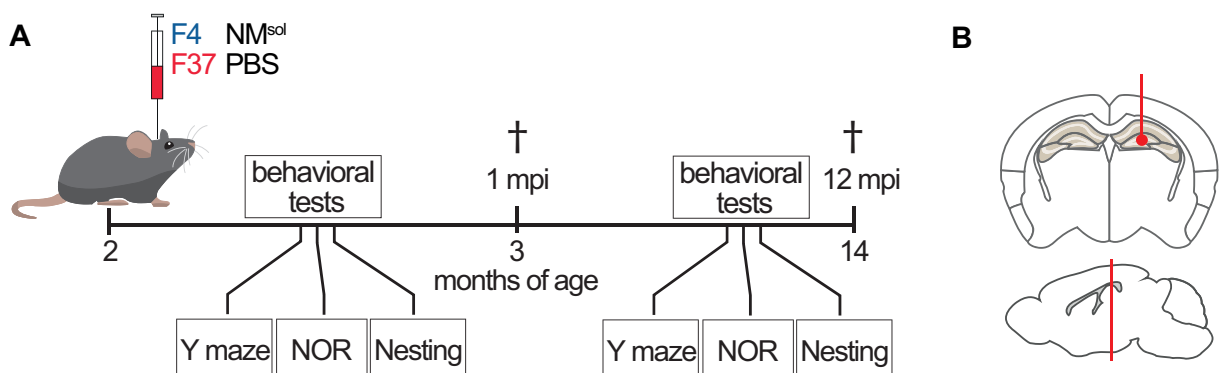
Figure 7. Schematic overview of animal experiments after stereotactic injections. A Experimental time line. 2 months-old NM-HA and WT animals were injected with 5 ng monomer equivalent F4, F37 or soluble NM (NM^{sol}). PBS was injected as control. Cognition was assessed via Y maze, Novel object recognition test (NOR) and nesting behavior before animals were sacrificed 1 mpi and 12 mpi. **B** Animals were unilaterally injected in the right dentate gyrus (from bregma: -2.0 mm posterior, + 1.3 mm lateral, - 2.2 mm ventral).

in the right dentate gyrus of the hippocampus with a flow rate of 100 nl/min using a microinjection syringe pump. 2.5 μl sterile PBS was injected as control. The capillary was left in place for 5 min before the wound was disinfected and closed with tissue adhesive. Mice were placed in a heated cage and were transferred into the home cage after full recovery. To

prevent pain and inflammation, animals were daily injected subcutaneously with 5 mg/kg Carprofen for three days post-surgery. Animals were sacrificed after 1 and 12 months post injection (mpi), PBS-injected animals were sacrificed at 8 mpi.

4.5.4 Behavioral experiments

To test hippocampus-dependent cognition of injected NM-HA animals, a series of behavioral experiments was performed 1 and 12 months post injection (figure 7 A). The day-night-cycle of all tested animals was switched to assess the behavior in the animals' active time. Before starting the experiments, animals recovered from the surgery for one week. In addition, animals were handled for 2 min for 3 consecutive days to familiarize the animals with the experimenter and the test environment. On each experimental day, animals were given 30 min in the test room to adjust to the new environment. As males and females were used in this project, males were tested first to reduce the distraction provoked by female smell. During the experiments, animals were recorded and automatically detected with three body points (EthoVision XT software, Noldus). However, as the automated detection is prone to errors, each video was also evaluated manually.

4.4.5.1 Y maze

Spatial working memory was assessed as described using a Y-shaped maze with three arms made of non-translucent plastic (Kraeuter *et al.*, 2019). Each arm was 30 cm long and 7 cm wide with a wall height of 10 cm. The animal was placed in the center of the maze and was allowed to freely explore the maze for 8 min. During that time, the animal was recorded and each arm entry was manually registered. The entrance in one arm was counted when all 4 paws entered the arm. Animals with less than 10 total arm entries were excluded. Finally, the animal was placed back in the home cage and the maze was cleaned with 70 % ethanol to remove odor cues. The spontaneous alternation rate, the consecutive visit of all 3 arms, was calculated per animal with the following formula:

$$Alternation \ (\%) = \frac{Number \ of \ alternations}{(Total \ number \ of \ arm \ entries - 2)} * 100$$

4.4.5.2 Novel object recognition (NOR)

Object recognition memory of injected animals was tested   using a white plastic box (50 cm x 50 cm x 50 cm) and different sets of objects, all varying in shape and color, randomized

across animals. An adapted NOR protocol was used (Oliveira *et al.*, 2012). The NOR consisted of three phases: the habituation phase, the training phase, and the test phase (figure 8). In the habituation phase, the animal was placed in the empty box and explored the test environment
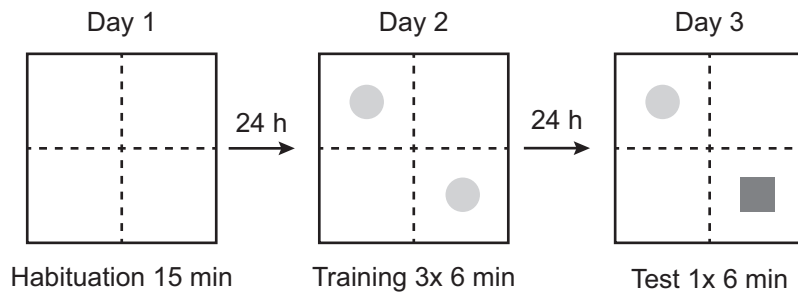
Figure 8. Procedure of novel object recognition test.

for 15 min. The animal was returned to its home cage and the box was cleaned with 70 % ethanol. 24 h after habituation, the animal was tested in 3 consecutive sessions with 6 min object training followed by 3 min break,

respectively. To this end, two identical objects were placed in two opposite quadrants of the box. The animal was placed in an empty quadrant and was allowed to explore the objects for 6 min. Afterwards, the animal was returned to its home cage for 3 min and the box and the objects were cleaned and replaced. For the test phase on the next day, one of the objects was replaced by a new object without changing the positions. The animal was placed in the box and explored the objects for 6 min. The exploration time at both objects was manually recorded when the animal was sniffing, licking, or gnawing but not when it was rearing or climbing on the object. Animals exploring the objects for less than 10 s were excluded. Subsequently, the animal was returned to its home cage and the box and the objects were cleaned. The recognition index was calculated using the following formula:

$$Recognition\ index\ (\%) = \frac{Exploration\ time\ new\ object}{Total\ exploration\ time} * 100$$

4.4.5.3 Nesting behavior

To test natural hippocampus-dependent behavior, the ability to build a nest was assessed. Animals were single caged around 1 h before the animals' active time. Each animal received a weighted cotton square nestlet but no other enrichments. After 12 hours, the built nest was scored with a value from 1 to 5 (Deacon, 2006) and unused parts of the nestlet were weighted. A score of 1 was given for an untouched nestlet and a score of 5 for a near perfect nest.

4.5.5 Mouse tissue preservation

At the appropriate time point post-injection, mice were euthanized by an intraperitoneal injection of 600 mg/kg Pentobarbital. After the respiration stopped, mice were transcardially perfused with 20 ml ice-cold PBS supplemented with 20 units/ml heparin at a flow rate of 5 ml/min to remove all blood. For molecular analysis, the brain was removed and the hemispheres were separately frozen on dry ice before storing them at -80 °C. For histological analysis, mice were additionally perfused with 20 ml ice-cold 4 % [w/v] buffered formaldehyde solution. The brain was removed and placed as a whole in 5 ml 4 % [w/v] buffered formaldehyde solution for immersion fixation at 4 °C ON. The next day, fixed tissue was washed twice in PBS before storing it in PBS supplemented with 0.01 % [w/v] sodium azide at 4 °C.

4.5.6 Mouse tissue preparation

Anti-freezing solution

13.1 mM	NaH_2PO_4
38.4 mM	Na_2HPO_4
30 % [v/v]	Ethylenglycol
30 % [v/v]	Glycerol

For histological analysis, fixed brains were quickly washed in PBS and transferred to 30 % [w/v] sucrose in PBS to prevent damaging ice crystal formation during freezing. After 48 h, the brain was removed from sucrose and attached to the cutting dish of a sliding and freezing microtome. The brain was frozen with dry ice and was cut in 35 μm coronal sections. The sections were consecutively collected in 5 wells of a 24 well plate filled with anti-freezing solution. Each well finally contained a full brain set consisting of every fifth section. The plates were stored at -20 °C until further use. For molecular analysis, the frozen right brain hemisphere was transferred to a pre-cooled mortar on dry ice. The mortar was filled with approx. 20 ml liquid nitrogen to deeply freeze the tissue. After full evaporation, the hemisphere was grinded to a fine powder using a pre-cooled pestle. 40 - 60 mg brain powder was aliquoted to pre-cooled protein low-bind tubes and was stored at -80 °C until further use.

4.6 Image analysis and Statistics

4.6.1 Quantification of NM-HA aggregates

To analyze NM-HA aggregate spreading in the brain of injected mice, 35 μm brain sections were immunohistochemically stained for HA (section 4.4.2). In total, 6 positions were selected for aggregate quantification to cover most of the brain from anterior to posterior: +0.98 mm, -0.46 mm, -2.06 mm (injection site), -3.08 mm, -3.88 mm, -5.52 mm from Bregma. 4 – 5 animals were randomly selected per treatment group, and 3 sections per animal were stained and analyzed. Each stained section was fully imaged using the automated slide scanner AxioScan 7 (Zeiss) with a 10x objective (figure 9 A). Images were taken as z-stacks of 5 slices with 3 μm intervals. For aggregate quantification, the image analysis software ARIVIS (Zeiss) was used, which allows automated large-scale analysis of full brain sections. To this end, the brain regions to be analyzed were manually defined for each section according to the Allen Reference Atlas – Mouse Brain (atlas.brain-map.org) (figure 9 B, Suppl. figure 4 A). Smaller subregions were grouped to reduce annotation time. A deep learning algorithm was trained and applied to detect the DAB signal of NM-HA aggregates in each defined area of each section (figure 9 C, D). Of note, some regions had to be excluded due to their strong structuring (e.g. the striatum, fimbria, lateral septum), which caused false-positive detection. Finally, the total surface area of the DAB signal in each brain region was normalized to the size of the respective brain region and was plotted as a heat map for each coronal position.
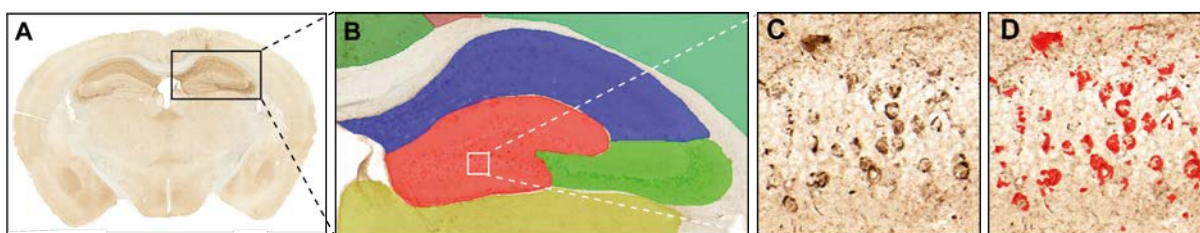
Figure 9. Workflow of automated NM-HA aggregate detection and quantification. A NM-HA deposits in the brain were detected via immunohistochemical staining with anti-HA antibodies. Each brain section was automatically imaged (AxioScan 7, Zeiss) and brain regions were manually annotated in each section according to the Allen Reference Atlas – Mouse Brain (colored areas) (**B**). **C, D** NM-HA deposits were quantified by a deep learning algorithm trained to detect the DAB signal in each defined brain region (ARIVIS, Zeiss). The total HA signal area was calculated and normalized to the size of the brain region.

4.6.2 Quantification of microglia, astroglia, and neurons

Microglia, astroglia and neurons were quantified via immunofluorescence triple staining with Iba1, GFAP and NeuN antibodies (table 5, 6) at the injection site (-2.06 mm from Bregma). 3 sections per animal were stained from the same animals analyzed for NM-HA aggregates.

Sections were fully imaged using the AxioScan 7 (Zeiss) slide scanner with a 10x objective. To reduce image sizes, a z-stack of 3 slices with 4 μm interval was used. Brain regions were defined in each section using the ARIVIS (Zeiss) software as described (section 4.6.1). For Iba-1 signal detection, an image segmentation pipeline was applied to automatically detect and count Iba1-positive cells per analyzed brain region. To quantify astroglia and neurons, image segmentation pipelines were established that automatically quantified the sum of GFAP and NeuN signal areas in each defined brain region. The signal was normalized to the size of the respective brain region and was plotted as a heat map or graph.

4.6.3 Statistics

For statistical analysis, all experiments were performed as biological triplicates. Data was analyzed using GraphPad Prism 9 (Graph Pad). Unless stated otherwise, data is shown as mean $\pm$ SD and was analyzed using a Two-way ANOVA with Bonferroni or Tukey post-hoc test. P-values below 0.05 were considered statistically significant (*$P < 0.0332$, **$P < 0.0021$, ***$P < 0.0002$, ****$P < 0.0001$.

5 Results

5.1 NM-HA in the brain of NM-HA mice remains soluble during aging

The use of the Sup35 prion domain NM (hereafter NM) as model for intracellular amyloid proteins has been a valuable tool in cells (Krammer *et al.*, 2009; Hofmann *et al.*, 2013). However, its functionality *in vivo* has not yet been investigated. In this project, we used the previously generated NM-HA mouse line, which expresses hemagglutinin-tagged NM to study NM aggregation and propagation in a more complex eukaryotic environment. As a heterologous protein, NM lacks a function in mammalian cells. Upon aggregation, NM therefore models the gain-of-function of cytosolic amyloid independent from the loss-of-function of the protein. First, NM-HA mice were characterized and analyzed for spontaneous aggregation of NM-HA with age. NM-HA is expected to be expressed at levels comparable to PrP in animals homozygous for the transgene. Western blot analysis of brain homogenates
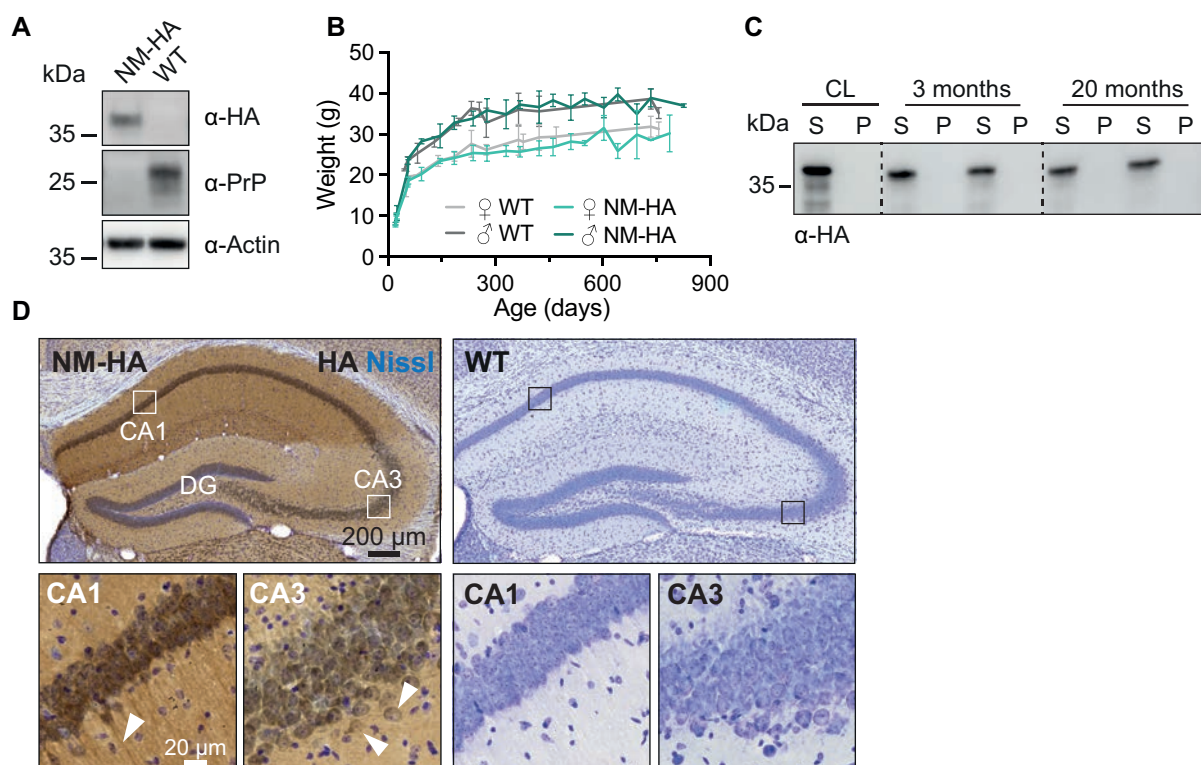
Figure 10. Characterization of the NM-HA mouse line. A Western blot of full brain homogenates shows NM-HA expression and absence of PrP in NM-HA animals. Wild type (WT) animals served as control. PrP was detected using antibody 4H11. **B** Body weights of female and male NM-HA mice compared to WT controls. Data are shown as means ± SD, n= 3-6 animals per time point. **C** Sedimentation assay with brain homogenates from young and aged NM-HA animals reveals no spontaneous aggregation of NM-HA during aging. NM-HA was detected using antibodies against the HA tag. Cell lysate (CL) from N2a cells expressing soluble NM-HA served as control. n= 3 animals per time point. Shown are 2 animals; dashed lines indicate excised lanes. **D** Immunohistochemical staining for NM-HA on brain sections from a 12 months-old NM-HA mouse (left) and an 8 months-old WT mouse (right). White and black boxes mark magnified regions. Arrowheads indicate axonal and cytoplasmic NM-HA expression. CA1/ 3: cornu ammonis 1/ 3, DG: dentate gyrus, kDa: kilodalton, MW: molecular weight, P: pellet, S: Supernatant.

from homozygous NM-HA mice confirmed the expression of NM-HA and the loss of PrP (figure 10 A). Phenotypically, NM-HA animals develop normally, breed with stable litter sizes, and increase in body weight over time like wild type (WT) animals (figure 10 B). Thus, the NM-HA KI and the lack of PrP expression have no major impact on fertility and viability in our mouse model. To investigate if NM-HA spontaneously forms aggregates during aging, brain homogenates from young and aged NM-HA mice were analyzed via sedimentation assay (figure 10 C). No NM-HA was detected in the insoluble pellet fractions of brain homogenates from aged animals, arguing that NM-HA remained soluble in the aging mouse brain. PrP is ubiquitously expressed and found in most brain regions of the mouse brain (Sjöstedt *et al.*, 2020). In line with this, staining for NM-HA in the brain of KI animals revealed region-specific expression patterns of NM-HA. High expression was found throughout the hippocampal formation, especially in the CA1 region (figure 10 D). Interestingly, a similar expression pattern has been observed in another KI mouse model, in which the *Prnp* ORF was replaced with the one coding for *GFP* (Jackson *et al.*, 2014). Within neurons, NM-HA was equally distributed in the cytoplasm and neurites, similar to other soluble cytosolic proteins. Notably, no aggregated NM-HA was found in any brain region of 12 months-old or older mice. Taken together, NM-HA animals are healthy and age without any obvious burden. Similar to NM expressed in cellular models, NM-HA in mice does not aggregate spontaneously with age and appears non-toxic. Therefore, the NM-HA mouse line was considered suitable for this project to study protein aggregation and the spread of protein aggregates in the brain.

5.2 Generation of two NM fibril conformers for intracerebral injection

Since different conformations of amyloid deposits are associated with distinct neuropathological lesions and disease phenotypes (Narasimhan *et al.*, 2017), we decided to produce different NM-His fibril variants for intracranial injection in NM-HA mice. It has previously been described that NM spontaneously polymerizes into different fibril conformers depending on the incubation temperature (Chien *et al.*, 2003; Tanaka *et al.*, 2004; Toyama *et al.*, 2007). This strategy was pursued in this work and fibrils were generated from purified, recombinant NM-His (NM from now on). Seed-free, monomeric NM in PBS pH 7.4 was incubated at 4 °C or 37 °C for 72 h without agitation (figure 11 A). The resulting spontaneously formed NM fibrils were designated F4 and F37 according to the incubation temperature during generation. To confirm that F4 and F37 fibrils contained equal amounts of NM protein, samples were analyzed via Western blot (figure 11 B). No difference in NM protein levels of F4 and F37 samples was detected. Next, we characterized the biochemical and biophysical properties of NM fibrils F4 and F37 to reveal information about the fibril conformation using

previously published methods (Tanaka *et al.*, 2004; Tanaka *et al.*, 2006; Toyama *et al.*, 2007). First, the stability of F4 and F37 was assessed by incubating the fibrils at increasing temperatures in the presence of SDS. Fibril solubilization was determined by quantifying the NM monomer band after Western blot (figure 11 C, D). At temperatures above 45 °C, both fibrils showed equal susceptibility to thermal denaturation. However, at 25 °C and 35 °C, the NM monomer signal was significantly increased in samples of fibril F4. Hence, F4 fibrils were
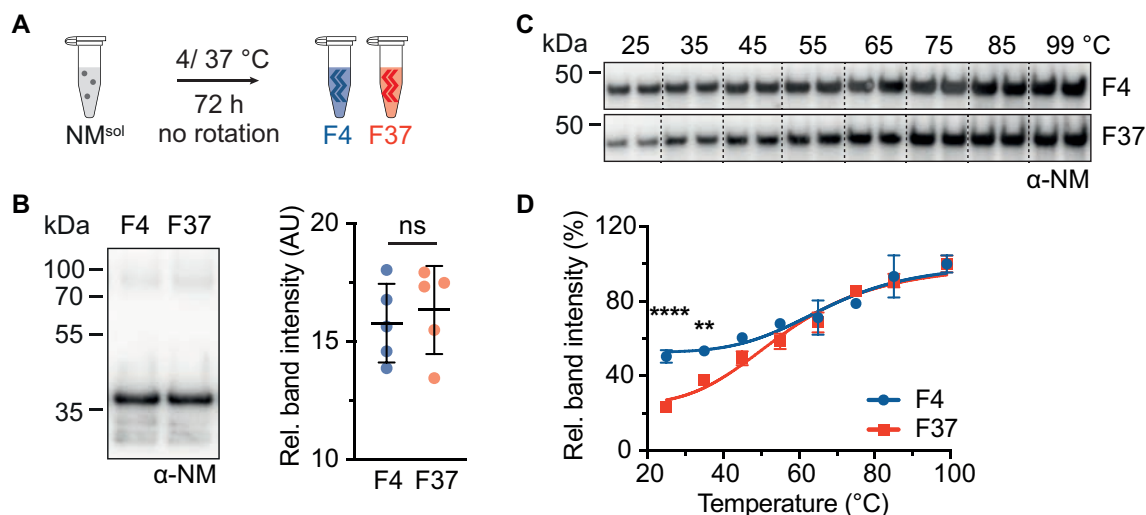
Figure 11. NM fibril F37 is more stable at physiological temperatures than fibril F4. A Fibrils F4 and F37 were generated from recombinant monomeric NM-His (NM^sol) by incubating the seed-free protein at 4 °C and 37 °C for 72 h without rotation. **B** Western blot of F4 and F37 fibrils detected with the anti-M domain antibody. Shown are two representative lanes. Quantification of the signal intensity (right graph) reveals no difference between F4 and F37 protein levels. Data are shown as means ± SD, unpaired t-test, ns indicates p > 0.05. **C** Thermal stability analysis of F4 and F37 fibrils upon incubation at different temperatures in the presence of 1 % [w/v] SDS. Monomeric NM was detected by Western blot using the anti-NM antibody. Shown are duplicates, dashed lines indicate excised lanes. **D** Quantification of the relative levels of monomeric NM from *(C)*. Data are shown as means ± SD, 3 replicates, fitted with a four-parameter logistic curve fit. Two-way ANOVA with Bonferroni post-hoc test. ** P < 0.0021, ****P < 0.0001

less stable than F37 fibrils under these conditions. In the next step, the fibril rigidity was analyzed, which is determined by the size of the amyloid core region of the fibril (Tanaka *et al.*, 2006). This biophysical characteristic can be assessed by measuring the fibril length following sonication. To this end, F4 and F37 fibrils were imaged before and after sonication using highly magnifying transmission electron microscopy (performed by Emiel Michiels, figure 12 A). Before sonication, both fibrils appeared as long twisted fibers without overt structural differences. After sonication, fibrils were fragmented into short seeds. While F37 fragments spread evenly on the grid, F4 fibrils appeared stickier and more clustered. Strikingly, the generated seeds differed in their average length, with approx. 75 nm for F4 and approx. 52 nm for F37 seeds (figure 12 B). Hence, sonication of F37 leads to shorter fragments, suggesting that F37 fibrils are less rigid than F4 fibrils.
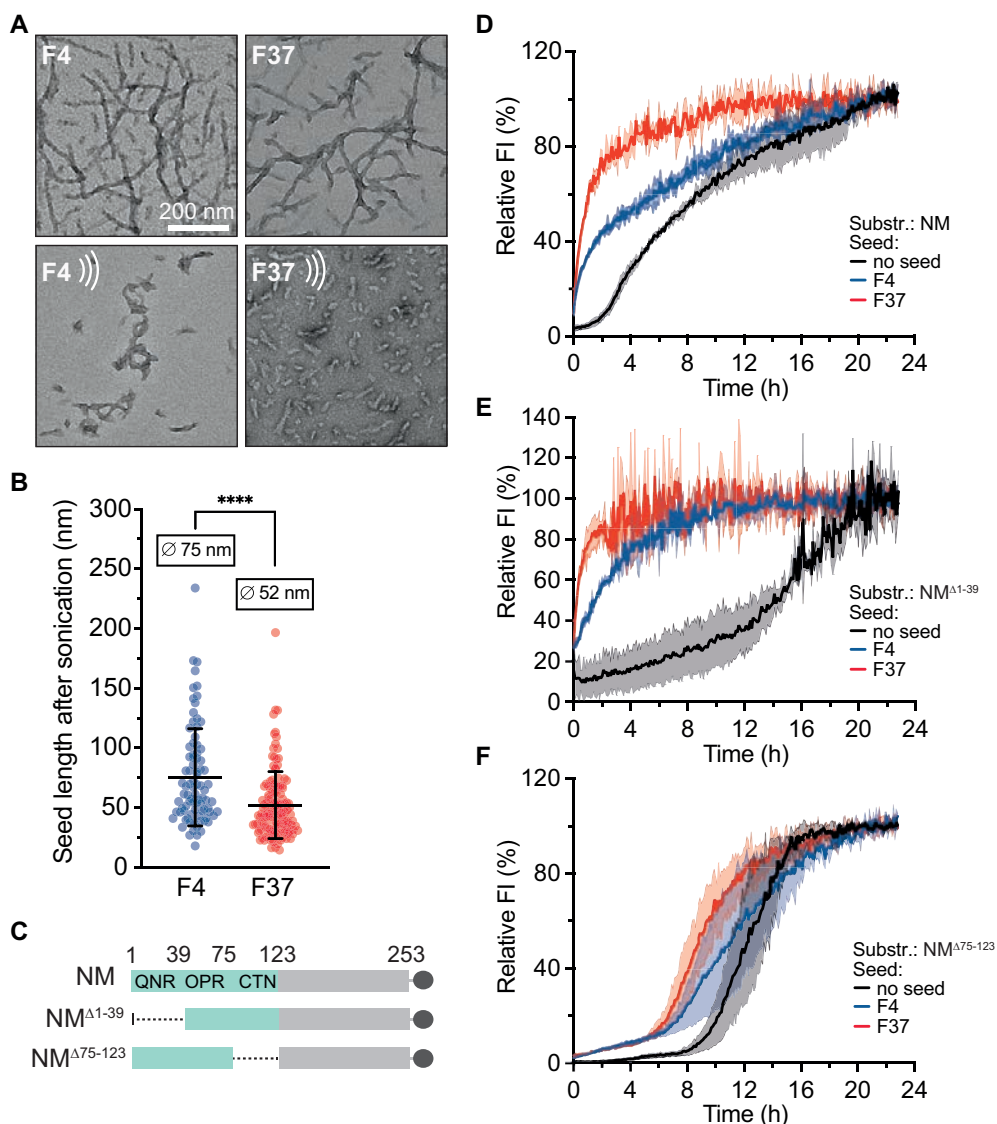
Figure 12. F4 and F37 differ in their biophysical properties in vitro. A Transmission electron microscopy images of F4 and F37 fibrils before (upper panels) and after sonication (lower panels). **B** Quantification of F4 and F37 seed lengths after sonication. The average seed lengths are indicated in boxes. Data are shown as means ± SD, unpaired t-test, ****P < 0.0001. **C** Schematic drawing of full-length NM-His and its deletion variants $NM^{\Delta 1-39}$ and $NM^{\Delta 75-123}$ used as substrate proteins for the Thioflavin-T (ThT) assay. Turquoise: prion domain, light grey: M domain, dark grey: His-tag, dashed lines indicate deleted regions. **D-F** ThT assay with His-tagged full length NM (**D**), $NM^{\Delta 1-39}$ (**E**) and $NM^{\Delta 75-123}$ (**F**) as substrate, either without fibrils or seeded with 5 % [mol/ mol] (monomer equivalent) F4 or F37 fibrils. Data are shown as means ± SD, 4 replicates.

Previous studies reported that NM prion formation in *S. cerevisiae* is mediated by the QN-rich region (QNR) of Sup35, while in mammalian cells NM prions propagation relies on the C-terminal OPR and CTN (Toyama *et al.*, 2007; Duernberger *et al.*, 2018). To reveal the prion forming region of the recombinant F4 and F37 fibrils, fibrils were tested in a Thioflavin-T (ThT) assay, in which they were used to seed different monomeric NM substrates. Substrates were either full length NM or NM mutants with deleted QNR (aa 1-39, $NM^{\Delta 1-39}$) and deleted OPR/ CTN (aa 75-123, $NM^{\Delta 75-123}$) (figure 12 C). Both fibrils seeded aggregation of full length NM and $NM^{\Delta 1-39}$, illustrated by the missing lag phase and an instant increase of the fluorescence signal

after fibril addition (figure 12 D, E). Interestingly, seeding with F37 led to higher fluorescence intensity than seeding with F4, independent of the used substrate. In contrast, the induction of $NM^{\Delta75-123}$ was weak and the lag phases of the seeded reactions were comparable to the one of the unseeded, spontaneous reaction (figure 12 F). This indicates that the C-terminal OPR and CTN (aa 75-123) are essential for seeding with F4 and F37 fibrils, while the QNR is dispensable. Furthermore, it suggests that F4 and F37 fibrils share a similar amyloid core region at the C-terminal end of the N domain.

Next, we tested if the generated NM fibrils induce NM-HA aggregation in mammalian cells. To this end, murine N2a neuroblastoma cells expressing soluble NM-HA (N2a NM-HA^{sol}) were seeded with different concentrations of sonicated F4 and F37 fibrils (figure 13 A). Treatment with soluble NM (NM^{sol}) led to no or very low induction in less than 5 % of cells at
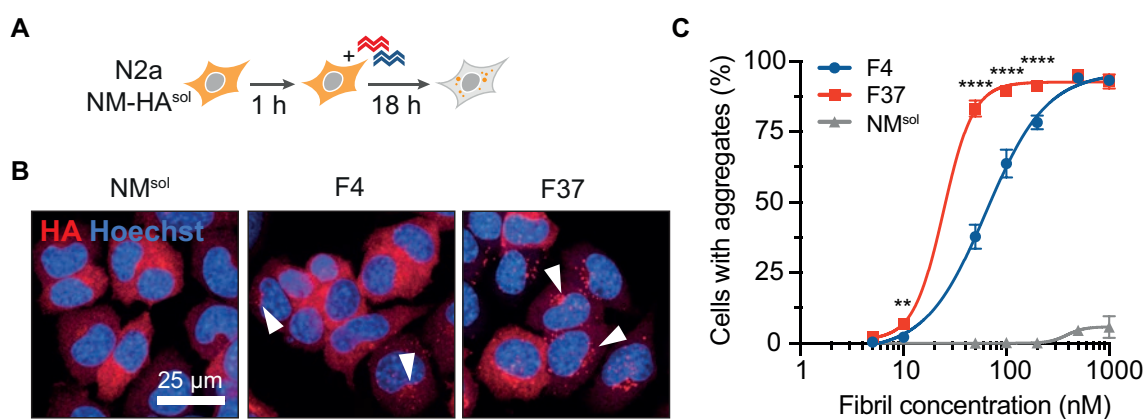
Figure 13. Fibril F37 seeds NM-HA aggregation more efficiently than F4 in NM-HA expressing N2a cells. A Experimental design. Murine N2a cells expressing soluble NM-HA (N2a NM-HA^{sol}) were exposed to sonicated F4 and F37 fibrils 1 h post plating. As a control, cells were treated with soluble NM (NM^{sol}). Cells containing NM-HA aggregates were imaged and quantified automatically. **B** Confocal images of N2a NM-HA cells seeded with 100 nM (monomer equivalent) fibrils or soluble NM. Cells were stained with anti-HA antibody and Hoechst. White arrowheads indicate intracellular NM-HA aggregates. **C** Induction of NM-HA aggregation in N2a NM-HA^{sol} cells after fibril exposure. Data are shown as means ± SD fitted with a four-parameter logistic curve fit. 4 replicates are shown. Only significant changes are indicated. Two-way ANOVA with Bonferroni post-hoc test for comparing F4 and F37. ** $P < 0.0021$, ****$P < 0.0001$.

the highest concentrations (figure 13 B, C). However, both fibrils seeded NM-HA aggregation in approx. 85 % of cells at the highest concentration. Interestingly, in the range of 50 – 200 nM, F37 induced significantly more cells (approx. 75 - 85 %) than F4 (approx. 40 - 75 %). Hence, F37 seeded NM more efficiently in cells than F4, highlighting the unique properties of both fibril conformers. Overall, NM fibrils F4 and F37 have different biochemical and biophysical characteristics and differ in their seeding activity *in vitro* and in cells. This argues that F4 and F37 are distinct fibril strains that possess distinct fibril conformations. Thus, these two fibrils were used for intracranial injections in NM-HA animals.

5.3 Mild cognitive decline in fibril-injected animals 12 mpi

Aim of this study was to investigate if NM prions can be induced in a living mammal and if NM-HA aggregates cause neurodegeneration through a toxic gain-of-function. To do this, two months-old NM-HA animals were unilaterally injected in the right dentate gyrus (DG) with 5 ng (monomer equivalent) F4 and F37 fibrils. As controls, soluble NM (NM^{sol}) and PBS were injected. Animals were sacrificed at 1 month post injection (mpi) and at 12 mpi. Mice of both sexes, equally distributed within cohorts were used in this study.

Over the course of 12 months, fibril-injected animals remained healthy without developing an overt phenotype. Since we injected in the hippocampus, we wondered if fibril inoculation led to a decline in cognition as a consequence of neurodegeneration in the hippocampus. To address this question, PBS, NM^{sol}, and fibril-injected NM-HA animals were tested in three hippocampus-dependent behavioral tests - nesting behavior, Y maze, and novel object recognition test (NOR) - before the experimental end at 1 mpi and 12 mpi. First, the natural nest-building behavior was analyzed by isolating animals and allowing them to build a nest from a cotton nestlet within 12 h. The nest quality was assessed the next day by ranking nests from score 1 for an untouched nestlet to score 5 for a near perfect nest (figure 14 A, B). At 1 mpi, injected animals were equally able to build nests with an average score of 4.3. Strikingly, after 12 months, animals inoculated with F37 fibrils built nests of lower quality (average score 3.1) compared to PBS and NM^{sol}-injected animals (average score 4.4 and 4.3), which indicates a decline in nest-building ability. A similar trend was observed for F4-injected animals (average score 3.9). No differences in nest quality were observed between males and females (Suppl. figure 1 A). To assess spatial working memory, the alternation rate of animals in a 3-armed Y maze was determined (figure 14 C-E). In this test, all animals alternated equally often and mostly above chance level, independent of the inoculum and age. Females and males alternated with an average rate of approx. 61 % and 66 % at 1 mpi and approx. 62 % and 68 % at 12 mpi (Suppl. figure 1 B). The overall amount of arm entries did not increase with age, even though aged females were more and aged males less active (Suppl. figure 1 C). In the NOR test, the memory to recognize a learned object was assessed 24 h after the last object training (figure 14 F-H). All injected animals were equally able to discriminate between the novel and old object, with mean recognition indices ranging from 65.6 % to 72.7 % in young and from 64.6 % to 68.3 % in aged animals. Additionally, animals spent similar amounts of time exploring both objects. The increased explorative behavior detected in NM^{sol}-injected animals at 1 mpi was unexpected and could be caused by an unknown bias on the test day. No differences in performance were observed between males and females (Suppl. figure 1 D, E). Together, the injection of NM fibrils in the hippocampus of NM-HA

animals did not lead to a visible phenotype. However, F37 fibril-injected animals were significantly and F4 fibril-inoculated mice were slightly impaired in nest building at 12 mpi. This indicates a mild cognitive decline in these mice. As nesting is a strongly hippocampus-dependent behavior, it suggests neuronal changes in the hippocampus. To investigate the consequences of NM fibril injection in the brain of NM-HA animals, the brain tissue was histologically and biochemically analyzed.
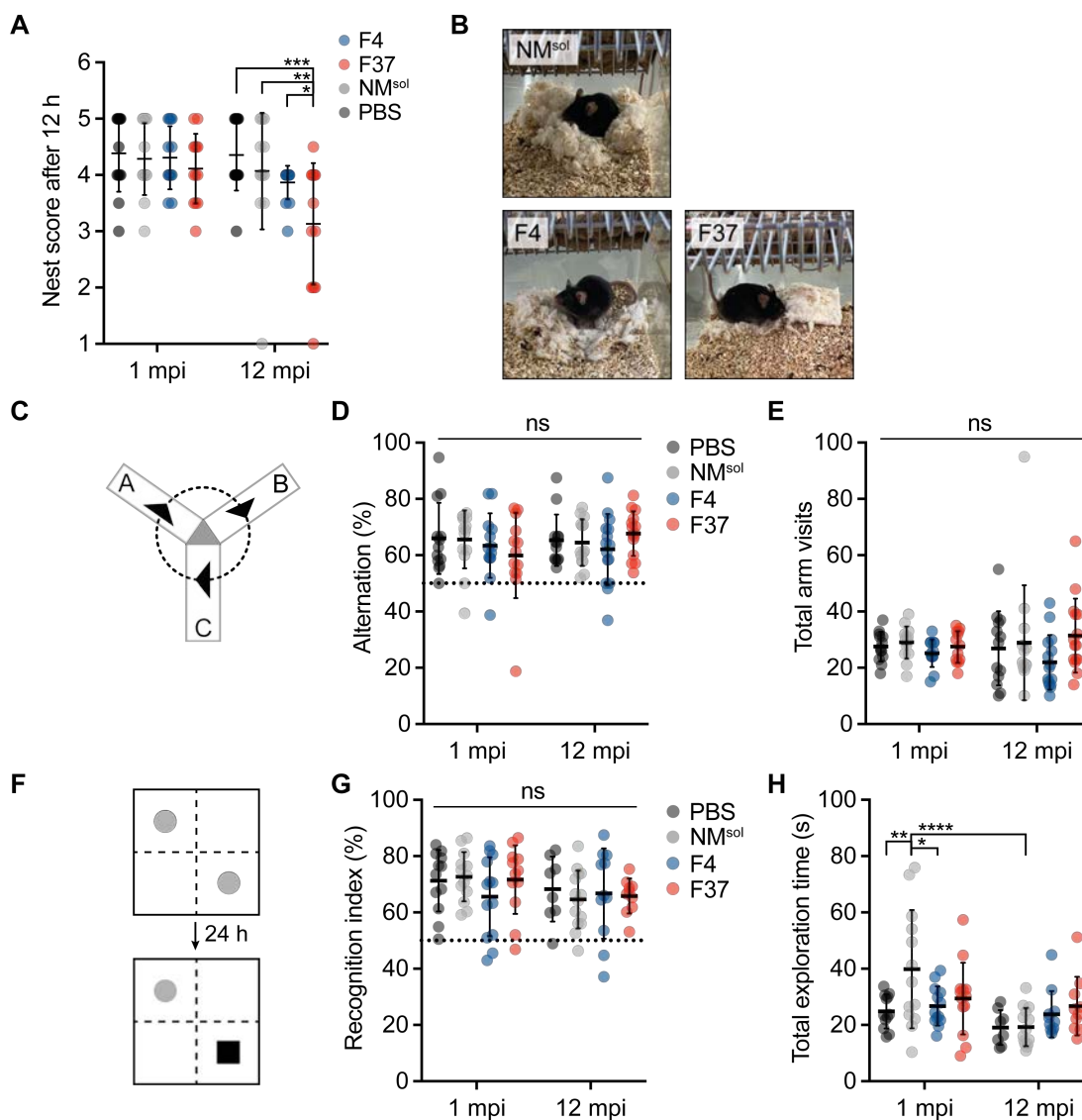
Figure 14. Fibril-injected animals show decreased nest-building ability. A Assessment of nest-building behavior shows decreased quality of nests from animals injected with F37 fibril. Animals were isolated and nests were scored from 1 (nestlet not touched) to 5 (perfect nest) after 12 h. **B** Representative nest images of animals 12 mpi. **C** Y maze test to investigate spontaneous alternation behavior. **D, E** Alternation rates (number of alternations/ number of total arm visits -2) and total arm visits of animals tested at 12 mpi were comparable with those tested at 1 mpi. **F** Novel object recognition (NOR) test to assess recognition and long-term memory. **G** Animals tested at 12 mpi were able to discriminate between the old and the novel object. Recognition index: time spent at the novel object/ time spent at both objects. **H** The total exploration time (the time spent at both objects) remained equal across groups, except for animals injected with NM^{sol} at 1 mpi. **A-H** 6-8 male and female animals were tested per condition. Data are shown as means ± SD, two-way ANOVA with Bonferroni multiple comparison test. Only significant changes are indicated. *$P < 0.0332$, **$P < 0.0021$, ***$P < 0.0002$, ****$P < 0.0001$. Dashed lines indicate the chance level.

5.4 Fibril injection in the hippocampus of NM-HA animals induces NM-HA amyloid

So far, we demonstrated that F4 and F37 seeded NM-HA aggregation *in vitro* and in mammalian cells expressing NM-HA. To determine if the injection of NM fibrils F4 and F37 in the brain of NM-HA mice induced NM-HA amyloid, injected animals were sacrificed after the behavior tests at 1 mpi and 12 mpi. Brain sections around the injection site were immunohistochemically stained for HA and imaged. NM-HA animals injected with NM^{sol} and PBS served as controls (figure 15 A). Over the course of eight months, PBS-injected animals did not develop NM-HA accumulations in the ipsilateral hippocampus or elsewhere in the
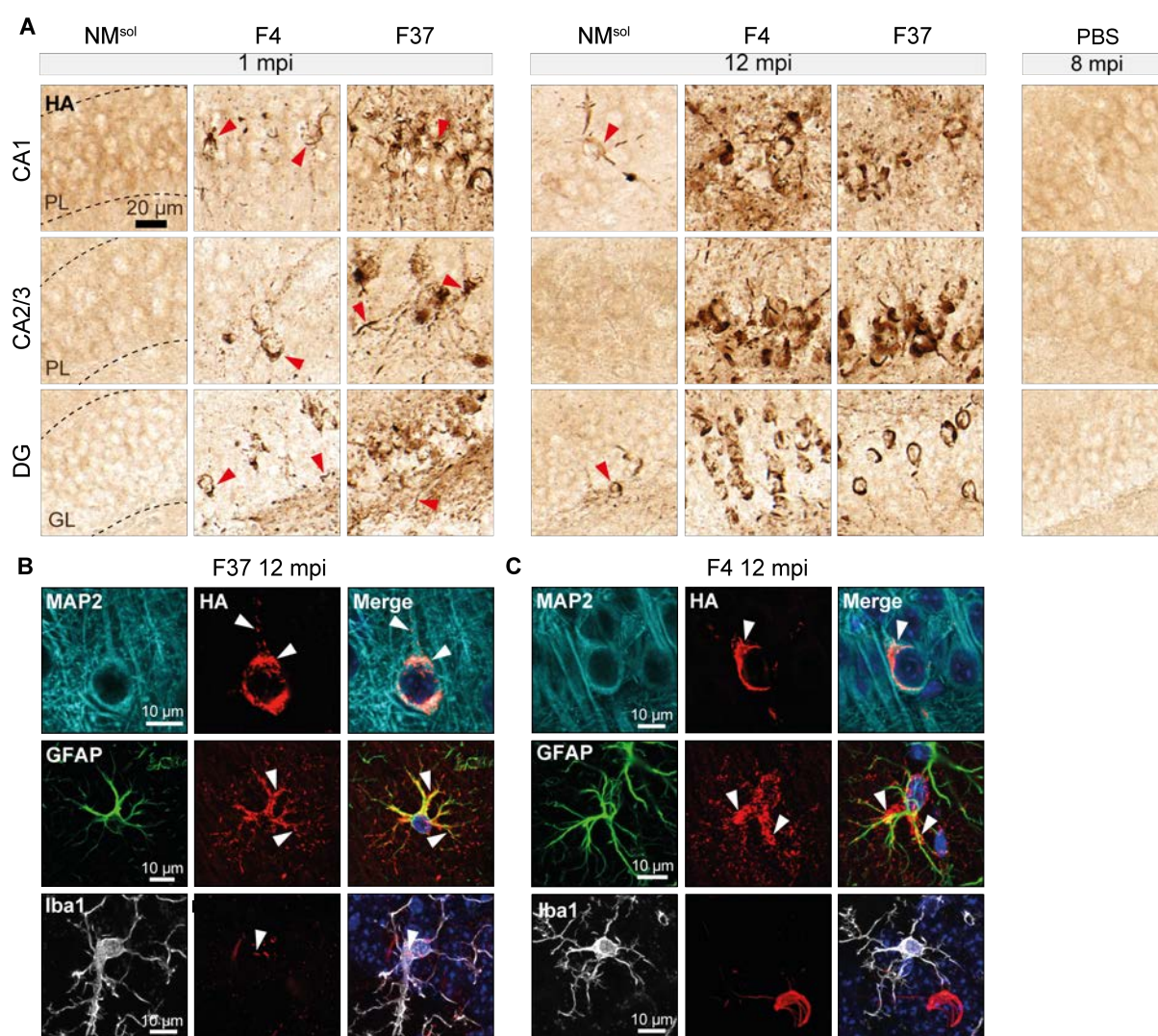
Figure 15. F4 and F37 fibril injection induces NM-HA aggregation in neurons and astrocytes. A Representative images of NM-HA aggregates in the ipsilateral hippocampus from animals injected with F4, F37 and NM^{sol} at 1 mpi (left) and 12 mpi (middle). Brain sections were immunohistochemically stained with anti-HA antibody. NM-HA accumulations were absent in PBS-injected animals at 8 mpi (right). Dashed lines indicate borders of the pyramidal layer (PL) and the granular layer (GL). **B, C** Representative confocal images of NM-HA deposits in neurons, astrocytes, and microglia in the hippocampus of F37-injected animals (**B**) and F4-injected animals (**C**) 12 mpi. Brain sections were immunofluorescently stained with antibodies against neuronal marker MAP2, astroglial marker GFAP, microglial marker Iba1, and HA. **A-C** Arrowheads indicate NM-HA deposits in the cytosol and cell processes. CA: cornu ammonis, DG: dentate gyrus.

brain (figure 15 A, right, Suppl. figure 2). Animals exposed to NM^sol lacked NM-HA deposits at 1 mpi but developed single inclusions scattered across the hippocampus at 12 mpi. This finding might be explained by the injection procedure during which NM^sol was forced through a thin glass capillary. *In vitro*, capillary-processed NM^sol seeded NM-HA aggregation in N2a NM-HA^sol cells (Suppl. figure 3). This argues that the injection of NM^sol introduced seeding-competent NM species that induced NM-HA aggregation in the brain. In fibril-injected animals, NM-HA deposits were detected in the CA1, CA2/3, and DG regions after one and 12 months (figure 15 A, left, middle). The severity of NM-HA deposition in specific brain regions somewhat differed between fibril-injected animals, even when the same fibril type was injected. In the pyramidal layer of CA1-3 and the granular layer of the DG, NM-HA aggregates appeared as fibrillar tangles around the neuronal nuclei. In subregions containing cellular processes, deposits were shaped as short fibrils and dots. Overall, NM-HA inclusions generated by F4 and F37 fibrils had similar morphologies. After 12 months, NM-HA pathology in the hippocampal subareas increased, especially in F4-injected mice. Immunofluorescence co-staining with neuronal marker MAP2 confirmed the intraneuronal localization of aggregates (figure 15 B, C). Additionally, NM-HA accumulations were found in the cytosol and processes of astroglia, while microglia contained no or only little amounts (figure 15 B, C). No NM-HA plaque formation or spongiform degeneration was observed.

To confirm that the detected deposits consisted of amyloid NM-HA, brain sections of fibril-injected animals were immunofluorescently stained for HA and were co-labelled with the amyloid-binding dye Thioflavin S (ThS) (figure 16 A, B). The co-localization of the ThS signal with NM-HA aggregates confirmed the amyloid nature of induced NM-HA deposits at 1 mpi and 12 mpi. Moreover, NM-HA amyloid co-localized with the autophagy marker p62, which binds to various disease-related amyloid (figure 16 C). The presence of insoluble NM-HA species in fibril-inoculated mice at 12 mpi was further verified by analyzing brain homogenates via sedimentation assay (figure 16 D, E). In control animals, NM-HA was detected in the soluble supernatant fraction but was absent in the insoluble pellet fraction. In fibril-injected animals, seeded NM-HA aggregates were separated from soluble NM-HA and were detected in the pellet fraction. Here, the banding pattern resembled the one from the control cell lysate, presumably detecting not fully denatured, tightly bound dimers of aminoterminally truncated NM-HA fragments. In summary, injection of F4 and F37 fibrils in the brain of NM-HA animals induced intracellular NM-HA amyloid within one month. Furthermore, NM-HA pathology increased over the course of 12 months. We conclude that a yeast prion can seed and propagate amyloid aggregates in a mammalian system *in vivo*.
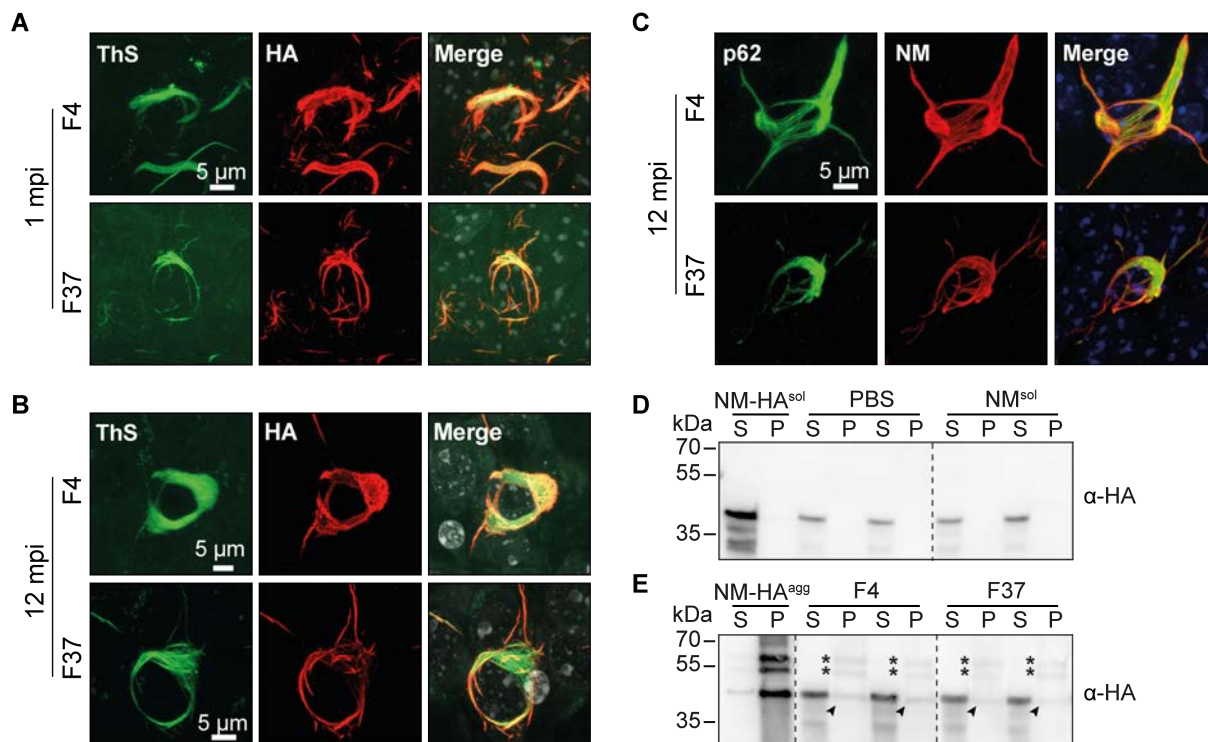
Figure 16. Fibril-induced NM-HA deposits have an amyloid structure. A, B Representative confocal images of neurons in the hippocampus of animals injected with F4 and F37 at 1 mpi (**A**) and 12 mpi (**B**). NM-HA deposits were detected via anti-HA antibodies and probed for amyloid conformation using Thioflavin S (ThS). Nuclei were stained with Hoechst. **C** Representative confocal images of NM-HA aggregates stained with anti-NM antibodies and co-labelled for autophagy marker p62 at 12 mpi. **D, E** Sedimentation assay with brain homogenate from injected animals at 12 mpi. Pellet fractions (P) were devoid of NM-HA in PBS and NM^{sol}-injected animals (**D**). Insoluble NM-HA was detected in fibril-injected animals. Arrows mark monomeric NM-HA, asterisks mark dimers of truncated NM-HA (**E**). NM-HA was visualized using anti-HA antibodies. Cell lysate from N2a NM-HA^{sol} and NM-HA^{agg} cells served as controls. n= 3 animals per condition. Shown are 2 animals; dashed lines indicate excised lanes. S: supernatant.

5.5 NM-HA aggregates spread through the brain in a prion-like manner

The spatio-temporal distribution of amyloid in the brain is characteristic of human NDDs (Braak and Braak, 1995). It is hypothesized that variable neuropathological patterns are caused by different strains of misfolded protein (Scialò *et al.*, 2019). To determine if F4 and F37-seeded NM-HA prions disseminate differently in the brain, we assessed the spread of NM-HA amyloid in inoculated animals. To this end, brain sections from animals injected with NM^{sol}, F4 and F37 were stained for HA at 1 mpi and 12 mpi (Suppl. figure 2). NM-HA aggregates were automatically quantified by a trained deep-learning algorithm in defined brain regions at six coronal positions covering the brain from rostral to caudal. For display, the NM-HA aggregate area fraction of each brain region was plotted as a heat map (figure 17, Suppl. figure 4).
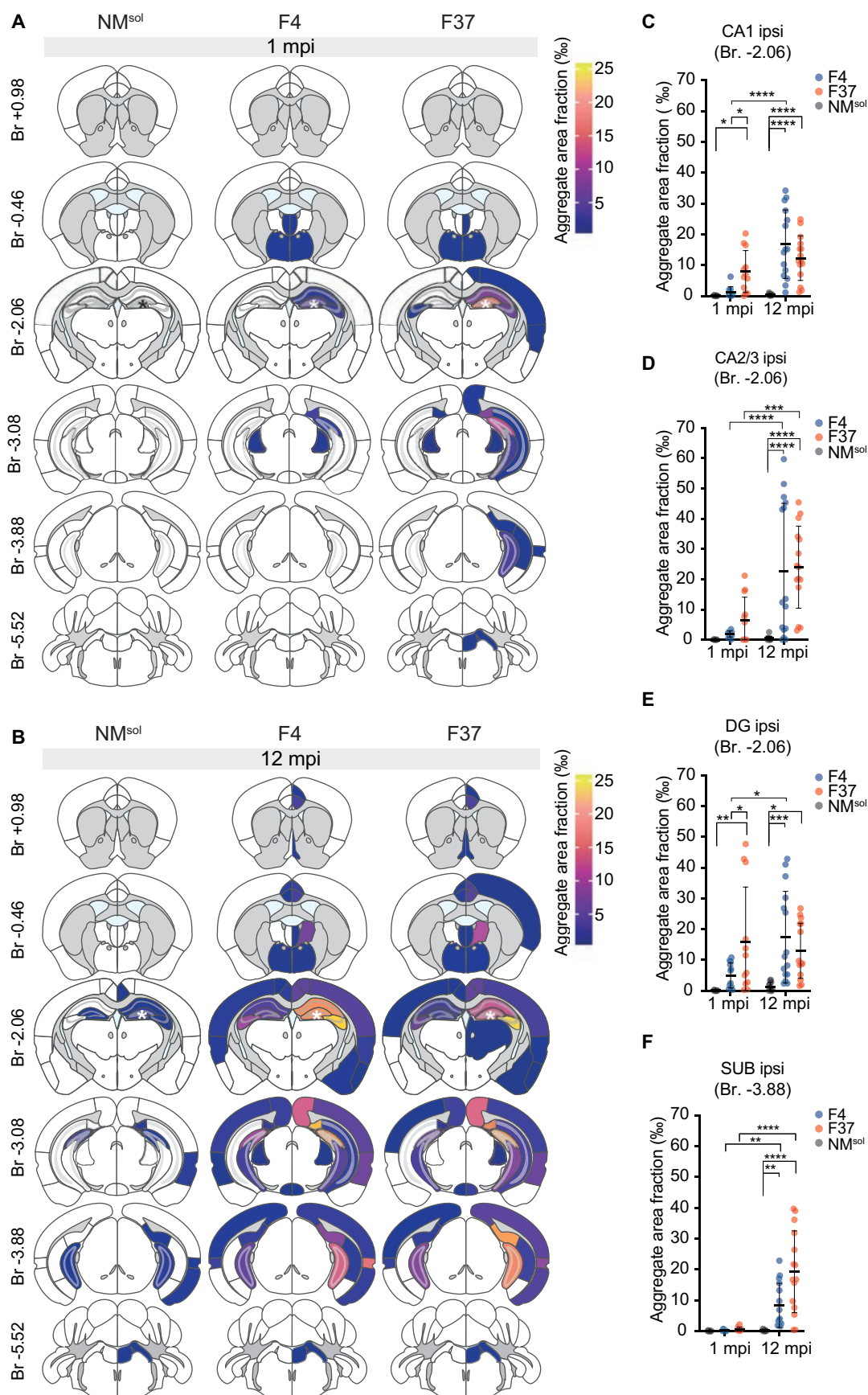
Figure 17. NM-HA prions spread to distant brain regions within 12 months. A, B Quantification of NM-HA aggregates in the brain of animals injected with NM^{sol}, F4 and F37 at 1 mpi (**A**) and 12 mpi (**B**). Brain sections were immunohistochemically stained using anti-HA antibodies and NM-HA aggregates were automatically quantified. Data are shown as heat maps depicting total aggregate surface per analyzed brain region. Brain regions with an

aggregate area fraction < 0.3 ‰ are colored in white. Ventricles are shown in light blue; grey areas are excluded. Asterisks mark the injection site. The coronal position is given in mm relative to Bregma (Br). **C-F** NM-HA aggregate quantification in representative ipsilateral (ipsi) brain regions at 1 mpi and 12 mpi. Data from A are shown as means ± SD, 3 sections/ animal, n= 4-5 animals/ condition. Two-way ANOVA with Tukey post-hoc test. Indicated are significant changes. *P < 0.0332, ** P < 0.0021, ***P < 0.0002, ****P < 0.0001. CA: cornu ammonis, DG: dentate gyrus, SUB: subiculum.

At 1 mpi, brains of animals injected with soluble NM were devoid of NM-HA aggregation in the brain (figure 17 A). In F4-inoculated mice, NM-HA pathology was mild and mainly localized ipsilaterally around the injection site (Br -2.06 mm). However, NM-HA prions also spread to the contra- and ipsilateral dorsal thalamus and hypothalamus (Br -0.46 mm), as well as to parts of the ventral hippocampus (Br -3.08 mm). Interestingly, in F37 injected animals, we observed strong NM-HA depositions in the ipsilateral hippocampus (figure 17 C, D) that propagated to the ipsilateral cortex and contralateral CA2/3 region (Br -2.06 mm). Additionally, NM-HA aggregates were found in more distal brain regions such as the ventral hippocampus, the ectorhinal and perirhinal areas (Br -3.88 mm), and the locus coeruleus (Br -5.52 mm) (Suppl. figure 5).

After 12 months, NM^{sol} injection caused sparse NM aggregation in several brain regions ipsi- and contralaterally, such as the dorsal and ventral hippocampal formation, the ventral retrosplenial area (Br. -2.06 mm), and the locus coeruleus (figure 17 B). In animals inoculated with F4 or F37, the overall amount of ipsilateral and contralateral NM-HA aggregates strongly increased (figure 17 B-F, Suppl. figure 5). F4 and F37-induced NM-HA aggregates spread to very similar brain regions and caused comparable amounts of amyloid pathology (figure 17 C-E). While protein aggregation rapidly increased in the hippocampus, deposits in more distant areas occurred later (figure 17 F). The most affected regions were the dorsal hippocampus, especially the CA3 area (Br. -2.06 mm), the ventral DG (Br. -3.08 mm) and the subiculum (Br. -3.08/ -3.88 mm). In general, NM-HA aggregates progressed from the injection site to ipsi- and contralateral frontal regions such as the thalamus, the cortex, the medial prefrontal cortex (Br. -0.46 mm) and the septum (Br. +0.98 mm). Rostrally, protein aggregation progressed to the ipsi- and contralateral ventral hippocampus, the ectorhinal, perirhinal and entorhinal areas, the retrosplenial cortex, and the subiculum (Br. -3.88 mm), until reaching the locus coeruleus. No pathology was found in the dorsal spinal cord. Together, F4 and F37 fibrils seeded NM-HA aggregation with different kinetics, highlighting F37 as more seeding competent than F4. Over time, NM-HA pathology progressively increased, arguing for a prion-like behavior of NM-HA amyloid in the mammalian brain. Furthermore, induced NM-HA aggregates disseminated via distinct routes that were similar for F4 and F37-induced aggregates.

5.6 NM-HA aggregates seed stable NM prions in mammalian cells

Next, we aimed to confirm if NM-HA aggregates in the brain of fibril-injected animals can seed aggregation of NM-HA in mammalian cells and if these induced aggregates are stably propagated. Murine N2a NM-HA^{sol} cells were exposed to brain homogenate from fibril-injected animals sacrificed at 1 mpi and 12 mpi (figure 18 A-C). 24 h post exposure, cells were analyzed for NM-HA aggregates by immunofluorescence staining with anti-HA antibodies. Cells were automatically imaged and cells containing aggregates were quantified. Brain homogenate from fibril-injected animals seeded intracellular NM-HA aggregates in all conditions (figure 18 B, C). While the induction rate of brain homogenate from animals
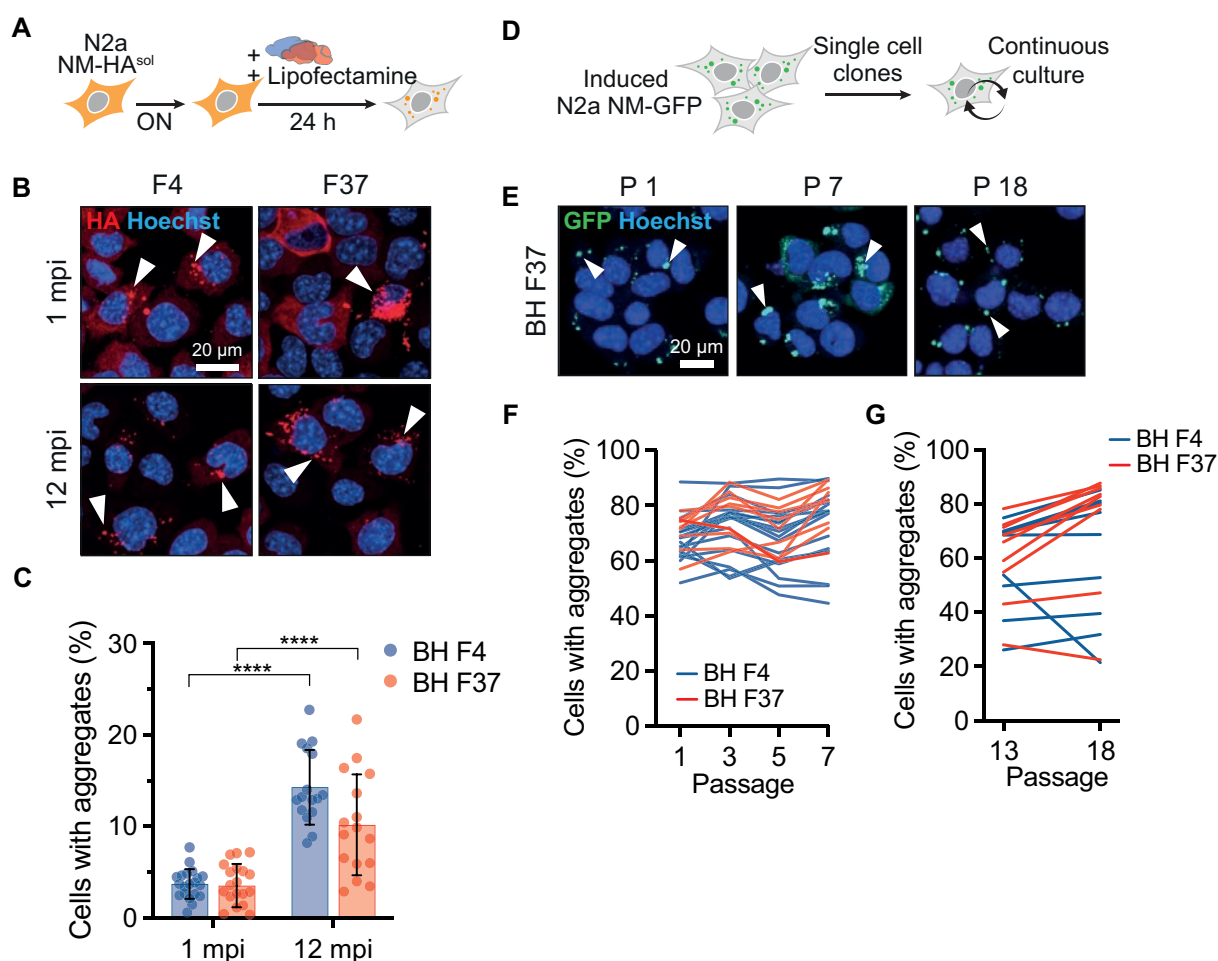
Figure 18. Brain homogenate of fibril-injected animals induces NM-HA aggregates in cells that are propagated like prions. A Experimental design. N2a NM-HA^{sol} cells were induced with a mixture of brain homogenate (BH) from fibril-injected animals and Lipofectamine. **B** Representative confocal images of NM-HA deposits in cells seeded with 55.56 ng/µl BH. Aggregates were detected via anti-HA antibodies, nuclei were stained with Hoechst. White arrows indicate intracellular aggregates. **C** Quantification of cells containing NM-HA aggregates. 4 replicates of 4 animals/ condition are shown. Two-way ANOVA with Tukey post-hoc test. Indicated are significant changes. ****P < 0.0001. **D** Experimental design. NM-GFP^{sol} cells were induced as described in (A). Single cell clones of induced cells were generated and continuously cultured. **E** Representative confocal images of one induced single cell clone at different passages. Nuclei were stained with Hoechst. White arrows indicate intracellular aggregates. **F, G** Quantification of cells with NM-GFP aggregates of several single cell clones with > 50 % of cells with aggregates at different passages (P). Each line depicts one clone. After P 13, 9 clones per condition were randomly chosen and cultured until P 18.

sacrificed at 1 mpi was around 5 %, it doubled to around 10 % when brain homogenate from the 12 mpi cohort was applied. This suggests a concomitant increase of NM-HA aggregate seeding activity with progressing brain pathology. No difference between F4 and F37 injected animals was observed. Next, we assessed the continuous NM prion propagation after induction (figure 18 D-G). For better detection, N2a cells expressing soluble GFP-tagged NM (NM-GFP^{sol}) were used. Cells were exposed to brain homogenate from F4 and F37-injected animals at 12 mpi and single cell clones were generated. Clones containing aggregates in more than 50 % of cells were chosen and continuously cultured. All clones stably propagated NM prions over 7 passages (figure 18 D-F). The average percentage of aggregate-positive cells at passage 1 and 7 remained stable and ranged from 68 % to 73 % (F4 brain homogenate) and from 71 % to 80 % (F37 brain homogenate). Randomly selected single cell clones also propagated NM prions until passage 18, even though the aggregation rate fell below 50 % in some clones (figure 18 G). Overall, the induction of NM aggregation in cells with brain homogenate from fibril-injected animals and the stable propagation of seeded NM prions in these cells are in line with the observed prion-like spread in the brain of injected animals. Thus, we conclude that NM-HA aggregates in the brain of NM-HA animals exhibit a true prion-like nature.

5.7 Hippocampal neurodegeneration in fibril-injected animals

Prion diseases and other NDDs are characterized by progressive neurodegeneration in the brain associated with increasing amounts of amyloid deposition (Jucker and Walker, 2018). NM aggregates are non-toxic in mammalian cell culture (Krammer *et al.*, 2009), but neurons in a highly complex living organism could be more sensitive. Since the hippocampus was one of the regions with the highest NM pathology and animals showed deficits in hippocampus-dependent behavior, we determined the neuronal loss in the hippocampus at the site of injection. For the quantification of neurons, brain sections from animals inoculated with F4, F37 and NM^{sol} sacrificed at 12 mpi were immunofluorescently stained for neuronal marker NeuN. Sections were imaged automatically and the NeuN-positive area within each hippocampal subregion was quantified (figure 19). In NM^{sol}-injected controls, ipsi- and contralateral neuronal populations in the pyramidal layers of the CA1-3 areas and the granule layer of the DG appeared healthy and unaffected ipsi- and contralaterally (figure 19 A, B). To exclude an effect of NM^{sol} inoculation, we quantified the neuronal area of PBS-injected animals but found no difference to NM^{sol}-inoculated animals (Suppl. Figure 6). In fibril-injected

Figure 19. Neurodegeneration in the ipsilateral CA1 region upon NM fibril injection. **A** Representative images of neurons in the hippocampus from animals injected with F4, F37 at 12 mpi. NM[sol]-injected animals served as controls. Neurons were detected via immunofluorescence staining for neuronal marker NeuN. CA1 regions are highlighted in red. Red asterisk indicates the injection site. White squares mark magnified pyramidal layers with degenerated neurons. Magnified CA3 images were derived from a different animal set. **B** Quantification of NeuN-positive area in ipsi- and contralateral CA1, CA2/3, and DG of injected animals at 12 mpi. Data are shown non-normalized as decreased sizes of brain areas introduced a bias. **C, D** Area quantification of the full hippocampus (C) and ipsilateral CA1, CA2/3, DG (**D**). The size of the ipsilateral brain region was normalized to the size of the contralateral region. **B-D** Data are shown as means ± SD, n= 4-5 animals/ condition, 3 sections/ animal. Two-way ANOVA (B, D) with Tukey post-hoc test, ordinary one-way ANOVA (C) with Dunnett's multiple comparison test. ns indicates $p > 0.05$, *$P < 0.0332$, ****$P < 0.0001$. HIP: hippocampus.

mice, no neuronal loss was detected in the contralateral hippocampus and in the ipsilateral DG. Strikingly, the medial pyramidal layer of the ipsilateral CA1 region was severely degenerated (figure 19 A, B). Moreover, neuronal loss was also detected in the CA2/3 area of mice that received F37. A similar trend was observed in F4 inoculated mice. The neuronal loss caused the entire ipsilateral hippocampus to shrink (figure 18 C). Especially the CA1 region decreased in size to approx. 83 % in F4 and approx. 74 % in F37 injected animals compared to NM[sol] treated controls (figure 18 D). Sizes of the CA2/3 area and the DG remained unchanged. Together, we found that the injection of NM fibrils led to the loss of pyramidal neurons in the ipsilateral CA1 but also in the CA2/3 region of the hippocampus. Furthermore, the data suggests that F4 and F37 injections resulted in comparable toxicity after 12 months. We conclude that a non-disease related protein in its prion conformation induced

neurodegeneration. Thus, NM-HA aggregation likely elicits mechanisms of toxicity that might also be common in NDDs.

5.8 Neuronal loss is accompanied by reactive astrogliosis and activated microglia

Neurodegeneration in prion diseases and other NDDs is associated with inflammatory responses, such as microgliosis and astrogliosis in affected brain regions (Carroll and Chesebro, 2019; Leng and Edison, 2021). To determine if NM-HA prions also cause inflammation, we assessed the quantity and morphology of glia cells in degenerated hippocampal regions. To this end, brain sections analyzed for neuronal loss were immunofluorescently co-labelled with the astroglial marker glial fibrillary acidic protein (GFAP) and the microglial marker Iba1. For quantification, the GFAP-positive area and the number of Iba1-positive cells were automatically detected in each hippocampal region (figures 20, 21). Over the course of 12 months, astroglia in the contralateral hippocampus remained unaffected in all analyzed animals, while changes were observed in the ipsilateral hippocampus. At 1 mpi, the GFAP-positive area in the CA1-3 areas of fibril-injected mice was comparable to control animals (figure 20 A top, C, D). The heat map of F37-injected animals depicts a bias from one animal with high response in the CA1 area (figure 20 C). In the ipsilateral DG of fibril-inoculated mice, the GFAP-positive area was increased compared to controls. Hence, at the site of injection, astroglia reacted to fibril injection. Of note, no differences in GFAP signals of PBS and NM^{sol}-injected animals were detected (Suppl. figure 7 A). After 12 months, the GFAP signal of the DG decreased to levels comparable to the control (figure 20 A, bottom, E). Astroglia in the CA2/3 area remained unchanged. Strikingly, astrocytes were reactive in the ipsilateral CA1 area of fibril-injected animals (figure 20 C). In the medial CA1, astrocytes developed a drastically altered morphology and clustered around the pyramidal cell layer. (figure 20 B). Thus, fibril injection caused local reactive astrogliosis firstly in the DG and at later stages in the ipsilateral CA1 area. Furthermore, F4 and F37 fibrils induced very similar responses in the brain of inoculated animals.

Next, we determined potential microglial changes. At 1 mpi, no changes in microglia numbers in the ipsi- or contralateral hippocampus of all analyzed mice were detected (figure 21 A). Microglia were evenly distributed and showed a ramified morphology. This indicated that fibril inoculation did not lead to microglia activation at the injection site 1 mpi. After 12 mpi, the microglia density in the contralateral and ipsilateral hippocampus of NM^{sol} and fibril-injected animals increased compared to 1 mpi (figure A). To verify whether this was an
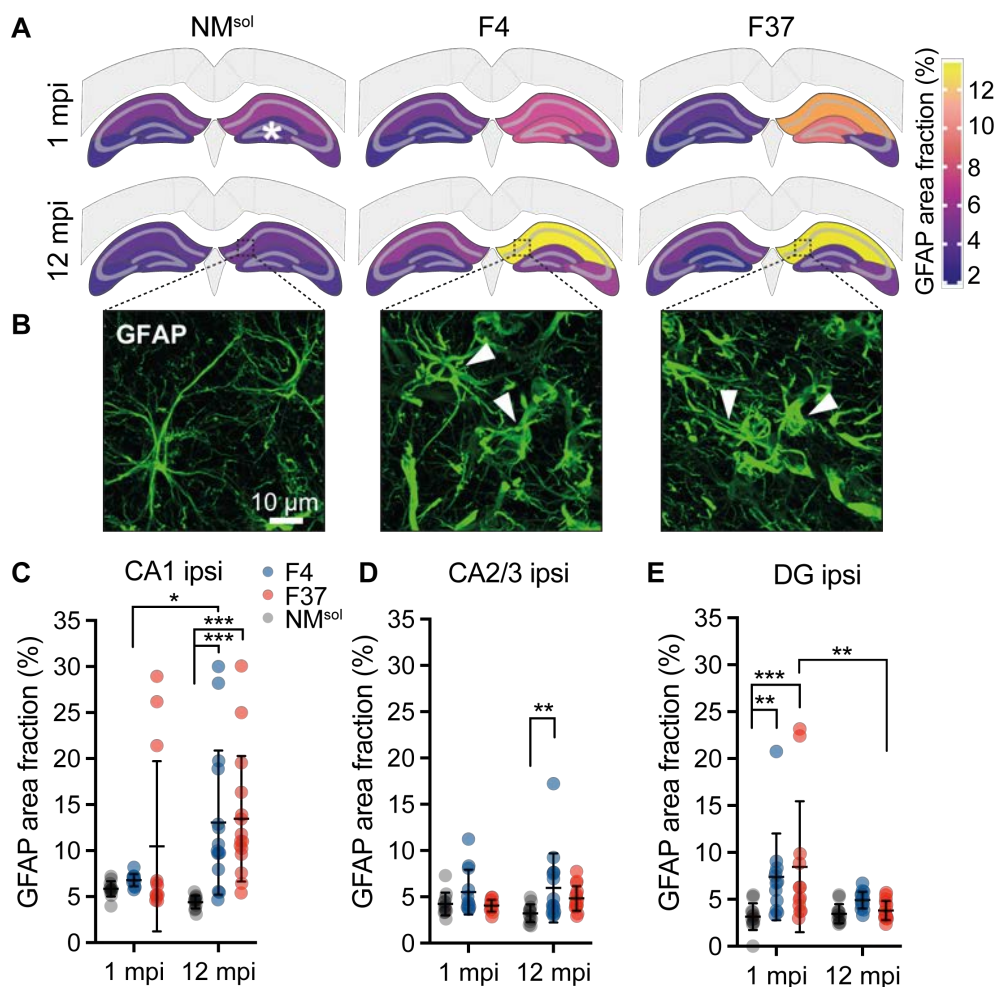
Figure 20. Severe astrogliosis in the ipsilateral CA1 region of fibril-injected animals 12 mpi. A Quantification of astrocytes in the hippocampus of injected animals 1 mpi (upper panels) and 12 mpi (lower panels). Brain sections were stained for astroglial marker GFAP and the GFAP-positive area was quantified automatically and normalized to the size of the brain region. Data are shown as heat maps using 3 sections/ animal and 4-5 animals/ condition. **B** Representative confocal images of morphologically changed astrocytes (arrowheads) in the ipsilateral (ipsi) CA1 region 12 mpi. **C-E** Quantification of GFAP signal in CA1 (C), CA2/3 (D) and DG (E) shows increased response in ipsilateral CA1 in fibril-injected animals 12 mpi. Data from (A) are shown as means ± SD, two-way ANOVA with Tukey post-hoc test. Indicated are significant changes. *P < 0.0332, ** P < 0.0021, ***P < 0.0002. White asterisk indicates injection site. CA1-3: cornu ammonis 1-3, DG: dentate gyrus.

inoculum-specific effect, microglia from animals injected with PBS were analyzed (Suppl. figure 7 B). Microglia density in PBS-inoculated mice was decreased in the ipsi- and contralateral hippocampus. Microglia numbers in young and aged, untreated WT and NM-HA animals increased with age independent of the transgene (Suppl. figure 7 C). Together, this argues for an inoculum-specific effect and suggests a time-dependent microglial response to the introduction of recombinant NM protein. On the ipsilateral side, microglial densities in the CA2/3 and DG remained unaffected by fibril injection (figure 21 D, E). Interestingly, microglia numbers strongly increased in the ipsilateral CA1 region (figure 21 C). While microglia in NM^{sol}-injected animals remained ramified, they severely changed their morphology to a highly activated, amoeboid state in the medial CA1 area of fibril-injected mice (figure 21 B). The morphological change was accompanied by an increased expression of the activation marker
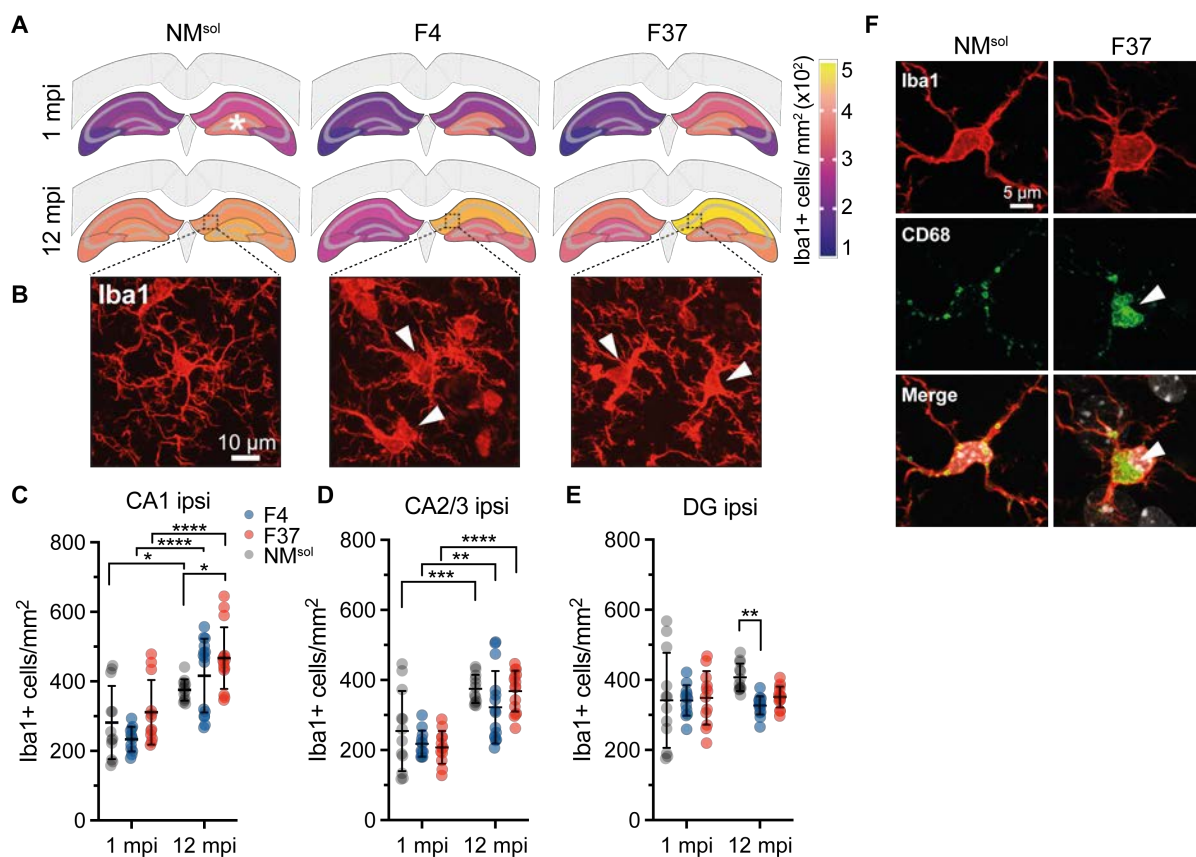
Figure 21. Reactive microglia in ipsilateral CA1 upon fibril injection. **A** Quantification of microglia in the hippocampus of injected animals 1 mpi (upper panels) and 12 mpi (lower panels). Brain sections were stained for microglial marker Iba1 and positive cells were detected and counted automatically per region. Data are shown as heat maps plotting Iba1-positive cells/ mm^2 brain region from 3 sections/ animal and 4-5 animals/ condition. **B** Representative confocal images of microglia in the ipsilateral CA1 region 12 mpi. Arrowheads indicate activated microglia with changed morphology. **C-E** Microglia quantification in CA1 (C), CA2/3 (D) and DG (E) revealed increased microglia numbers in the ipsilateral CA1 region of fibril-injected animals 12 mpi. Data from **A** are shown as means ± SD, two-way ANOVA with Tukey post-hoc test. Indicated are significant changes. *$P < 0.0332$, ** $P < 0.0021$, ***$P < 0.0002$, ****$P < 0.0001$. White asterisk indicates injection site. CA1-3: cornu ammonis 1-3, DG: dentate gyrus, ipsi: ipsilateral. **F** Representative confocal images of microglia in brains from animals injected with NM^{sol} and F37 stained for Iba-1 and co-labelled for microglial activity maker CD68. White arrows indicate large CD68 inclusions.

CD68 (figure 21 F, Suppl. figure 7 D). Again, microglia responded similarly to the injection of F4 and F37 fibrils. In summary, fibril injection into the hippocampus caused a mild astroglial response in the DG after one month. Over the course of 12 months, severe astrogliosis and reactive microgliosis developed locally in the ipsilateral CA1, in line with the neurodegeneration found in this area. As other hippocampal areas with strong NM-HA pathology, e.g. CA2/3, were not affected, it suggests a specific vulnerability of the CA1 area to NM-HA amyloid.

5.9 Chaperone valosin-containing protein (VCP) mediates NM-HA seed formation in cells

So far, we discovered that fibril-injected animals develop neurodegeneration in the hippocampus but do not show an overt phenotype at 12 mpi. This suggests that NM-HA prions are either not very toxic within 12 months, or that neurons and astrocytes use cellular mechanisms to keep the aggregates in balance to ensure cell survival. How intracellular aggregates are disassembled and degraded in mammalian cells is yet to be determined. In a recent study, Saha and co-workers (2023) identified the chaperone valosin-containing protein (VCP) as a regulator of tau fibril disaggregation. They hypothesized that VCP acts on ubiquitinylated tau amyloid in conjunction with Hsp70. As VCP has also been identified in the interactome of NM-HA prions in N2a NM-HA[agg] cells (Riemschoss *et al.*, 2019), we wondered if VCP was involved in the disaggregation and/or seed formation of NM-HA aggregates. To verify an association of VCP, Hsp70, and Ubiquitin with NM-HA amyloid, brain sections of fibril injected animals at 12 mpi were immunofluorescently stained for NM-HA and co-labelled with antibodies against ubiquitin, Hsp70, and VCP (figure 22 A-C). As expected, NM-HA amyloid co-localized with ubiquitin, which labels aberrant proteins for degradation. Most importantly, NM-HA aggregates also co-localized with Hsp70 and VCP, suggesting that VCP and Hsp70 interact with NM-HA prions in fibril-injected NM-HA animals.

To further investigate the potential role of VCP in the disaggregation of NM-HA aggregates, we performed a pilot experiment using our NM cell systems. By co-culturing cells, the transmission of NM seeds from donor cells propagating aggregated NM-HA (HEK NM-HA[agg]) to recipient HEK cells expressing soluble NM-GFP (HEK NM-GFP[sol]) was determined. To improve membrane contact and fusion between donor and recipient cells (both required for aggregate transmission), the donor was transiently transfected to express the vesicular stomatitis virus glycoprotein (VSV-G) (S. Liu *et al.*, 2021). In addition, donor cells were treated with the small molecule inhibitor NMS-873, which allosterically inhibits VCP. Shortly, donor HEK NM-HA[agg] cells were transiently transfected with an empty plasmid or a plasmid coding for VSV-G (figure 22 D). 6 h post transfection, VCP inhibitor NMS-873 or the equivalent DMSO solvent was added to the donor cells. After 24 h, treated donor cells were co-cultured with recipient HEK NM-GFP[sol] cells and the induction of NM-GFP aggregates in recipients was automatically quantified the next day. Without the expression of VSV-G in donor cells, aggregate induction in the recipient NM-GFP[sol] cells was below 3 % without a detectable effect of VCP inhibition (figure 22 E, F). In contrast, when the donor expressed VSV-G and was treated with DMSO, the induction rate increased to approx. 30 %. Strikingly, inhibiting VCP in VSV-G-expressing donor cells caused a substantial decline in aggregate
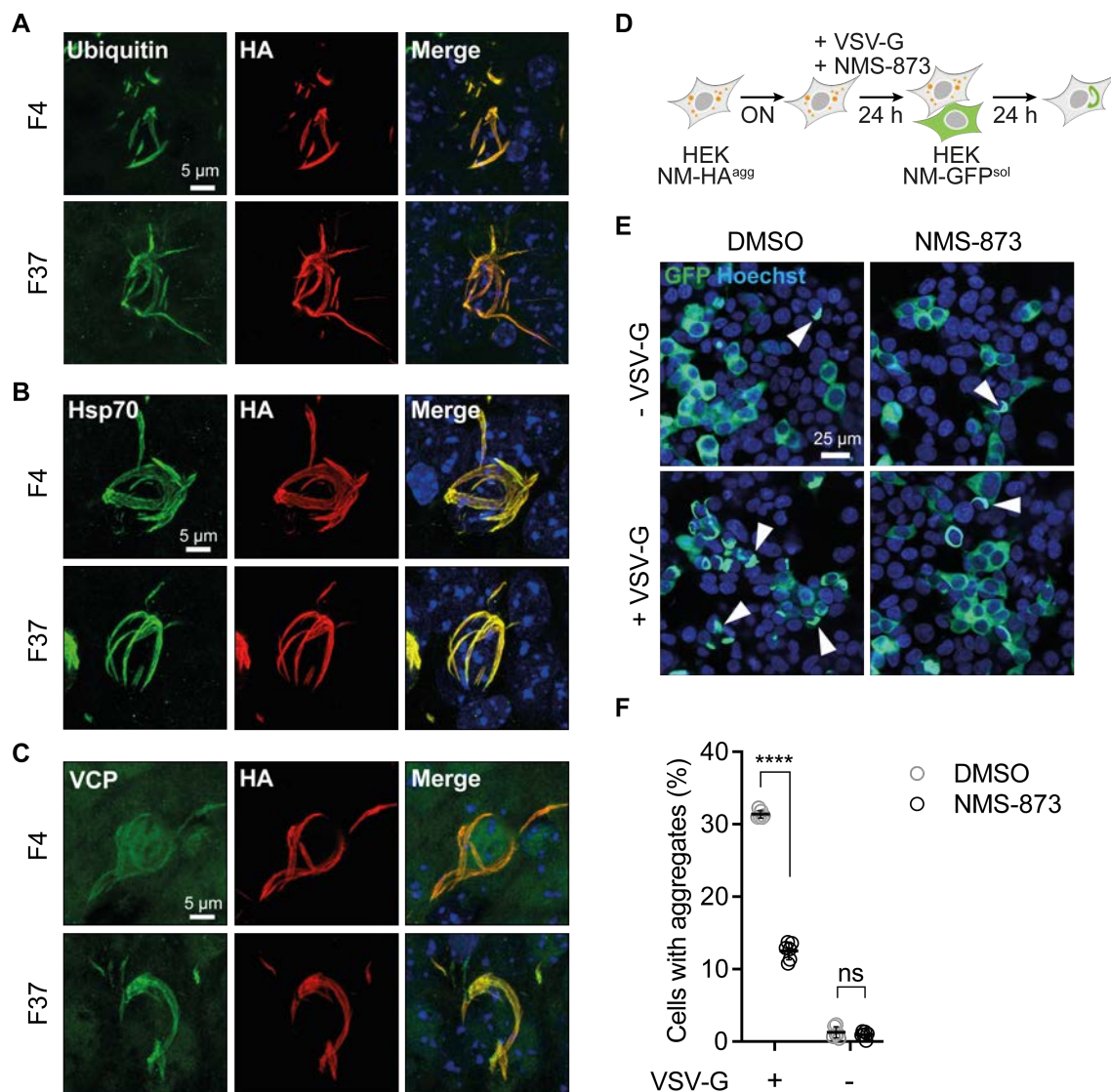
Figure 22. Inhibition of valosin-containing protein VCP decreases NM seed formation in cells. A-C Representative confocal images of immunofluorescence staining for Ubiquitin, Hsp70, and VCP co-localizing with NM-HA amyloid. Aggregates were imaged in the ipsilateral CA1 region of the brain from mice inoculated with F4 or F37, sacrificed 12 mpi. NM-HA was detected using anti-HA antibodies and nuclei were stained with Hoechst. **D** Experimental design. Donor HEK cells propagating NM-HA^{agg} were transfected with plasmid coding for the vesicular stomatitis virus glycoprotein (VSV-G) to increase intercellular contact in co-cultures. Donor cells were treated with VCP inhibitor NMS-873 or DMSO overnight (ON). Donors were co-cultured with recipient HEK NM-GFP^{sol} cells and NM-GFP aggregate induction was quantified automatically. **E** Representative confocal images of co-cultures. Arrowheads mark recipient cells with induced NM-GFP aggregates. Note that donor cells were not stained. **F** Percentage of recipient cells with induced NM-GFP aggregates following co-culture with donors +/- VSV-G expression and +/- NMS pre-treatment. DMSO served as a solvent control. Data are shown as means ± SD from 6 replicates, two-way ANOVA with Bonferroni's multiple comparisons test. ns indicates $p > 0.05$, ****$P < 0.0001$.

induction to approx. 12 % of recipients. Interestingly, this is in line with the findings of Saha et al. (2023). It suggests that the inhibition of VCP reduced the amount of transmittable NM-HA seeds in donor cells, leading to lower induction rates. Thus, VCP might be involved in the generation of seeding-competent NM species. Together, the above results highlight VCP as potential disaggregase of NM amyloid in cells and potentially *in vivo*. However, since VCP is

also involved in virus replication and release (Das and Dudley, 2021) and NMS-873 was described as potential antiviral drug (J. Zhang *et al.*, 2019), an effect on intercellular transmission cannot be excluded. Thus, future experiments should test the effect of VCP on NM aggregates *in vitro* and in cells via VCP knock-down or overexpression. Ultimately, identifying the mechanisms of protein amyloid disassembly is essential to interfere with or slow down disease progression in NDDs and prion diseases.

6 Discussion

To study human NDDs *in vivo*, numerous mouse models have been established that closely recapitulate certain pathological aspects of disease (Dawson *et al.*, 2018). Many of these models require the intracerebral injection of amyloid proteins to induce protein aggregation and disease in mice. However, while seeding protein aggregation is often successful, most mouse models fail to recapitulate other disease characteristics, such as neuroinflammation, neuronal loss, or cognitive decline (Iba *et al.*, 2013; Masuda-Suzukake *et al.*, 2013; Narasimhan *et al.*, 2017). Consequently, important factors such as neurotoxic functions of protein aggregates and cellular mechanisms of amyloid fragmentation and dissemination are yet only partially understood. In this project, we used the NM-HA KI mouse line, which expresses the amyloidogenic yeast prion domain NM, to investigate the gain-of-function of NM-HA amyloid and their dissemination in the brain of NM-HA animals. We found that the inoculation of two NM fibril polymorphs, F4 and F37, into the brain of NM-HA mice induced NM-HA aggregation within 1 mpi. Animals survived until 12 mpi without an obvious phenotype but showed impairments in nest building. Strikingly, F4 and F37 induced NM-HA prions propagated from the injection site to various ipsi- and contralateral brain regions and caused hippocampal neurodegeneration and inflammation. Our results highlight that the gain-of-function of amyloid strongly contributes to neurodegeneration. In addition, the NM-HA model recapitulates important features of NDDs and suggests shared mechanisms underlying amyloid dissemination and toxicity in mammals.

6.1 The yeast prion domain NM stably replicates in a mammalian host

To study mechanisms of intracellular amyloid propagation, the *S. cerevisisae* Sup35 prion domain NM has been used as model protein for many years. In mammalian cells expressing NM, NM prions are inducible by exogenous NM seeds and are stably transmitted vertically and horizontally (Krammer *et al.*, 2009; Hofmann *et al.*, 2013). In this project, we demonstrated for the first time that NM prions also successfully propagate in a living species of a different phylogenetic kingdom: in mice. Injection of recombinant NM fibrils seeded NM aggregates in the brain of NM-HA mice. Strikingly, NM pathology increased over time, arguing for a prion-like replication of NM prions in mammals. Since metazoa lack a Hsp104 homologue for the disaggregation of Sup35 prions (Chernoff *et al.*, 1995), a functional equivalent machinery must exist that fragments NM-HA aggregates into infectious seeds in mice. In the brain of injected animals, NM-HA deposits were decorated with ubiquitin and p62. This suggests that the cells

targeted aggregated NM-HA for degradation via the UPS and autophagy (Chen *et al.*, 2011). However, the persistence of NM-HA amyloid until 12 mpi indicates that cells were unable to fully disassemble or clear NM-HA prions. Interestingly, NM-HA aggregates also co-localized with the chaperone Hsp70. In yeast, Hsp70 homologs are involved in Sup35 prion replication (Allen *et al.*, 2005). Furthermore, Hsp70 is hypothesized to be a key player in amyloid disassembly in mammals together with chaperones Hsp40 and Hsp110 and hence, could mediate NM-HA fragmentation (Shorter, 2011; Nillegoda *et al.*, 2018). This is supported by the finding that this tri-chaperone system is able to depolymerize and fragment amyloid fibrils of tau and α-synuclein *in vitro,* thereby producing seeding-competent species (Gao *et al.*, 2015; Nachman *et al.*, 2020; Wentink *et al.*, 2020). Curiously, the interactome of NM-HA aggregates in N2a cells also included Hsp110 (Riemschoss *et al.*, 2019). However, homologs of the yeast chaperones Hsp70, Hsp40, and Hsp110 (Sse1, Ssa1, and Sis1) failed to disassemble Sup35 prions *in vitro* (Shorter 2011). Hence, the tri-chaperone system might not be the main contributor in disaggregating NM aggregates. Strikingly, NM-HA deposits in fibril-injected animals were additionally decorated with the mammalian chaperone VCP. VCP is a hexameric AAA$^+$ ATPase that is involved in a multitude of processes, mediating cellular homeostasis and proteostasis, amongst others (Kobayashi *et al.*, 2007; Meyer and Weihl, 2014). In the cell, VCP interacts with ubiquitinated proteins, disassembles protein complexes and assists in the degradation of misfolded proteins via ER-associated degradation (ERAD) or the UPS (Rabinovich *et al.*, 2002; Meyer *et al.*, 2012). Saha *et al.* (2023) argued that VCP disassembles tau aggregates together with Hsp70 in a ubiquitin-dependent manner. Strikingly, NM-HA prions in fibril-injected animals co-localized with VCP as well as Hsp70 and ubiquitin. This raises the question whether NM-HA aggregates could be fragmented by a similar mechanism. This idea is supported by the detection of VCP in the interactome of aggregated NM-HA, but not monomeric, soluble NM-HA in N2a cells (Riemschoss *et al.*, 2019). Although it was reported that the yeast VCP homologue Cdc48 had no influence on Sup35 seeding *in vitro* (Shorter and Lindquist, 2006), the inhibition of VCP in HEK NM-HA[agg] donor cells decreased seeding in recipient cells in our pilot experiment. This is in line with findings from Saha *et al.* (2023) and suggests that VCP might be involved in the formation of transmissible seeding-competent NM particles. However, the exact role of VCP in replicating NM prions remains to be determined. Remarkably, recent data also suggests the involvement of VCP in the disaggregation of tau, α-synuclein, and TDP-43 filaments *in vitro* (Darwich *et al.*, 2020; Zhu *et al.*, 2022; Phan *et al.*, 2023). However, from these data it remains unclear if VCP activity promotes or prevents amyloid seed formation or if VCP plays a dual role (Batra *et al.*, 2023). Overall, VCP is a promising candidate as amyloid disaggregase, as mutations of VCP have also been identified to cause human NDDs, characterized by the accumulation of

tau or TDP-43 amyloid in the brain (Schröder *et al.*, 2005; Darwich *et al.*, 2020). Hence, the modulation of VCP activity could be a potential therapeutic target with the aim to ameliorate amyloid burden in NDDs.

6.2 NM-HA aggregates induce a neurotoxic gain-of-function

Concomitant with NM-HA prion dissemination in fibril-injected NM-HA animals, neurons in the ipsilateral hippocampus degenerated within 12 mpi and mice exhibited decreased nest-building activity. Since neurons in the contralateral hippocampus with little or no NM-HA deposits did not degenerate, we conclude that NM-HA aggregates are linked to neurotoxicity. To our knowledge, this is the first study that demonstrates that a non-mammalian and non-disease-related protein is able to cause neurodegeneration upon aggregation in mice. Since NM-HA does not share sequence similarity with mammalian proteins and it is not known to fulfill any physiological function, the NM-HA model recapitulates solely the gain-of-function of aggregated NM-HA. This further indicates that the neurotoxic effect of NM-HA amyloid is not associated with a loss-of-function, but is caused by a gain-of-function. Similarly, neurodegeneration caused by PrP^{Sc} is considered to be mainly driven by a toxic gain-of-function, as PrP KO animals age with some deficits but without severe neurological symptoms (Sigurdson *et al.*, 2019; Mercer and Harris, 2023). However, due to the various, sometimes not well understood, functions of PrP^{C}, the influence of a loss-of-function cannot be fully excluded (Mercer and Harris, 2023). In contrast, tau and α-synuclein execute specific functions in the cell and the loss of these proteins causes cellular impairments and cognitive decline in KO mouse models of tau and α-synuclein (Burré, 2015; Y. Wang and Mandelkow, 2016). Nevertheless, oligomers or amyloid inclusions exhibit profound aberrant functions, such as protein sequestration, synaptic dysfunction, or mitochondria and endoplasmic reticulum stress (Y. Wang and Mandelkow, 2016; Wong and Krainc, 2017). Consequently, it is believed that the gain-of-function of tau and α-synuclein outweighs the loss-of-function, but the particular contribution of both effects remains unclear (Goedert, 2016; Riera-Tur *et al.*, 2022). Strikingly, our data extends findings of a study in primary neurons, in which a non-functional amyloidogenic protein caused neurotoxicity (Riera-Tur *et al.*, 2022). While the authors reported an impairment of the lysosomal system as a neurotoxic driver, the mechanism of NM-HA-mediated toxicity and the involved toxic species are to be determined. Still, it is possible that intracellular amyloid formed from different proteins cause toxicity by shared mechanisms.

In fibril-challenged animals, degenerated neurons were found in the CA1 and CA3 area of the hippocampus. Comparing the neuronal loss with the NM-HA aggregate burden in these subfields, suggests that both processes are correlated. Interestingly, this resembles findings from tau transgenic mice, which developed tau deposits and selective neurodegeneration in CA1 and CA3 subfields upon inoculation of amyloid tau (Boluda *et al.*, 2015; Peeraer *et al.*, 2015). Similarly, challenging mice with α-synuclein fibrils caused neuronal loss in CA3 (Luna *et al.*, 2018; Dues *et al.*, 2023). Of note, animals in these studies were injected in the hippocampus and overlying cortex. These data indicate that pyramidal neurons in the CA1 and CA3 subarea are specifically vulnerable to intracellular aggregates. In NM-HA mice, this could be explained by the high NM-HA expression levels in these regions, leading to increased availability of NM-HA substrate. However, while α-synuclein pathology and toxicity depended on α-synuclein expression levels (Luna *et al.*, 2018), regional vulnerability to amyloid tau was independent of tau expression (Cornblath *et al.*, 2021). Rather, selective vulnerability to aggregated tau in the human brain was linked to distinct tau species and specific neuronal subtypes (Farrell *et al.*, 2022; Kawles *et al.*, 2023). For example, neurons of the DG were more vulnerable to amyloid tau of Pick's disease, while CA1 neurons degenerated upon exposure to AD-associated pathologic tau. This indicates that vulnerability is also mediated by the amyloid conformation and suggests that CA1 and CA3 neurons in NM-HA mice are specifically vulnerable to the NM F4 and F37 fibril folds. Furthermore, tau pathology in the CA1 subfield was linked to neurotoxicity in the subiculum (Farrell *et al.*, 2022). This area exhibits profound NM-HA pathology in NM-HA mice. Thus, investigating neuronal loss in other brain regions with high NM-HA amyloid burden, such as the subiculum or ventral DG, could reveal more vulnerable regions. In addition, to better resolve the temporal correlation between NM-HA deposition and neurodegeneration, animals should be analyzed at additional timepoints post injection.

6.3 The NM-HA model is similar to mouse models of tauopathies and synucleinopathies

The observed neuronal loss caused by NM-HA aggregates represents an important feature of NDDs. But how comparable is the NM-HA model to other mouse models of NDDs? Since NM-HA expression in NM-HA animals is controlled by the *prnp* promoter, NM-HA is expressed in the same cells that would normally produce PrP^C. Thus, WT mice expressing PrP^C at physiological levels inoculated with recombinant PrP^{Sc} fibrils represent a comparable disease model. After inoculating NM-HA mice with recombinant NM fibrils, animals survived

for 12 mpi without developing an explicit phenotype. In contrast, injecting recombinant PrP^{Sc} fibrils into the brain of WT mice induces prion disease with survival times ranging from 150 to 356 dpi, depending on the strain (Ma *et al.*, 2022). At the terminal stage, prion-infected animals develop neurological signs, strong PrP^{Sc} deposition, and spongiform degeneration in the brain (F. Wang *et al.*, 2010; Z. Zhang *et al.*, 2013). While the NM-HA amyloid burden was high in numerous brain regions of fibril-injected animals, neurodegeneration occurred locally without spongiosis. This indicates that neurotoxicity is not driven by the cell population expressing the aggregating protein, but depends on the aggregating protein itself. Furthermore, this highlights that PrP^{Sc} and NM-HA amyloid strongly differ in their toxicity. The disparity might be explained by the different subcellular localization of PrP^C and NM-HA. NM-HA is expressed cytosolically and aggregates intracellularly, while most PrP^C is attached to the outer cell membrane and aggregates extracellularly and/or within intracellular vesicles (Sigurdson et al., 2019). Due to the different cellular location and different pools of potential interactors, the toxicity of NM and PrP^{Sc} deposits may vary greatly (Mercer and Harris, 2023), which limits the comparability of these models. Hence, disease models of intracellular amyloid deposits, such as α-synuclein and tau, might share more similarity with the NM-HA model. In several studies, pre-formed fibrils (PFFs) of mouse or human α-synuclein were injected into the brain of WT mice. Similar to our findings in NM-HA animals, PFFs reliably induced aggregation of the homotypic protein in numerous brain regions within 1 - 3 mpi (Luk *et al.*, 2012a; Masuda-Suzukake *et al.*, 2013; Rey *et al.*, 2018; Stoyka *et al.*, 2020; Rahayel *et al.*, 2022). However, in contrast to fibril-injected NM-HA mice, neuronal loss and behavioral deficits were less frequently reported (Luk *et al.*, 2012a; Stoyka *et al.*, 2020). Of note, decreased survival times were only described in injected transgenic animals overexpressing α-synuclein, but not in WT mice (Luk *et al.*, 2012b; Lohmann *et al.*, 2019). Strikingly, even brain homogenate or brain extracts from PD and DLB patients injected into the brain of transgenic animals failed to cause disease up to 540 dpi (Prusiner *et al.*, 2015; Lau *et al.*, 2020). Only brain homogenate from MSA patients induced disease in transgenic, but not in WT mice, (Prusiner *et al.*, 2015; Peng *et al.*, 2018; Peelaerts and Baekelandt, 2023). Hence, NM fibril injection of NM-HA mice induced neurodegeneration and behavioral deficits similar to, if not even stronger than, those observed in WT animals injected with α-synuclein PFFs. In most studies of tauopathies, tau aggregation was induced in transgenic mouse lines overexpressing a certain, often mutated, tau isoform (Clavaguera *et al.*, 2009; Iba *et al.*, 2013; Boluda *et al.*, 2015; Peeraer *et al.*, 2015; Narasimhan *et al.*, 2017). But also in WT animals, the injection of recombinant tau fibrils or tau isolates from patient's brains robustly seeded tau aggregates within 3 mpi, similar to our model (J. L. Guo *et al.*, 2016; Cornblath *et al.*, 2021). Interestingly, only a few studies in transgenic PS19 and tauP301L mice reported local neuronal loss together with astrogliosis

and microgliosis after injecting tau fibrils or brain extracts. (Boluda *et al.*, 2015; Peeraer *et al.*, 2015). None of the mentioned reports described clinical symptoms or shortened survival times. Due to these limitations, tau KI mouse lines are now being established that express tau at endogenous levels. However, injection of brain-derived tau strains in these tau KI mice seeded tau pathology but failed to cause neurodegeneration (He et al., 2020). Thus, the NM-HA mouse model recapitulates crucial characteristics of human amyloidosis, such as neurodegeneration, that are partly absent in models of tauopathies and synucleinopathies. While the observed toxicity of NM-HA aggregates is more similar to the one of intracellular amyloid, the described discrepancies suggest that neurotoxicity is highly specific to the aggregating protein.

Still, various factors influence seeding and amyloid-related pathogenicity that need to be considered when comparing the above-mentioned models to the NM-HA system. First, efficient aggregate induction is dependent on the compatibility of seed and substrate. In WT mice, PFFs of mouse α-synuclein are more seeding-competent than PFFs of human α-synuclein (Luk *et al.*, 2016). Similarly, tau seeds consisting of the 3R tau isoform predominantly seed 3R tau but not 4R tau (He *et al.*, 2020). While these species barriers may be caused by differences in the amino acid sequences, post translational modifications, or the fibril conformation (Luk *et al.*, 2016; Arakhamia *et al.*, 2020), they strongly influence disease progression and impair model comparison. Second, the expression level of the soluble substrate protein varies between WT, KI, and transgenic mice. Since higher substrate expression correlates with increased aggregation and shortened disease onset in animals and humans, this limits a direct comparison (Clavaguera *et al.*, 2013; Antonarakis, 2017; Sigurdson *et al.*, 2019; Y. J. Guo *et al.*, 2022). Third, the majority of studies used inocula of different volumes, concentrations, and amyloid purity. Consequently, the amount of injected seeding entities varied substantially. As pathology development correlates with the inoculated seed quantity in proteinopathies, this further complicates data comparison (Iba *et al.*, 2013; Boluda *et al.*, 2015; J. L. Guo *et al.*, 2016; Lohmann *et al.*, 2019). Lastly, most studies sacrificed injected animals between 6 and 9 mpi or even earlier. Hence, data of long-term developments are rare, which restricts the assessment of pathology spread or behavioral deficits in NM-HA animals at 12 mpi.

6.4 NM fibril injection causes an inflammatory response in NM-HA mice

Another pathological feature of NDDs is profound neuroinflammation in the brain, mediated by microglia and astrocytes (Glass *et al.*, 2010). Strikingly, fibril-inoculated NM-HA mice

developed reactive astrogliosis in the ipsilateral hippocampal CA1 subfield and partly in the CA2/3 subregion at 12 mpi. In addition, microglia cell numbers in the CA1 area increased and microglia exhibited an activated morphology. The inflammatory response correlated with neuronal NM-HA deposits in the CA subfields, while microglia and astrocytes in areas without NM-HA aggregates remained unchanged. This resembles findings from transgenic mouse models of tau, in which the injection of pathological tau in the hippocampus caused severe micro- and astrogliosis in CA1 and CA3 subfields (Boluda *et al.*, 2015; Peeraer *et al.*, 2015). Likewise, intrahippocampal inoculation of α-synuclein PFFs into wild type animals led to α-synuclein deposits and astrogliosis in the CA3 area (Dues *et al.*, 2023), while intrastriatal inoculation caused reactive astrocytes distributed throughout the brain (Luk *et al.*, 2012b; Prusiner *et al.*, 2015; Iba *et al.*, 2022). This emphasizes that the NM-HA model not only replicates neurodegeneration, but also amyloid-associated neuroinflammation. Furthermore, in fibril-injected NM-HA animals, reactive astrogliosis was detected together with neuronal loss in the CA1 subfield, suggesting a link between astrogliosis and neurodegeneration. This connection has also been reported for tau and α-synuclein deposition (Peeraer *et al.*, 2015; Dues *et al.*, 2023) and is in line with the hypothesis that reactive astrocytes act neurotoxic and can contribute to neurodegeneration (Liddelow *et al.*, 2017; Acioglu *et al.*, 2021). Since astroglial activation is also dependent on microglia activation (Yun *et al.*, 2018), the analysis of NM-HA mice at an earlier time point post injection could give a deeper insight into the chronology and connection of NM-HA aggregation, microgliosis, astrogliosis, and neurodegeneration. In addition, other brain regions with high NM-HA aggregate burden, such as the subiculum or ventral hippocampus, should be included in the analysis. Interestingly, although microglia did not change their morphology upon the injection of monomeric NM, microglia cell numbers in the hippocampus increased compared to PBS-injected animals. This suggests that monomeric NM caused a subtle microglial response. Considering that the injection process generated seeding-competent NM species that induced aggregation in cells and animals, it is also possible that microglia responded to these NM species. Both hypotheses are supported by studies of monomeric α-synuclein that induced mild inflammatory responses in wild type animals (Iba *et al.*, 2022) and reports that discovered microglia activation mediated by tau oligomers and fibrils (Morales *et al.*, 2013). Overall, these findings highlight that the NM-HA mouse model recapitulates neuroinflammation, another essential feature of human NDDs, as well as amyloid NM-HA propagation, and neurodegeneration.

6.5 Distinct seeding capacities of F4 and F37 suggest conformational differences between fibril types

TSE strains are defined by their characteristic incubation times and neuropathological changes (Collinge and Clarke, 2007). In this project, animals challenged with F37 fibrils exhibited markedly stronger NM pathology in the brain at 1 mpi, compared to animals receiving F4 fibrils. Further, in experiments *in vitro*, F37 fibrils were fragmented into smaller seeds than F4 by sonication and were more efficient at seeding NM-HA aggregates in cells. This is in line with previous studies reporting that the length of NM seeds is inversely correlated with the prion inducing capacity in yeast (Tanaka *et al.*, 2006; Marchante *et al.*, 2017). These findings are further supported by data from NM expressing N2a cells, in which short NM fragments seeded NM aggregation more efficiently than longer ones (Michiels *et al.*, 2020). In addition, the capacity of smaller NM seeds to induce aggregation was linked to increased cellular seed uptake (Michiels *et al.*, 2020). Possibly, the smaller seeds of F37 were more easily internalized by cells and hence, induced more aggregation *in vitro* and in fibril-inoculated animals. Most importantly, the seed length of NM fibrils has been linked directly to the fibril conformation, specifically to the length of the amyloid core-forming region of NM polymers (Toyama *et al.*, 2007). NM fibrils with a shorter amyloid core region were less mechanically stable and were fragmented into shorter seeds *in vitro.* These seeds also exhibited higher seeding capacity in yeast (Tanaka *et al.*, 2006; Toyama *et al.*, 2007). This indicates that the conformation of NM strains determines their seeding potential and could explain the distinct seeding efficiencies of F4 and F37 fibrils. These findings reflect results from tau strains in cells that exhibited different seeding strengths, which were inversely correlated to the size of tau fibril species (Sanders *et al.*, 2014; Kaufman *et al.*, 2016). Furthermore, similar to the seeding behavior of F4 and F37 fibrils in cells and NM-HA mice, tau strains with weak or strong seeding capacities in cultured cells also exhibited comparable week or strong seeding activities *in vivo* (Kaufman *et al.*, 2016). This was also observed for PFF strains of α-synuclein that induced aggregation of α-synuclein with comparable activity in human iPSC-derived neurons and in mice (Peelaerts *et al.*, 2015; Gribaudo *et al.*, 2019). Together, the distinct seeding efficiencies of F4 and F37 fibrils *in cellula* and *in vivo* indicate conformational differences between the NM polymorphs.

6.6 Close conformational relationship of F4 and F37 as cause of similar dissemination routes

Despite the observed differences in seeding activities of F4 and F37 fibrils, the injection of both fibril types into NM-HA mice induced NM-HA aggregates that spread to very similar brain regions at 12 mpi. This suggests that the observed conformational differences between F4 and F37 fibrils did not induce NM prion strains that differed in their spreading behavior and brain region tropism. By contrast, strains of PrP^{Sc}, tau, and α-synuclein, when injected into the brain of WT and transgenic mice, cause seed-specific transmission patterns (Peelaerts *et al.*, 2015; J. L. Guo *et al.*, 2016; Legname and Moda, 2017; Rey *et al.*, 2019; Lau *et al.*, 2020). Likewise, pathological strains isolated from the brain of patients suffering from tauopathies or synucleinopathies, induce specific spreading patterns and pathologies in the brains of WT and transgenic mice (Clavaguera *et al.*, 2013; Sanders *et al.*, 2014; Boluda *et al.*, 2015; Prusiner *et al.*, 2015; He *et al.*, 2020; Van der Perren *et al.*, 2020; Porta *et al.*, 2021). These data support the hypothesis that the conformation of a given prion-like protein aggregate determines its dissemination and brain region tropism (Collinge and Clarke, 2007; Hoppe *et al.*, 2021). One possible explanation for our findings is that conformational differences in NM fibrils are insufficient to translate into specific strain phenotypes. Unfortunately, the exact structures of F4 and F37 fibrils remains unresolved. TEM images of F4 and F37 did not reveal explicit structural differences. Furthermore, the ThT assay showed that both fibrils might share a similar amyloid core region within amino acid residues 75-123. This region has previously been identified to form the amyloid core of NM fibrils in mammalian cells (Duernberger *et al.*, 2018). It has been shown that closely related fibril strains of tau and synuclein induce similar neuropathological patterns *in vivo* (Kaufman *et al.*, 2016; Yang *et al.*, 2022). Cryo-EM should be applied to solve the structures of F4 and F37 fibrils. Further, it is unclear if the conformation of F4 and F37 fibrils is conserved by NM-HA prions propagating in mice. While some studies claim that amyloid conformations of original tau and α-synuclein seeds are retained when propagating them *in vitro* and *in vivo* (Bousset *et al.*, 2013; Sanders *et al.*, 2014), other studies report that imprinting a conformation even under highly stable conditions *in vitro* can be challenging (J. L. Guo *et al.*, 2013; Lau *et al.*, 2020; Lövestam *et al.*, 2021). In addition, recent data suggest that the cell-specific environment, ions, post-translational modifications, or protein-membrane interactions determine the structure of amyloid polymorphs (Peng *et al.*, 2018; Lövestam *et al.*, 2022; Peelaerts and Baekelandt, 2023). Here, F4 and F37 fibrils were generated *in vitro* under standard conditions in PBS without specific cofactors. This could have created fibril polymorphs that are less compatible with the cell environment *in vivo*. It is possible that upon uptake, the same cell populations

selectively propagate a specific NM-HA conformer that is more adapted to the cellular environment and that differs from F4 and F37. This is in line with the structural adaptation of PrP^{Sc} strains to a new environment (Bistaffa *et al.*, 2019). It is hypothesized that amyloid fibril populations are not all the same, but exist in a heterogenous pool of variants. Upon introduction into a new environment, the most compatible strain, that might differ from the previously dominant strain, is selected and prevails (Baskakov, 2014). Others argue that strains can actively adapt their conformation over several passages to generate new, better adapted polymorphs. As adaptation occurs slowly, the first introduction causes a long incubation phase, similar to what we observed (Makarava and Baskakov, 2012). Although we are not able to determine if the cellular environment of NM-HA mice caused a strain selection or strain adaptation, both processes could have occurred upon fibril injection. As F4 and F37 fibrils were injected in the same cell population, the similar environment could have favored polymorphs that disseminated similarly. To further investigate if the conformation of NM fibrils influences NM-HA aggregate propagation, NM-HA animals should be challenged with fibrils of more distinct structures. Finally, to test for strain adaptation, brain homogenate from fibril-injected animals need to be serially passaged over several NM-HA mouse generations.

6.7 The F4 and F37 conformations induce similar neurotoxicity

Besides the shared spatio-temporal distribution of F4 and F37-induced aggregates, NM-HA amyloid also caused neurodegeneration in the same regions of the hippocampus. However, while both strains induced neurotoxicity in the ipsilateral CA1 area, injection of the more seeding-competent F37 strain also affected neurons in the CA3 area. This reflects findings on tau aggregates in dividing cells, in which strains with strong seeding potential were more toxic to cells (Kaufman *et al.*, 2016). Similarly, α-synuclein fibrils with strong seeding ability caused shorter incubation times in TgM83$^{+/-}$ mice (Lau *et al.*, 2020). This suggests that the aggregate conformation influences the degree of neurotoxicity. Remarkably, disease progression caused by F4 and F37 resembles observations from recombinant PrP^{Sc} strains. In contrast to highly toxic natural PrP^{Sc} strains, many recombinant PrP^{Sc} strains induced disease after long incubation times (500 - 750 dpi) only in transgenic but not in WT mice (Legname *et al.*, 2004; Colby *et al.*, 2010). Others induced PrP^{Sc} deposits in the brain of WT animals with no signs of clinical disease (Makarava *et al.*, 2010; Barron *et al.*, 2016; Ma *et al.*, 2022). This further supports the hypothesis that the toxicity of a given amyloid is to some extent enciphered in its conformation. For recombinant PrP^{Sc} it is argued that the lack of the GPI anchor and glycosylation leads to conformations that are insufficiently compatible with the host PrP and

hence, less toxic (Baskakov, 2014; Makarava *et al.*, 2018). It is thus possible that our generated NM fibrils elicit low neurotoxicity, but theoretically other NM conformers could exist that are more toxic. Additionally, conformational similarities of F4 and F37 (section 6.6) could explain the comparable toxicity observed in fibril-injected mice. Extending the incubation time beyond 12 months after F4 and F37 injection could give a deeper insight into amyloid-mediated toxicity. Further, the use of co-factors, such as RNA, heparin, or lipopolysaccharide during fibrilization has been shown to modulate pathogenicity of recombinant PrP^{Sc}, tau, and α-synuclein (Goedert *et al.*, 1996; F. Wang *et al.*, 2010; Bousset *et al.*, 2013; C. Kim *et al.*, 2016). Hence, a change in the polymerization conditions could generate NM fibrils that potentially induce a stronger pathology and disease phenotype.

6.8 NM-HA prions spread through the brain via functional connections

In human NDDs, pathological protein deposits propagate through the brain in a stereotypical and time-dependent manner (Braak and Braak, 1991). Here, NM-HA amyloid in fibril-injected mice disseminated from the hippocampus to nearby and distant brain regions in a prion-like manner within 12 months. Interestingly, the dissemination pattern was restricted to areas that are neuroanatomically connected to the hippocampus (figure 23 A). The strongest pathology was found in the ipsi- and contralateral hippocampal formation (HF). Considering that animals were injected in the DG and that hippocampal subregions are strongly interconnected, this was to be expected. The HF comprises the DG, the CA1-3 subfields, the subiculum, and the entorhinal cortex (EC) (Amaral and Witter, 1989). These subregions are, among others, connected via the trisynaptic path (figure 23 B). In short, neurons in the upper layers of the EC send projections to neurons in the granule layer of the DG. From there, fibres connect with pyramidal neurons of the CA3 region, which in turn send their axons to the CA1 area. The CA1 closes the circuit by projecting back to the lower layers of the EC (Andersen *et al.*, 1971; van Groen *et al.*, 2003). As major hippocampal output zone, the CA1 also projects to the subiculum, in which strong NM-HA pathology was detected (figure 23 A). NM-HA aggregates in the contralateral HF likely disseminated via axons of the ipsilateral CA3 subfield connecting with contralateral CA3 and CA1 pyramidal neurons (Amaral *et al.*, 1991; Wyss and Van Groen, 1992). While one must consider that a portion of the inoculum might have distributed via diffusion around the injection site, the observed pathology in subiculum, EC and contralateral HF strongly argues for a directed dissemination. NM-HA deposits in the cortical regions could have traveled to the retrosplenial cortex via bidirectional projections from CA1 and subiculum (RSP) (Cenquizca and Swanson, 2007). Additionally, the medial prefrontal cortex (mPFC) is
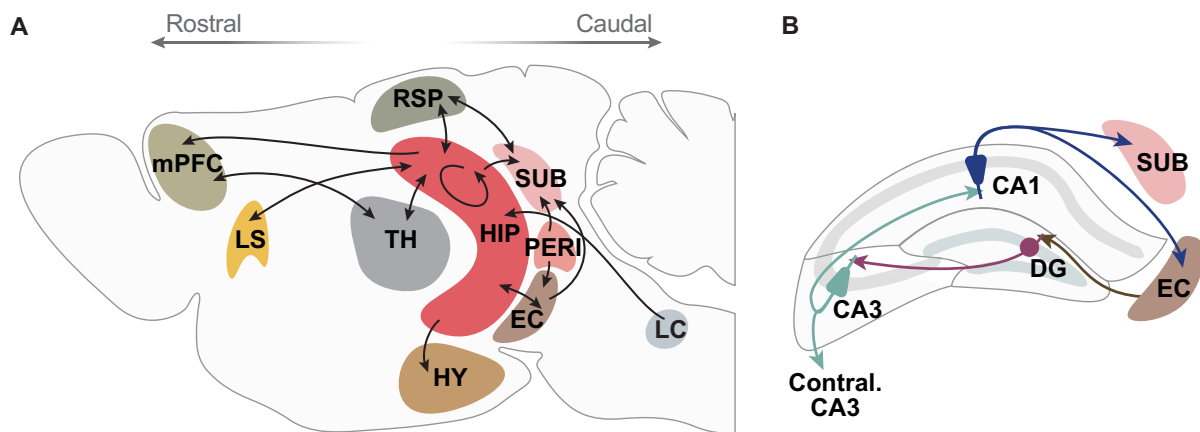
Figure 23. Map of brain regions with NM-HA pathology and their connection to and within the hippocampus. **A** Randomly colored shapes outline brain areas in which NM-HA amyloid were detected. Arrows indicate mono- or bidirectional projections from and/or to brain regions. For simplicity, only the main connections are shown. Hippocampal-connected regions without pathology are not shown. **B** Illustration of the trisynaptic path connecting the entorhinal cortex (EC) with the dentate gyrus (DG), cornu ammonis (CA) region 3 and 1, and the subiculum. Contral.: contralateral, HIP: hippocampus HY: hypothalamus, LC: locus coeruleus, LS: lateral septal nucleus, mPFC: medial prefrontal cortex, PERI: perirhinal area, RSP: retrosplenial cortex, SUB: subiculum, TH: thalamus.

linked to the CA1 subfield and subiculum via unidirectional projections allowing NM-HA amyloid dissemination (Jay and Witter, 1991; Thierry *et al.*, 2000). NM-HA pathology in the thalamus could be due to connections to and from the hippocampus or the mPFC (Aggleton and Brown, 1999; Varela *et al.*, 2014). The CA1 and subiculum also form circuits to the medial septum via the fimbria (Risold and Swanson, 1996) and strongly project to numerous nuclei of the hypothalamus, in which NM-HA deposits were detected (Cenquizca and Swanson, 2006). Finally, the HF receives unidirectional projections from the locus coeruleus, which was the most caudal area containing NM-HA deposits (Jones and Moore, 1977). Since the connections between the described areas are a lot more diverse and complex, the direction of NM-HA amyloid dissemination - anterogradly, retrogradly, or trans-synaptically - remains speculative. NM-HA pathology in the locus coeruleus argues for retrograde dissemination, due to the strict unidirectional connection from the locus coeruleus to the hippocampus. The same holds true for amyloid found in the hypothalamic nuclei and upper layers of the enthorinal cortex. In contrast, the intense pathology in the subiculum, which receives the strongest input from the CA1 subfield, indicates anterograde spread. In addition, the affected RSP, mPFC and the anteroventral nucleus of thalamus are mainly reached by connections from the hippocampus, supporting anterograde distribution. Finally, a few hippocampal-connected regions, such as the amygdala, ventral tegmental area or the nucleus accumbens that are targets of amyloid α-synuclein (Masuda-Suzukake *et al.*, 2013; Rahayel *et al.*, 2022) remained free of NM-HA deposits. This suggests that these areas are either less vulnerable to NM-HA amyloid, or are reached at later stages. Overall, we conclude that induced NM-HA prions spread from the hippocampus to neuroanatomically connected brain regions.

6.9 NM and other amyloidogenic proteins share dissemination routes

Strikingly, the dissemination behavior of NM-HA prions closely reflects the spreading of human disease-related amyloid in animal models of NDDs. Various groups reported that the injection of recombinant tau fibrils or AD patient-derived tau into the hippocampus of transgenic and WT mice induced pathological tau inclusions in brain regions anatomically connected to the hippocampus (Clavaguera *et al.*, 2009; Clavaguera *et al.*, 2013; Iba *et al.*, 2013; Sanders *et al.*, 2014; J. L. Guo *et al.*, 2016). In line with our results, tau pathology was detected in the above-mentioned brain regions in a time-dependent manner. The authors concluded that the propagation of intracellular amyloid occurs trans-neuronally in anterograde and retrograde direction. Similar results were obtained in studies investigating the spread of α-synuclein, TDP-43, and PrP^{Sc} deposits in the mouse brain, even though different inoculation sites were used (Luk *et al.*, 2012a; Rey *et al.*, 2013; Rangel *et al.*, 2014; Porta *et al.*, 2018; S. Kim *et al.*, 2019). Recently, computational modeling of pathological tau and α-synuclein dissemination in the brain of WT mice supported these findings (Mezias *et al.*, 2020; Cornblath *et al.*, 2021; Ramirez *et al.*, 2023). Interestingly, the spatiotemporal distribution of tau and α-synuclein pathology was best described by combining interneuronal and bidirectional transmission, with a favor for retrograde transport. Also in humans, the dissemination of tau pathology via the neuronal connectome was confirmed *in vivo* in AD patients (Franzmeier *et al.*, 2020). Here, tau accumulation was found in highly inter-connected brain regions.

However, increasing evidence also suggests an active role of astrocytes in the dissemination of PrP^{Sc}, amyloid tau, and α-synuclein (Reid *et al.*, 2020; Acioglu *et al.*, 2021; Tahir *et al.*, 2022). Intriguingly, astrocytes in fibril-injected NM-HA animals contained NM-HA deposits. As the *prnp* promoter is active in astrocytes (Y. Zhang *et al.*, 2014), astroglia in NM-HA animals express NM-HA and thus astroglial NM-HA can be seeded upon uptake of NM-HA amyloid. It is believed that astrocytes internalize pathological proteins from the synaptic cleft for degradation. In NDDs, however, impaired astrocytic degradation may lead to amyloid accumulation within the astrocytes and the propagation of infectious seeds to surrounding neurons (Smethurst *et al.*, 2022). Hence, astrocytic NM-HA aggregates suggest impaired clearance, which could contribute to the dissemination of NM-HA deposits. Together, the NM-HA model recapitulates interneuronal spreading of pathological NM-HA but may also capture dissemination mediated by astroglia. This emphasizes that NM prions behave very similarly to disease-related amyloid and further implicates that intracellular amyloid propagation is based on shared mechanisms.

6.10 Limitations of the study

The biggest risk factor for developing NDDs, such as AD and PD, is aging (Wyss-Coray, 2016). During aging, various cellular and molecular mechanisms are disturbed, including protein homeostasis, which has been associated with the deposition of misfolded proteins (Hipp *et al.*, 2019; Hou *et al.*, 2019). In this project, animals were challenged with fibrils at an early adult stage and were sacrificed when they reached mid-age (14 months). This corresponds to a human age of approx. 20 years at inoculation and approx. 40 years at the endpoint (Flurkey *et al.*, 2007). Hence, the current NM-HA study design recapitulated rather early stages of amyloidosis, but the influence of aging on NM-HA pathology induction and disease progression was only insufficiently captured. This is similar to most mouse models of NDDs, as disease is either induced early in life or develops within a short time due to protein overexpression (Clavaguera *et al.*, 2013; Prusiner *et al.*, 2015). Studies focusing on aging investigated tau and α-synuclein aggregation in aged mice and reported exacerbated pathology and inflammation caused by α-synuclein deposits (Iba *et al.*, 2022) and altered spreading of tau pathology (J. L. Guo *et al.*, 2016; Nies *et al.*, 2021). Thus, it would be of great interest to investigate the influence of aging in the NM-HA model by injecting NM fibrils into aged NM-HA animals. This approach could reveal age-dependent mechanisms of amyloid-mediated pathology shared by different NDDs.

Another limitation may be the unilateral injection of fibrils in NM-HA animals. While this approach was essential to follow the dissemination of NM-HA deposits ipsi- and contralaterally, it likely limited the development of cognitive and clinical signs. As the contralateral hippocampus remained mostly unaffected over the course of 12 months, it could explain the observed mild cognitive decline. This is in line with other studies on tau and α-synuclein, in which fibrils were unilaterally injected but mice showed no behavioral deficits (Luk *et al.*, 2012a; J. L. Guo *et al.*, 2016). However, in the human brain, amyloid pathology presents mostly bilaterally (Braak and Braak, 1995; Schöll *et al.*, 2016). Hence, human NDDs could be even more closely recapitulated if NM fibrils were injected into both hemispheres potentially leading to increased pathology and neurodegeneration (Dues *et al.*, 2023).

Finally, one could argue that the PrP KO in NM-HA mice itself leads to a functional deficit. However, we did not observe severe phenotypic changes in NM-HA animals at 24 months (data not shown). Furthermore, although PrP has been hypothesized to protect against inflammation (Bakkebø *et al.*, 2015), NM-HA animals did not show increased inflammation in the brain at 18 months. Consequently, we conclude that the PrP KO has no or only very little influence on cell populations in the brain of NM-HA animals.

6.11 Relevance

NDDs, such as AD and PD, are a major burden in our aging population. Currently, patients are mainly treated symptomatically and have no prospect of being cured (Marasco, 2020). While this urges the need for disease-modifying drugs, many processes contributing to disease development and neuronal loss remain insufficiently understood (Wilson *et al.*, 2023). Here, we demonstrated that the aggregation of the non-mammalian and non-disease-related amyloidogenic yeast prion domain Sup35 NM replicates key aspects of NDDs *in vivo*. Fibril-seeded intracellular NM-HA aggregates disseminate through the brain via the neuronal connectome and induce neuroinflammation and neurodegeneration. Thus, NM-HA aggregates behave similarly to human disease-associated amyloid composed of tau or α-synuclein. Our data suggest that the gain-of-function of protein aggregates plays a crucial role in neurotoxicity and neurodegeneration. Most importantly, our findings indicate that mechanisms of intracellular amyloid fragmentation, propagation, and neurotoxicity are shared between different amyloidogenic proteins. Consequently, interactors of NM-HA amyloid could potentially also regulate other amyloidogenic proteins. One example is VCP, which could be involved in the disaggregation of NM-HA and tau aggregates. Thus, the NM-HA mouse model provides proof of concept of disease-related mechanisms and could help to identify pathways for therapeutic intervention. Interestingly, aggregated Sup35 has recently been described to induce α-synuclein aggregation in transgenic and WT mice, suggesting that yeast infection might contribute to PD pathology (Meng *et al.*, 2023). In our hands, NM fibrils failed to seed α-synuclein in NM-HA mice and in cells (preliminary data, not shown). Yet, it suggests that cross-seeding of amyloidogenic proteins can accelerate disease progression in NDDs (Bassil *et al.*, 2020), which is another important aspect that could be investigated in more detail in the future. In addition, the NM-HA mouse model could be valuable for drug discovery. Since disease pathogenesis in NM-HA mice progresses slowly over several months after fibril injection, the model offers a large therapeutic window for testing drugs that interfere with the disease at an early stage. For example, the NM-HA mouse model could be used for long-term studies of drugs that can only be applied in low doses because of their toxicity. It may be advantageous that neurons show a certain resilience to NM-HA aggregates, as this may increase the responsiveness to the tested drugs. NM-HA mice may therefore be a suitable model for pharmacological interventions.

Acknowledgements

First and foremost, I would like to thank my supervisor, Prof. Dr. Ina Vorberg. She not only gave me the opportunity to do my PhD in her lab, but also guided me very well through this time. Thank you for your great scientific and emotional support and your always open door for short questions, long discussions, or simply a nice chat! I really appreciated our positive and trusting relationship and that you pushed my self-esteem when I needed it!

Furthermore, I would like to thank Prof. Dr. Jörg Höhfeld for agreeing to be the second examiner of my PhD thesis. Likewise, I want to thank Prof. Dr. Walter Witke and Frau Jun-Prof. Dr. Marie-Christine Simon for taking the time and joining my examination committee.

A big and heartfelt thank you to all current and former members of the AG Vorberg group who have supported me along the way! I would especially like to thank my lab buddy Alina for the great time we spent together in the lab, with lots of laughing about calculations, support in down-times and many evenings together in Endenich! I would also like to thank my HiWi Joana for her great help and positive attitude, André and Lydia, for patiently answering my questions and of course Carmen, for being the best administrative support in the world! Finally, thank you to the DZNE DRs for the many relaxing coffee breaks and fun after-work events: Steffi, Nina, Eva, Tanja, Angela, Komal, Sally, Lilly, Thorben, and Kai.

In addition, I would like to thank everyone who helped me with my animal experiments: the DZNE animal research facility, especially Ben Wagner, Kristin Oberländer for sharing her immense knowledge of behavioral experiments, and Sinead O'Sullivan for showing me the surgery. I would also like to thank the LMF and LAT facilities, especially Ireen König, Hans Fried, and Philip Denner, for helping me with my experiments. Thanks also to Ayse Ulusoy and Donato Di Monte for their great scientific support and contribution to my TAC meetings. Furthermore, I would like to thank our collaborators Emiel Michiels, for performing the TEM analysis of our NM fibrils, as well as Yury Chernoff and Konstantin Kulichikhin for sharing their NM expertise with us.

I would like to deeply thank my family and friends for their constant encouragement and support, especially my parents and my father, who inspired me to become a neuroscientist! Finally, a very special thank you to Max who has been my constant source of motivation, reassurance and encouragement - thank you for being by my side!

Bibliography

Abounit, S., Bousset, L., Loria, F., Zhu, S., de Chaumont, F., Pieri, L., . . . Zurzolo, C. (2016). Tunneling nanotubes spread fibrillar α-synuclein by intercellular trafficking of lysosomes. *Embo j, 35*(19), 2120-2138. doi:10.15252/embj.201593411

Acioglu, C., Li, L., & Elkabes, S. (2021). Contribution of astrocytes to neuropathology of neurodegenerative diseases. *Brain Res, 1758*, 147291. doi:10.1016/j.brainres.2021.147291

Aggleton, J. P., & Brown, M. W. (1999). Episodic memory, amnesia, and the hippocampal-anterior thalamic axis. *Behav Brain Sci, 22*(3), 425-444; discussion 444-489.

Aguzzi, A., & Calella, A. M. (2009). Prions: protein aggregation and infectious diseases. *Physiol Rev, 89*(4), 1105-1152. doi:10.1152/physrev.00006.2009

Allen, K. D., Wegrzyn, R. D., Chernova, T. A., Müller, S., Newnam, G. P., Winslett, P. A., . . . Chernoff, Y. O. (2005). Hsp70 chaperones as modulators of prion life cycle: novel effects of Ssa and Ssb on the Saccharomyces cerevisiae prion [PSI+]. *Genetics, 169*(3), 1227-1242. doi:10.1534/genetics.104.037168

Alonso Adel, C., Li, B., Grundke-Iqbal, I., & Iqbal, K. (2006). Polymerization of hyperphosphorylated tau into filaments eliminates its inhibitory activity. *Proc Natl Acad Sci U S A, 103*(23), 8864-8869. doi:10.1073/pnas.0603214103

Amaral, D. G., Dolorfo, C., & Alvarez-Royo, P. (1991). Organization of CA1 projections to the subiculum: a PHA-L analysis in the rat. *Hippocampus, 1*(4), 415-435. doi:10.1002/hipo.450010410

Amaral, D. G., & Witter, M. P. (1989). The three-dimensional organization of the hippocampal formation: a review of anatomical data. *Neuroscience, 31*(3), 571-591. doi:10.1016/0306-4522(89)90424-7

An, L., & Harrison, P. M. (2016). The evolutionary scope and neurological disease linkage of yeast-prion-like proteins in humans. *Biology Direct, 11*(1), 32. doi:10.1186/s13062-016-0134-5

Andersen, P., Bliss, T. V., & Skrede, K. K. (1971). Lamellar organization of hippocampal pathways. *Exp Brain Res, 13*(2), 222-238. doi:10.1007/bf00234087

Antonarakis, S. E. (2017). Down syndrome and the complexity of genome dosage imbalance. *Nat Rev Genet, 18*(3), 147-163. doi:10.1038/nrg.2016.154

Arakhamia, T., Lee, C. E., Carlomagno, Y., Duong, D. M., Kundinger, S. R., Wang, K., . . . Fitzpatrick, A. W. P. (2020). Posttranslational Modifications Mediate the Structural Diversity of Tauopathy Strains. *Cell, 180*(4), 633-644.e612. doi:10.1016/j.cell.2020.01.027

Bakkebø, M. K., Mouillet-Richard, S., Espenes, A., Goldmann, W., Tatzelt, J., & Tranulis, M. A. (2015). The Cellular Prion Protein: A Player in Immunological Quiescence. *Front Immunol, 6*, 450. doi:10.3389/fimmu.2015.00450

Balch, W. E., Morimoto, R. I., Dillin, A., & Kelly, J. W. (2008). Adapting proteostasis for disease intervention. *Science, 319*(5865), 916-919. doi:10.1126/science.1141448

Ballatore, C., Lee, V. M. Y., & Trojanowski, J. Q. (2007). Tau-mediated neurodegeneration in Alzheimer's disease and related disorders. *Nature Reviews Neuroscience, 8*(9), 663-672. doi:10.1038/nrn2194

Bamberger, M. E., Harris, M. E., McDonald, D. R., Husemann, J., & Landreth, G. E. (2003). A cell surface receptor complex for fibrillar beta-amyloid mediates microglial activation. *J Neurosci, 23*(7), 2665-2674. doi:10.1523/jneurosci.23-07-02665.2003

Barron, R. M., King, D., Jeffrey, M., McGovern, G., Agarwal, S., Gill, A. C., & Piccardo, P. (2016). PrP aggregation can be seeded by pre-formed recombinant PrP amyloid fibrils without the replication of infectious prions. *Acta Neuropathol, 132*(4), 611-624. doi:10.1007/s00401-016-1594-5

Baskakov, I. V. (2014). The many shades of prion strain adaptation. *Prion, 8*(2), 169-172. doi:10.4161/pri.27836

Bassil, F., Brown, H. J., Pattabhiraman, S., Iwasyk, J. E., Maghames, C. M., Meymand, E. S., . . . Lee, V. M. (2020). Amyloid-Beta (Aβ) Plaques Promote Seeding and Spreading of Alpha-Synuclein and Tau in a Mouse Model of Lewy Body Disorders with Aβ Pathology. *Neuron, 105*(2), 260-275.e266. doi:10.1016/j.neuron.2019.10.010

Batra, S., Vaquer-Alicea, J., 3rd, Manon, V. A., Kashmer, O. M., Lemoff, A., Cairns, N. J., . . . Diamond, M. I. (2023). VCP increases or decreases tau seeding using specific cofactors. *bioRxiv*. doi:10.1101/2023.08.30.555637

Bessen, R. A., & Marsh, R. F. (1992a). Biochemical and physical properties of the prion protein from two strains of the transmissible mink encephalopathy agent. *J Virol, 66*(4), 2096-2101. doi:10.1128/jvi.66.4.2096-2101.1992

Bessen, R. A., & Marsh, R. F. (1992b). Identification of two biologically distinct strains of transmissible mink encephalopathy in hamsters. *J Gen Virol, 73 (Pt 2)*, 329-334. doi:10.1099/0022-1317-73-2-329

Bistaffa, E., Moda, F., Virgilio, T., Campagnani, I., De Luca, C. M. G., Rossi, M., . . . Legname, G. (2019). Synthetic Prion Selection and Adaptation. *Mol Neurobiol, 56*(4), 2978-2989. doi:10.1007/s12035-018-1279-2

Bolós, M., Llorens-Martín, M., Jurado-Arjona, J., Hernández, F., Rábano, A., & Avila, J. (2016). Direct Evidence of Internalization of Tau by Microglia In Vitro and In Vivo. *J Alzheimers Dis, 50*(1), 77-87. doi:10.3233/jad-150704

Bolton, D. C., McKinley, M. P., & Prusiner, S. B. (1982). Identification of a protein that purifies with the scrapie prion. *Science, 218*(4579), 1309-1311. doi:10.1126/science.6815801

Boluda, S., Iba, M., Zhang, B., Raible, K. M., Lee, V. M., & Trojanowski, J. Q. (2015). Differential induction and spread of tau pathology in young PS19 tau transgenic mice following intracerebral injections of pathological tau from Alzheimer's disease or corticobasal degeneration brains. *Acta Neuropathol, 129*(2), 221-237. doi:10.1007/s00401-014-1373-0

Bousset, L., Pieri, L., Ruiz-Arlandis, G., Gath, J., Jensen, P. H., Habenstein, B., . . . Melki, R. (2013). Structural and functional characterization of two alpha-synuclein strains. *Nat Commun, 4*, 2575. doi:10.1038/ncomms3575

Braak, H., & Braak, E. (1991). Neuropathological stageing of Alzheimer-related changes. *Acta Neuropathol, 82*(4), 239-259. doi:10.1007/bf00308809

Braak, H., & Braak, E. (1995). Staging of Alzheimer's disease-related neurofibrillary changes. *Neurobiol Aging, 16*(3), 271-278; discussion 278-284. doi:10.1016/0197-4580(95)00021-6

Braak, H., Del Tredici, K., Rüb, U., de Vos, R. A., Jansen Steur, E. N., & Braak, E. (2003). Staging of brain pathology related to sporadic Parkinson's disease. *Neurobiol Aging, 24*(2), 197-211. doi:10.1016/s0197-4580(02)00065-9

Brunden, K. R., Trojanowski, J. Q., & Lee, V. M. (2008). Evidence that non-fibrillar tau causes pathology linked to neurodegeneration and behavioral impairments. *J Alzheimers Dis, 14*(4), 393-399. doi:10.3233/jad-2008-14406

Burré, J. (2015). The Synaptic Function of α-Synuclein. *J Parkinsons Dis, 5*(4), 699-713. doi:10.3233/jpd-150642

Carroll, J. A., & Chesebro, B. (2019). Neuroinflammation, Microglia, and Cell-Association during Prion Disease. *Viruses, 11*(1). doi:10.3390/v11010065

Cascella, R., Bigi, A., Cremades, N., & Cecchi, C. (2022). Effects of oligomer toxicity, fibril toxicity and fibril spreading in synucleinopathies. *Cell Mol Life Sci, 79*(3), 174. doi:10.1007/s00018-022-04166-9

Caughey, B., Baron, G. S., Chesebro, B., & Jeffrey, M. (2009). Getting a grip on prions: oligomers, amyloids, and pathological membrane interactions. *Annu Rev Biochem, 78*, 177-204. doi:10.1146/annurev.biochem.78.082907.145410

Caughey, B., Kocisko, D. A., Raymond, G. J., & Lansbury, P. T., Jr. (1995). Aggregates of scrapie-associated prion protein induce the cell-free conversion of protease-sensitive prion protein to the protease-resistant state. *Chem Biol, 2*(12), 807-817. doi:10.1016/1074-5521(95)90087-x

Caughey, B., & Peter T. Lansbury, J. (2003). PROTOFIBRILS, PORES, FIBRILS, AND NEURODEGENERATION: Separating the Responsible Protein Aggregates from The Innocent Bystanders. *Annual Review of Neuroscience, 26*(1), 267-298. doi:10.1146/annurev.neuro.26.010302.081142

Cenquizca, L. A., & Swanson, L. W. (2006). Analysis of direct hippocampal cortical field CA1 axonal projections to diencephalon in the rat. *J Comp Neurol, 497*(1), 101-114. doi:10.1002/cne.20985

Cenquizca, L. A., & Swanson, L. W. (2007). Spatial organization of direct hippocampal field CA1 axonal projections to the rest of the cerebral cortex. *Brain Res Rev, 56*(1), 1-26. doi:10.1016/j.brainresrev.2007.05.002

Chazot, G., Broussolle, E., Lapras, C., Blättler, T., Aguzzi, A., & Kopp, N. (1996). New variant of Creutzfeldt-Jakob disease in a 26-year-old French man. *Lancet, 347*(9009), 1181. doi:10.1016/s0140-6736(96)90638-8

Chen, B., Retzlaff, M., Roos, T., & Frydman, J. (2011). Cellular strategies of protein quality control. *Cold Spring Harb Perspect Biol, 3*(8), a004374. doi:10.1101/cshperspect.a004374

Chernoff, Y. O., Derkach, I. L., & Inge-Vechtomov, S. G. (1993). Multicopy SUP35 gene induces de-novo appearance of psi-like factors in the yeast Saccharomyces cerevisiae. *Curr Genet, 24*(3), 268-270. doi:10.1007/bf00351802

Chernoff, Y. O., Lindquist, S. L., Ono, B., Inge-Vechtomov, S. G., & Liebman, S. W. (1995). Role of the chaperone protein Hsp104 in propagation of the yeast prion-like factor [psi+]. *Science, 268*(5212), 880-884. doi:10.1126/science.7754373

Chien, P., DePace, A. H., Collins, S. R., & Weissman, J. S. (2003). Generation of prion transmission barriers by mutational control of amyloid conformations. *Nature, 424*(6951), 948-951. doi:10.1038/nature01894

Chiti, F., & Dobson, C. M. (2006). Protein misfolding, functional amyloid, and human disease. *Annu Rev Biochem, 75*, 333-366. doi:10.1146/annurev.biochem.75.101304.123901

Ciechanover, A. (2006). Intracellular protein degradation: from a vague idea thru the lysosome and the ubiquitin-proteasome system and onto human diseases and drug targeting. *Exp Biol Med (Maywood), 231*(7), 1197-1211. doi:10.1177/153537020623100705

Clavaguera, F., Akatsu, H., Fraser, G., Crowther, R. A., Frank, S., Hench, J., . . . Tolnay, M. (2013). Brain homogenates from human tauopathies induce tau inclusions in mouse brain. *Proc Natl Acad Sci U S A, 110*(23), 9535-9540. doi:10.1073/pnas.1301175110

Clavaguera, F., Bolmont, T., Crowther, R. A., Abramowski, D., Frank, S., Probst, A., . . . Tolnay, M. (2009). Transmission and spreading of tauopathy in transgenic mouse brain. *Nat Cell Biol, 11*(7), 909-913. doi:10.1038/ncb1901

Colby, D. W., Wain, R., Baskakov, I. V., Legname, G., Palmer, C. G., Nguyen, H. O., . . . Prusiner, S. B. (2010). Protease-sensitive synthetic prions. *PLoS Pathog, 6*(1), e1000736. doi:10.1371/journal.ppat.1000736

Cole, G. M., & Timiras, P. S. (1987). Ubiquitin-protein conjugates in Alzheimer's lesions. *Neurosci Lett, 79*(1-2), 207-212. doi:10.1016/0304-3940(87)90698-7

Collinge, J. (2001). Prion diseases of humans and animals: their causes and molecular basis. *Annu Rev Neurosci, 24*, 519-550. doi:10.1146/annurev.neuro.24.1.519

Collinge, J., & Clarke, A. R. (2007). A general model of prion strains and their pathogenicity. *Science, 318*(5852), 930-936. doi:10.1126/science.1138718

Collinge, J., Sidle, K. C., Meads, J., Ironside, J., & Hill, A. F. (1996). Molecular analysis of prion strain variation and the aetiology of 'new variant' CJD. *Nature, 383*(6602), 685-690. doi:10.1038/383685a0

Cornblath, E. J., Li, H. L., Changolkar, L., Zhang, B., Brown, H. J., Gathagan, R. J., . . . Henderson, M. X. (2021). Computational modeling of tau pathology spread reveals patterns of regional vulnerability and the impact of a genetic risk factor. *Sci Adv, 7*(24). doi:10.1126/sciadv.abg6677

Cowan, C. M., Bossing, T., Page, A., Shepherd, D., & Mudher, A. (2010). Soluble hyper-phosphorylated tau causes microtubule breakdown and functionally compromises normal tau in vivo. *Acta Neuropathol, 120*(5), 593-604. doi:10.1007/s00401-010-0716-8

Cox, B. S. (1965). Ψ, A cytoplasmic suppressor of super-suppressor in yeast. *Heredity, 20*(4), 505-521. doi:10.1038/hdy.1965.65

Crowther, R. A., & Goedert, M. (2000). Abnormal tau-containing filaments in neurodegenerative diseases. *J Struct Biol, 130*(2-3), 271-279. doi:10.1006/jsbi.2000.4270

Dalstra, H. J., Swart, K., Debets, A. J., Saupe, S. J., & Hoekstra, R. F. (2003). Sexual transmission of the [Het-S] prion leads to meiotic drive in Podospora anserina. *Proc Natl Acad Sci U S A, 100*(11), 6616-6621. doi:10.1073/pnas.1030058100

Danzer, K. M., Kranich, L. R., Ruf, W. P., Cagsal-Getkin, O., Winslow, A. R., Zhu, L., . . . McLean, P. J. (2012). Exosomal cell-to-cell transmission of alpha synuclein oligomers. *Mol Neurodegener, 7*, 42. doi:10.1186/1750-1326-7-42

Darwich, N. F., Phan, J. M., Kim, B., Suh, E., Papatriantafyllou, J. D., Changolkar, L., . . . Lee, E. B. (2020). Autosomal dominant VCP hypomorph mutation impairs disaggregation of PHF-tau. *Science, 370*(6519). doi:10.1126/science.aay8826

Das, P., & Dudley, J. P. (2021). How Viruses Use the VCP/p97 ATPase Molecular Machine. *Viruses, 13*(9). doi:10.3390/v13091881

Dawson, T. M., Golde, T. E., & Lagier-Tourenne, C. (2018). Animal models of neurodegenerative diseases. *Nat Neurosci, 21*(10), 1370-1379. doi:10.1038/s41593-018-0236-8

Deacon, R. M. J. (2006). Assessing nest building in mice. *Nature Protocols, 1*(3), 1117-1119. doi:10.1038/nprot.2006.170

DePace, A. H., Santoso, A., Hillner, P., & Weissman, J. S. (1998). A critical role for amino-terminal glutamine/asparagine repeats in the formation and propagation of a yeast prion. *Cell, 93*(7), 1241-1252. doi:10.1016/s0092-8674(00)81467-1

Deriziotis, P., André, R., Smith, D. M., Goold, R., Kinghorn, K. J., Kristiansen, M., . . . Tabrizi, S. J. (2011). Misfolded PrP impairs the UPS by interaction with the 20S proteasome and inhibition of substrate entry. *Embo j, 30*(15), 3065-3077. doi:10.1038/emboj.2011.224

Derkatch, I. L., Bradley, M. E., Zhou, P., Chernoff, Y. O., & Liebman, S. W. (1997). Genetic and environmental factors affecting the de novo appearance of the [PSI+] prion in Saccharomyces cerevisiae. *Genetics, 147*(2), 507-519. doi:10.1093/genetics/147.2.507

Derkatch, I. L., Chernoff, Y. O., Kushnirov, V. V., Inge-Vechtomov, S. G., & Liebman, S. W. (1996). Genesis and variability of [PSI] prion factors in Saccharomyces cerevisiae. *Genetics, 144*(4), 1375-1386. doi:10.1093/genetics/144.4.1375

Desplats, P., Lee, H. J., Bae, E. J., Patrick, C., Rockenstein, E., Crews, L., . . . Lee, S. J. (2009). Inclusion formation and neuronal cell death through neuron-to-neuron transmission of alpha-synuclein. *Proc Natl Acad Sci U S A, 106*(31), 13010-13015. doi:10.1073/pnas.0903691106

DeTure, M. A., & Dickson, D. W. (2019). The neuropathological diagnosis of Alzheimer's disease. *Mol Neurodegener, 14*(1), 32. doi:10.1186/s13024-019-0333-5

DiFiglia, M., Sapp, E., Chase, K. O., Davies, S. W., Bates, G. P., Vonsattel, J. P., & Aronin, N. (1997). Aggregation of huntingtin in neuronal intranuclear inclusions and dystrophic neurites in brain. *Science, 277*(5334), 1990-1993. doi:10.1126/science.277.5334.1990

Dikic, I. (2017). Proteasomal and Autophagic Degradation Systems. *Annual Review of Biochemistry, 86*(1), 193-224. doi:10.1146/annurev-biochem-061516-044908

Douglas, P. M., & Dillin, A. (2010). Protein homeostasis and aging in neurodegeneration. *J Cell Biol, 190*(5), 719-729. doi:10.1083/jcb.201005144

Du, Z., Park, K. W., Yu, H., Fan, Q., & Li, L. (2008). Newly identified prion linked to the chromatin-remodeling factor Swi1 in Saccharomyces cerevisiae. *Nat Genet, 40*(4), 460-465. doi:10.1038/ng.112

Duernberger, Y., Liu, S., Riemschoss, K., Paulsen, L., Bester, R., Kuhn, P. H., . . . Vorberg, I. (2018). Prion Replication in the Mammalian Cytosol: Functional Regions within a Prion Domain Driving Induction, Propagation, and Inheritance. *Mol Cell Biol, 38*(15). doi:10.1128/mcb.00111-18

Dues, D. J., Nguyen, A. P. T., Becker, K., Ma, J., & Moore, D. J. (2023). Hippocampal subfield vulnerability to α-synuclein pathology precedes neurodegeneration and cognitive dysfunction. *bioRxiv*. doi:10.1101/2023.04.12.536572

Eanes, E. D., & Glenner, G. G. (1968). X-ray diffraction studies on amyloid filaments. *J Histochem Cytochem, 16*(11), 673-677. doi:10.1177/16.11.673

Eisenberg, D., & Jucker, M. (2012). The amyloid state of proteins in human diseases. *Cell, 148*(6), 1188-1203. doi:10.1016/j.cell.2012.02.022

Falcon, B., Zhang, W., Murzin, A. G., Murshudov, G., Garringer, H. J., Vidal, R., . . . Goedert, M. (2018). Structures of filaments from Pick's disease reveal a novel tau protein fold. *Nature, 561*(7721), 137-140. doi:10.1038/s41586-018-0454-y

Falcon, B., Zivanov, J., Zhang, W., Murzin, A. G., Garringer, H. J., Vidal, R., . . . Scheres, S. H. W. (2019). Novel tau filament fold in chronic traumatic encephalopathy encloses hydrophobic molecules. *Nature, 568*(7752), 420-423. doi:10.1038/s41586-019-1026-5

Fang, Y.-S., Tsai, K.-J., Chang, Y.-J., Kao, P., Woods, R., Kuo, P.-H., . . . Chen, Y.-R. (2014). Full-length TDP-43 forms toxic amyloid oligomers that are present in frontotemporal lobar dementia-TDP patients. *Nature Communications, 5*(1), 4824. doi:10.1038/ncomms5824

Farrell, K., Iida, M. A., Cherry, J. D., Casella, A., Stein, T. D., Bieniek, K. F., . . . Crary, J. F. (2022). Differential Vulnerability of Hippocampal Subfields in Primary Age-Related Tauopathy and Chronic Traumatic Encephalopathy. *J Neuropathol Exp Neurol, 81*(10), 781-789. doi:10.1093/jnen/nlac066

Feinstein, S. C., & Wilson, L. (2005). Inability of tau to properly regulate neuronal microtubule dynamics: a loss-of-function mechanism by which tau might mediate neuronal cell death. *Biochim Biophys Acta, 1739*(2-3), 268-279. doi:10.1016/j.bbadis.2004.07.002

Fitzpatrick, A. W. P., Falcon, B., He, S., Murzin, A. G., Murshudov, G., Garringer, H. J., . . . Scheres, S. H. W. (2017). Cryo-EM structures of tau filaments from Alzheimer's disease. *Nature, 547*(7662), 185-190. doi:10.1038/nature23002

Flavin, W. P., Bousset, L., Green, Z. C., Chu, Y., Skarpathiotis, S., Chaney, M. J., . . . Campbell, E. M. (2017). Endocytic vesicle rupture is a conserved mechanism of cellular invasion by amyloid proteins. *Acta Neuropathol, 134*(4), 629-653. doi:10.1007/s00401-017-1722-x

Flurkey, K., M. Currer, J., & Harrison, D. E. (2007). Chapter 20 - Mouse Models in Aging Research. In J. G. Fox, M. T. Davisson, F. W. Quimby, S. W. Barthold, C. E. Newcomer, & A. L. Smith (Eds.), *The Mouse in Biomedical Research (Second Edition)* (pp. 637-672). Burlington: Academic Press.

Franzmeier, N., Neitzel, J., Rubinski, A., Smith, R., Strandberg, O., Ossenkoppele, R., . . . Ewers, M. (2020). Functional brain architecture is associated with the rate of tau accumulation in Alzheimer's disease. *Nat Commun, 11*(1), 347. doi:10.1038/s41467-019-14159-1

Frautschy, S. A., Yang, F., Irrizarry, M., Hyman, B., Saido, T. C., Hsiao, K., & Cole, G. M. (1998). Microglial response to amyloid plaques in APPsw transgenic mice. *Am J Pathol, 152*(1), 307-317.

Frost, B., Jacks, R. L., & Diamond, M. I. (2009). Propagation of tau misfolding from the outside to the inside of a cell. *J Biol Chem, 284*(19), 12845-12852. doi:10.1074/jbc.M808759200

Gao, X., Carroni, M., Nussbaum-Krammer, C., Mogk, A., Nillegoda, N. B., Szlachcic, A., . . . Bukau, B. (2015). Human Hsp70 Disaggregase Reverses Parkinson's-Linked α-Synuclein Amyloid Fibrils. *Mol Cell, 59*(5), 781-793. doi:10.1016/j.molcel.2015.07.012

Gerhard, A., Pavese, N., Hotton, G., Turkheimer, F., Es, M., Hammers, A., . . . Brooks, D. J. (2006). In vivo imaging of microglial activation with [11C](R)-PK11195 PET in idiopathic Parkinson's disease. *Neurobiol Dis, 21*(2), 404-412. doi:10.1016/j.nbd.2005.08.002

Giehm, L., & Otzen, D. E. (2010). Strategies to increase the reproducibility of protein fibrillization in plate reader assays. *Anal Biochem, 400*(2), 270-281. doi:10.1016/j.ab.2010.02.001

Gilch, S., Chitoor, N., Taguchi, Y., Stuart, M., Jewell, J. E., & Schätzl, H. M. (2011). Chronic wasting disease. *Top Curr Chem, 305*, 51-77. doi:10.1007/128_2011_159

Glass, C. K., Saijo, K., Winner, B., Marchetto, M. C., & Gage, F. H. (2010). Mechanisms underlying inflammation in neurodegeneration. *Cell, 140*(6), 918-934. doi:10.1016/j.cell.2010.02.016

Glover, J. R., Kowal, A. S., Schirmer, E. C., Patino, M. M., Liu, J.-J., & Lindquist, S. (1997). Self-Seeded Fibers Formed by Sup35, the Protein Determinant of [PSI+], a Heritable Prion-like Factor of S. cerevisiae. *Cell, 89*(5), 811-819. doi:https://doi.org/10.1016/S0092-8674(00)80264-0

Glover, J. R., & Lindquist, S. (1998). Hsp104, Hsp70, and Hsp40: a novel chaperone system that rescues previously aggregated proteins. *Cell, 94*(1), 73-82. doi:10.1016/s0092-8674(00)81223-4

Goedert, M. (2015). NEURODEGENERATION. Alzheimer's and Parkinson's diseases: The prion concept in relation to assembled Aβ, tau, and α-synuclein. *Science, 349*(6248), 1255555. doi:10.1126/science.1255555

Goedert, M. (2016). The ordered assembly of tau is the gain-of-toxic function that causes human tauopathies. *Alzheimers Dement, 12*(10), 1040-1050. doi:10.1016/j.jalz.2016.09.001

Goedert, M., Jakes, R., Spillantini, M. G., Hasegawa, M., Smith, M. J., & Crowther, R. A. (1996). Assembly of microtubule-associated protein tau into Alzheimer-like filaments induced by sulphated glycosaminoglycans. *Nature, 383*(6600), 550-553. doi:10.1038/383550a0

Gómez-Isla, T., Hollister, R., West, H., Mui, S., Growdon, J. H., Petersen, R. C., . . . Hyman, B. T. (1997). Neuronal loss correlates with but exceeds neurofibrillary tangles in Alzheimer's disease. *Ann Neurol, 41*(1), 17-24. doi:10.1002/ana.410410106

Gousset, K., Schiff, E., Langevin, C., Marijanovic, Z., Caputo, A., Browman, D. T., . . . Zurzolo, C. (2009). Prions hijack tunnelling nanotubes for intercellular spread. *Nat Cell Biol, 11*(3), 328-336. doi:10.1038/ncb1841

Gribaudo, S., Tixador, P., Bousset, L., Fenyi, A., Lino, P., Melki, R., . . . Perrier, A. L. (2019). Propagation of α-Synuclein Strains within Human Reconstructed Neuronal Network. *Stem Cell Reports, 12*(2), 230-244. doi:10.1016/j.stemcr.2018.12.007

Guo, J. L., Covell, D. J., Daniels, J. P., Iba, M., Stieber, A., Zhang, B., . . . Lee, V. M. (2013). Distinct α-synuclein strains differentially promote tau inclusions in neurons. *Cell, 154*(1), 103-117. doi:10.1016/j.cell.2013.05.057

Guo, J. L., & Lee, V. M. (2011). Seeding of normal Tau by pathological Tau conformers drives pathogenesis of Alzheimer-like tangles. *J Biol Chem, 286*(17), 15317-15331. doi:10.1074/jbc.M110.209296

Guo, J. L., Narasimhan, S., Changolkar, L., He, Z., Stieber, A., Zhang, B., . . . Lee, V. M. (2016). Unique pathological tau conformers from Alzheimer's brains transmit tau pathology in nontransgenic mice. *J Exp Med, 213*(12), 2635-2654. doi:10.1084/jem.20160833

Guo, Q., Lehmer, C., Martínez-Sánchez, A., Rudack, T., Beck, F., Hartmann, H., . . . Fernández-Busnadiego, R. (2018). In Situ Structure of Neuronal C9orf72 Poly-GA Aggregates Reveals Proteasome Recruitment. *Cell, 172*(4), 696-705.e612. doi:10.1016/j.cell.2017.12.030

Guo, Y. J., Xiong, H., Chen, K., Zou, J. J., & Lei, P. (2022). Brain regions susceptible to alpha-synuclein spreading. *Mol Psychiatry, 27*(1), 758-770. doi:10.1038/s41380-021-01296-7

Halfmann, R., Jarosz, D. F., Jones, S. K., Chang, A., Lancaster, A. K., & Lindquist, S. (2012). Prions are a common mechanism for phenotypic inheritance in wild yeasts. *Nature, 482*(7385), 363-368. doi:10.1038/nature10875

Hansen, C., Angot, E., Bergström, A. L., Steiner, J. A., Pieri, L., Paul, G., . . . Brundin, P. (2011). α-Synuclein propagates from mouse brain to grafted dopaminergic neurons and seeds aggregation in cultured human cells. *J Clin Invest, 121*(2), 715-725. doi:10.1172/jci43366

Hartl, F. U., & Hayer-Hartl, M. (2009). Converging concepts of protein folding in vitro and in vivo. *Nat Struct Mol Biol, 16*(6), 574-581. doi:10.1038/nsmb.1591

He, Z., McBride, J. D., Xu, H., Changolkar, L., Kim, S. J., Zhang, B., . . . Lee, V. M. (2020). Transmission of tauopathy strains is independent of their isoform composition. *Nat Commun, 11*(1), 7. doi:10.1038/s41467-019-13787-x

Heneka, M. T., Carson, M. J., El Khoury, J., Landreth, G. E., Brosseron, F., Feinstein, D. L., . . . Kummer, M. P. (2015). Neuroinflammation in Alzheimer's disease. *Lancet Neurol, 14*(4), 388-405. doi:10.1016/s1474-4422(15)70016-5

Herva, M. E., & Spillantini, M. G. (2015). Parkinson's disease as a member of Prion-like disorders. *Virus Res, 207*, 38-46. doi:10.1016/j.virusres.2014.10.016

Hickman, S., Izzy, S., Sen, P., Morsett, L., & El Khoury, J. (2018). Microglia in neurodegeneration. *Nature Neuroscience, 21*(10), 1359-1369. doi:10.1038/s41593-018-0242-x

Hickman, S. E., Allison, E. K., & El Khoury, J. (2008). Microglial dysfunction and defective beta-amyloid clearance pathways in aging Alzheimer's disease mice. *J Neurosci, 28*(33), 8354-8360. doi:10.1523/jneurosci.0616-08.2008

Hipp, M. S., Kasturi, P., & Hartl, F. U. (2019). The proteostasis network and its decline in ageing. *Nat Rev Mol Cell Biol, 20*(7), 421-435. doi:10.1038/s41580-019-0101-y

Hofmann, J. P., Denner, P., Nussbaum-Krammer, C., Kuhn, P. H., Suhre, M. H., Scheibel, T., . . . Vorberg, I. M. (2013). Cell-to-cell propagation of infectious cytosolic protein aggregates. *Proc Natl Acad Sci U S A, 110*(15), 5951-5956. doi:10.1073/pnas.1217321110

Holmes, B. B., DeVos, S. L., Kfoury, N., Li, M., Jacks, R., Yanamandra, K., . . . Diamond, M. I. (2013). Heparan sulfate proteoglycans mediate internalization and propagation of specific proteopathic seeds. *Proc Natl Acad Sci U S A, 110*(33), E3138-3147. doi:10.1073/pnas.1301440110

Hoppe, S. O., Uzunoğlu, G., & Nussbaum-Krammer, C. (2021). α-Synuclein Strains: Does Amyloid Conformation Explain the Heterogeneity of Synucleinopathies? *Biomolecules, 11*(7). doi:10.3390/biom11070931

Hou, Y., Dan, X., Babbar, M., Wei, Y., Hasselbalch, S. G., Croteau, D. L., & Bohr, V. A. (2019). Ageing as a risk factor for neurodegenerative disease. *Nat Rev Neurol, 15*(10), 565-581. doi:10.1038/s41582-019-0244-7

Iba, M., Guo, J. L., McBride, J. D., Zhang, B., Trojanowski, J. Q., & Lee, V. M. (2013). Synthetic tau fibrils mediate transmission of neurofibrillary tangles in a transgenic mouse model of Alzheimer's-like tauopathy. *J Neurosci, 33*(3), 1024-1037. doi:10.1523/jneurosci.2642-12.2013

Iba, M., McDevitt, R. A., Kim, C., Roy, R., Sarantopoulou, D., Tommer, E., . . . Masliah, E. (2022). Aging exacerbates the brain inflammatory micro-environment contributing to α-synuclein pathology and functional deficits in a mouse model of DLB/PD. *Mol Neurodegener, 17*(1), 60. doi:10.1186/s13024-022-00564-6

Jackson, W. S., Borkowski, A. W., Faas, H., Steele, A. D., King, O. D., Watson, N., . . . Lindquist, S. (2009). Spontaneous generation of prion infectivity in fatal familial insomnia knockin mice. *Neuron, 63*(4), 438-450. doi:10.1016/j.neuron.2009.07.026

Jackson, W. S., Krost, C., Borkowski, A. W., & Kaczmarczyk, L. (2014). Translation of the prion protein mRNA is robust in astrocytes but does not amplify during reactive astrocytosis in the mouse brain. *PLoS One, 9*(4), e95958. doi:10.1371/journal.pone.0095958

Jarrett, J. T., & Lansbury, P. T., Jr. (1993). Seeding "one-dimensional crystallization" of amyloid: a pathogenic mechanism in Alzheimer's disease and scrapie? *Cell, 73*(6), 1055-1058. doi:10.1016/0092-8674(93)90635-4

Jay, T. M., & Witter, M. P. (1991). Distribution of hippocampal CA1 and subicular efferents in the prefrontal cortex of the rat studied by means of anterograde transport of Phaseolus vulgaris-leucoagglutinin. *J Comp Neurol, 313*(4), 574-586. doi:10.1002/cne.903130404

Jiang, P., Gan, M., Ebrahim, A. S., Lin, W. L., Melrose, H. L., & Yen, S. H. (2010). ER stress response plays an important role in aggregation of α-synuclein. *Mol Neurodegener, 5*, 56. doi:10.1186/1750-1326-5-56

Jones, B. E., & Moore, R. Y. (1977). Ascending projections of the locus coeruleus in the rat. II. Autoradiographic study. *Brain Res, 127*(1), 25-53.

Jucker, M., & Walker, L. C. (2018). Propagation and spread of pathogenic protein assemblies in neurodegenerative diseases. *Nat Neurosci, 21*(10), 1341-1349. doi:10.1038/s41593-018-0238-6

Karpowicz, R. J., Jr., Haney, C. M., Mihaila, T. S., Sandler, R. M., Petersson, E. J., & Lee, V. M. (2017). Selective imaging of internalized proteopathic α-synuclein seeds in primary neurons reveals mechanistic insight into transmission of synucleinopathies. *J Biol Chem, 292*(32), 13482-13497. doi:10.1074/jbc.M117.780296

Kaufman, S. K., Sanders, D. W., Thomas, T. L., Ruchinskas, A. J., Vaquer-Alicea, J., Sharma, A. M., . . . Diamond, M. I. (2016). Tau Prion Strains Dictate Patterns of Cell Pathology, Progression Rate, and Regional Vulnerability In Vivo. *Neuron, 92*(4), 796-812. doi:10.1016/j.neuron.2016.09.055

Kawles, A., Minogue, G., Zouridakis, A., Keszycki, R., Gill, N., Nassif, C., . . . Gefen, T. (2023). Differential vulnerability of the dentate gyrus to tauopathies in dementias. *Acta Neuropathol Commun, 11*(1), 1. doi:10.1186/s40478-022-01485-7

Kayed, R., & Lasagna-Reeves, C. A. (2013). Molecular mechanisms of amyloid oligomers toxicity. *J Alzheimers Dis, 33 Suppl 1*, S67-78. doi:10.3233/jad-2012-129001

Kempuraj, D., Thangavel, R., Natteru, P. A., Selvakumar, G. P., Saeed, D., Zahoor, H., . . . Zaheer, A. (2016). Neuroinflammation Induces Neurodegeneration. *J Neurol Neurosurg Spine, 1*(1).

Kim, C., Lv, G., Lee, J. S., Jung, B. C., Masuda-Suzukake, M., Hong, C. S., . . . Lee, S. J. (2016). Exposure to bacterial endotoxin generates a distinct strain of α-synuclein fibril. *Sci Rep, 6*, 30891. doi:10.1038/srep30891

Kim, S., Kwon, S. H., Kam, T. I., Panicker, N., Karuppagounder, S. S., Lee, S., . . . Ko, H. S. (2019). Transneuronal Propagation of Pathologic α-Synuclein from the Gut to the Brain Models Parkinson's Disease. *Neuron, 103*(4), 627-641.e627. doi:10.1016/j.neuron.2019.05.035

King, C. Y., & Diaz-Avalos, R. (2004). Protein-only transmission of three yeast prion strains. *Nature, 428*(6980), 319-323. doi:10.1038/nature02391

King, O. D., Gitler, A. D., & Shorter, J. (2012). The tip of the iceberg: RNA-binding proteins with prion-like domains in neurodegenerative disease. *Brain Research, 1462*, 61-80. doi:https://doi.org/10.1016/j.brainres.2012.01.016

Kobayashi, T., Manno, A., & Kakizuka, A. (2007). Involvement of valosin-containing protein (VCP)/p97 in the formation and clearance of abnormal protein aggregates. *Genes Cells, 12*(7), 889-901. doi:10.1111/j.1365-2443.2007.01099.x

Kraeuter, A. K., Guest, P. C., & Sarnyai, Z. (2019). The Y-Maze for Assessment of Spatial Working and Reference Memory in Mice. *Methods Mol Biol, 1916*, 105-111. doi:10.1007/978-1-4939-8994-2_10

Krammer, C., Kryndushkin, D., Suhre, M. H., Kremmer, E., Hofmann, A., Pfeifer, A., . . . Vorberg, I. (2009). The yeast Sup35NM domain propagates as a prion in mammalian cells. *Proc Natl Acad Sci U S A, 106*(2), 462-467. doi:10.1073/pnas.0811571106

Kraus, A., Hoyt, F., Schwartz, C. L., Hansen, B., Artikis, E., Hughson, A. G., . . . Caughey, B. (2021). High-resolution structure and strain comparison of infectious mammalian prions. *Mol Cell, 81*(21), 4540-4551.e4546. doi:10.1016/j.molcel.2021.08.011

Kryndushkin, D. S., Alexandrov, I. M., Ter-Avanesyan, M. D., & Kushnirov, V. V. (2003). Yeast [PSI+] prion aggregates are formed by small Sup35 polymers fragmented by Hsp104. *J Biol Chem, 278*(49), 49636-49643. doi:10.1074/jbc.M307996200

Kuusisto, E., Salminen, A., & Alafuzoff, I. (2001). Ubiquitin-binding protein p62 is present in neuronal and glial inclusions in human tauopathies and synucleinopathies. *Neuroreport, 12*(10), 2085-2090. doi:10.1097/00001756-200107200-00009

Kuzuhara, S., Mori, H., Izumiyama, N., Yoshimura, M., & Ihara, Y. (1988). Lewy bodies are ubiquitinated. A light and electron microscopic immunocytochemical study. *Acta Neuropathol, 75*(4), 345-353. doi:10.1007/bf00687787

Laganowsky, A., Liu, C., Sawaya, M. R., Whitelegge, J. P., Park, J., Zhao, M., . . . Eisenberg, D. (2012). Atomic view of a toxic amyloid small oligomer. *Science, 335*(6073), 1228-1231. doi:10.1126/science.1213151

Lasagna-Reeves, C. A., Castillo-Carranza, D. L., Sengupta, U., Clos, A. L., Jackson, G. R., & Kayed, R. (2011). Tau oligomers impair memory and induce synaptic and mitochondrial dysfunction in wild-type mice. *Molecular Neurodegeneration, 6*(1), 39. doi:10.1186/1750-1326-6-39

Lashuel, H. A., Hartley, D., Petre, B. M., Walz, T., & Lansbury, P. T., Jr. (2002). Neurodegenerative disease: amyloid pores from pathogenic mutations. *Nature, 418*(6895), 291. doi:10.1038/418291a

Lau, A., So, R. W. L., Lau, H. H. C., Sang, J. C., Ruiz-Riquelme, A., Fleck, S. C., . . . Watts, J. C. (2020). α-Synuclein strains target distinct brain regions and cell types. *Nat Neurosci, 23*(1), 21-31. doi:10.1038/s41593-019-0541-x

Lee, D. C., Rizer, J., Selenica, M. L., Reid, P., Kraft, C., Johnson, A., . . . Morgan, D. (2010). LPS- induced inflammation exacerbates phospho-tau pathology in rTg4510 mice. *J Neuroinflammation, 7*, 56. doi:10.1186/1742-2094-7-56

Lee, V. M., Goedert, M., & Trojanowski, J. Q. (2001). Neurodegenerative tauopathies. *Annu Rev Neurosci, 24*, 1121-1159. doi:10.1146/annurev.neuro.24.1.1121

Legname, G., Baskakov, I. V., Nguyen, H. O., Riesner, D., Cohen, F. E., DeArmond, S. J., & Prusiner, S. B. (2004). Synthetic mammalian prions. *Science, 305*(5684), 673-676. doi:10.1126/science.1100195

Legname, G., & Moda, F. (2017). The Prion Concept and Synthetic Prions. *Prog Mol Biol Transl Sci, 150*, 147-156. doi:10.1016/bs.pmbts.2017.06.002

Lei, P., Ayton, S., Moon, S., Zhang, Q., Volitakis, I., Finkelstein, D. I., & Bush, A. I. (2014). Motor and cognitive deficits in aged tau knockout mice in two background strains. *Mol Neurodegener, 9*, 29. doi:10.1186/1750-1326-9-29

Leng, F., & Edison, P. (2021). Neuroinflammation and microglial activation in Alzheimer disease: where do we go from here? *Nat Rev Neurol, 17*(3), 157-172. doi:10.1038/s41582-020-00435-y

LeVine, H., 3rd. (1993). Thioflavine T interaction with synthetic Alzheimer's disease beta-amyloid peptides: detection of amyloid aggregation in solution. *Protein Sci, 2*(3), 404-410. doi:10.1002/pro.5560020312

Liddelow, S. A., Guttenplan, K. A., Clarke, L. E., Bennett, F. C., Bohlen, C. J., Schirmer, L., . . . Barres, B. A. (2017). Neurotoxic reactive astrocytes are induced by activated microglia. *Nature, 541*(7638), 481-487. doi:10.1038/nature21029

Liebman, S. W., & Chernoff, Y. O. (2012). Prions in yeast. *Genetics, 191*(4), 1041-1072. doi:10.1534/genetics.111.137760

Lindersson, E., Beedholm, R., Højrup, P., Moos, T., Gai, W., Hendil, K. B., & Jensen, P. H. (2004). Proteasomal inhibition by alpha-synuclein filaments and oligomers. *J Biol Chem, 279*(13), 12924-12934. doi:10.1074/jbc.M306390200

Liu, J. J., Sondheimer, N., & Lindquist, S. L. (2002). Changes in the middle region of Sup35 profoundly alter the nature of epigenetic inheritance for the yeast prion [PSI+]. *Proc Natl Acad Sci U S A, 99 Suppl 4*(Suppl 4), 16446-16453. doi:10.1073/pnas.252652099

Liu, S., Hossinger, A., Göbbels, S., & Vorberg, I. M. (2017). Prions on the run: How extracellular vesicles serve as delivery vehicles for self-templating protein aggregates. *Prion, 11*(2), 98-112. doi:10.1080/19336896.2017.1306162

Liu, S., Hossinger, A., Heumüller, S. E., Hornberger, A., Buravlova, O., Konstantoulea, K., . . . Vorberg, I. M. (2021). Highly efficient intercellular spreading of protein misfolding mediated by viral ligand-receptor interactions. *Nat Commun, 12*(1), 5739. doi:10.1038/s41467-021-25855-2

Liu, S., Hossinger, A., Hofmann, J. P., Denner, P., & Vorberg, I. M. (2016). Horizontal Transmission of Cytosolic Sup35 Prions by Extracellular Vesicles. *mBio, 7*(4). doi:10.1128/mBio.00915-16

Lohmann, S., Bernis, M. E., Tachu, B. J., Ziemski, A., Grigoletto, J., & Tamgüney, G. (2019). Oral and intravenous transmission of α-synuclein fibrils to mice. *Acta Neuropathol, 138*(4), 515-533. doi:10.1007/s00401-019-02037-5

Louros, N., Schymkowitz, J., & Rousseau, F. (2023). Mechanisms and pathology of protein misfolding and aggregation. *Nat Rev Mol Cell Biol, 24*(12), 912-933. doi:10.1038/s41580-023-00647-2

Lövestam, S., Koh, F. A., van Knippenberg, B., Kotecha, A., Murzin, A. G., Goedert, M., & Scheres, S. H. W. (2022). Assembly of recombinant tau into filaments identical to those of Alzheimer's disease and chronic traumatic encephalopathy. *Elife, 11*. doi:10.7554/eLife.76494

Lövestam, S., Schweighauser, M., Matsubara, T., Murayama, S., Tomita, T., Ando, T., . . . Scheres, S. H. W. (2021). Seeded assembly in vitro does not replicate the structures of α-synuclein filaments from multiple system atrophy. *FEBS Open Bio, 11*(4), 999-1013. doi:10.1002/2211-5463.13110

Luk, K. C., Covell, D. J., Kehm, V. M., Zhang, B., Song, I. Y., Byrne, M. D., . . . Lee, V. M. (2016). Molecular and Biological Compatibility with Host Alpha-Synuclein Influences Fibril Pathogenicity. *Cell Rep, 16*(12), 3373-3387. doi:10.1016/j.celrep.2016.08.053

Luk, K. C., Kehm, V., Carroll, J., Zhang, B., O'Brien, P., Trojanowski, J. Q., & Lee, V. M. (2012a). Pathological α-synuclein transmission initiates Parkinson-like neurodegeneration in nontransgenic mice. *Science, 338*(6109), 949-953. doi:10.1126/science.1227157

Luk, K. C., Kehm, V. M., Zhang, B., O'Brien, P., Trojanowski, J. Q., & Lee, V. M. (2012b). Intracerebral inoculation of pathological α-synuclein initiates a rapidly progressive neurodegenerative α-synucleinopathy in mice. *J Exp Med, 209*(5), 975-986. doi:10.1084/jem.20112457

Luk, K. C., Song, C., O'Brien, P., Stieber, A., Branch, J. R., Brunden, K. R., . . . Lee, V. M. (2009). Exogenous alpha-synuclein fibrils seed the formation of Lewy body-like intracellular inclusions in cultured cells. *Proc Natl Acad Sci U S A, 106*(47), 20051-20056. doi:10.1073/pnas.0908005106

Luna, E., Decker, S. C., Riddle, D. M., Caputo, A., Zhang, B., Cole, T., . . . Luk, K. C. (2018). Differential α-synuclein expression contributes to selective vulnerability of hippocampal neuron subpopulations to fibril-induced toxicity. *Acta Neuropathol, 135*(6), 855-875. doi:10.1007/s00401-018-1829-8

Ma, J., Zhang, J., & Yan, R. (2022). Recombinant Mammalian Prions: The "Correctly" Misfolded Prion Protein Conformers. *Viruses, 14*(9). doi:10.3390/v14091940

Makarava, N., & Baskakov, I. V. (2012). Genesis of tramsmissible protein states via deformed templating. *Prion, 6*(3), 252-255. doi:10.4161/pri.19930

Makarava, N., Kovacs, G. G., Bocharova, O., Savtchenko, R., Alexeeva, I., Budka, H., . . . Baskakov, I. V. (2010). Recombinant prion protein induces a new transmissible prion disease in wild-type animals. *Acta Neuropathol, 119*(2), 177-187. doi:10.1007/s00401-009-0633-x

Makarava, N., Savtchenko, R., Lasch, P., Beekes, M., & Baskakov, I. V. (2018). Preserving prion strain identity upon replication of prions in vitro using recombinant prion protein. *Acta Neuropathol Commun, 6*(1), 92. doi:10.1186/s40478-018-0597-y

Manka, S. W., Wenborn, A., Betts, J., Joiner, S., Saibil, H. R., Collinge, J., & Wadsworth, J. D. F. (2023). A structural basis for prion strain diversity. *Nat Chem Biol, 19*(5), 607-613. doi:10.1038/s41589-022-01229-7

Manka, S. W., Zhang, W., Wenborn, A., Betts, J., Joiner, S., Saibil, H. R., . . . Wadsworth, J. D. F. (2022). 2.7Å cryo-EM structure of ex vivo RML prion fibrils. *Nat Commun, 13*(1), 4004. doi:10.1038/s41467-022-30457-7

Mao, X., Ou, M. T., Karuppagounder, S. S., Kam, T. I., Yin, X., Xiong, Y., . . . Dawson, T. M. (2016). Pathological α-synuclein transmission initiated by binding lymphocyte-activation gene 3. *Science, 353*(6307). doi:10.1126/science.aah3374

Marasco, R. A. (2020). Current and evolving treatment strategies for the Alzheimer disease continuum. *Am J Manag Care, 26*(8 Suppl), S167-s176. doi:10.37765/ajmc.2020.88481

Marchante, R., Beal, D. M., Koloteva-Levine, N., Purton, T. J., Tuite, M. F., & Xue, W. F. (2017). The physical dimensions of amyloid aggregates control their infective potential as prion particles. *Elife, 6*. doi:10.7554/eLife.27109

Masuda-Suzukake, M., Nonaka, T., Hosokawa, M., Oikawa, T., Arai, T., Akiyama, H., . . . Hasegawa, M. (2013). Prion-like spreading of pathological α-synuclein in brain. *Brain, 136*(Pt 4), 1128-1138. doi:10.1093/brain/awt037

McGeer, P. L., Akiyama, H., Itagaki, S., & McGeer, E. G. (1989). Immune system response in Alzheimer's disease. *Can J Neurol Sci, 16*(4 Suppl), 516-527. doi:10.1017/s0317167100029863

McGeer, P. L., Itagaki, S., Boyes, B. E., & McGeer, E. G. (1988). Reactive microglia are positive for HLA-DR in the substantia nigra of Parkinson's and Alzheimer's disease brains. *Neurology, 38*(8), 1285-1291. doi:10.1212/wnl.38.8.1285

McGlinchey, R. P., Kryndushkin, D., & Wickner, R. B. (2011). Suicidal [PSI+] is a lethal yeast prion. *Proc Natl Acad Sci U S A, 108*(13), 5337-5341. doi:10.1073/pnas.1102762108

Medeiros, R., & LaFerla, F. M. (2013). Astrocytes: conductors of the Alzheimer disease neuroinflammatory symphony. *Exp Neurol, 239*, 133-138. doi:10.1016/j.expneurol.2012.10.007

Meng, L., Liu, C., Li, Y., Chen, G., Xiong, M., Yu, T., . . . Zhang, Z. (2023). The yeast prion protein Sup35 initiates α-synuclein pathology in mouse models of Parkinson's disease. *Sci Adv, 9*(44), eadj1092. doi:10.1126/sciadv.adj1092

Mercer, R. C. C., & Harris, D. A. (2023). Mechanisms of prion-induced toxicity. *Cell Tissue Res, 392*(1), 81-96. doi:10.1007/s00441-022-03683-0

Meyer, H., Bug, M., & Bremer, S. (2012). Emerging functions of the VCP/p97 AAA-ATPase in the ubiquitin system. *Nat Cell Biol, 14*(2), 117-123. doi:10.1038/ncb2407

Meyer, H., & Weihl, C. C. (2014). The VCP/p97 system at a glance: connecting cellular function to disease pathogenesis. *J Cell Sci, 127*(Pt 18), 3877-3883. doi:10.1242/jcs.093831

Mezias, C., Rey, N., Brundin, P., & Raj, A. (2020). Neural connectivity predicts spreading of alpha-synuclein pathology in fibril-injected mouse models: Involvement of retrograde and anterograde axonal propagation. *Neurobiol Dis, 134*, 104623. doi:10.1016/j.nbd.2019.104623

Michiels, E., Liu, S., Gallardo, R., Louros, N., Mathelié-Guinlet, M., Dufrêne, Y., . . . Rousseau, F. (2020). Entropic Bristles Tune the Seeding Efficiency of Prion-Nucleating Fragments. *Cell Rep, 30*(8), 2834-2845.e2833. doi:10.1016/j.celrep.2020.01.098

Mogk, A., Kummer, E., & Bukau, B. (2015). Cooperation of Hsp70 and Hsp100 chaperone machines in protein disaggregation. *Front Mol Biosci, 2*, 22. doi:10.3389/fmolb.2015.00022

Mollenhauer, B., Trautmann, E., Taylor, P., Manninger, P., Sixel-Döring, F., Ebentheuer, J., . . . Schlossmacher, M. G. (2013). Total CSF α-synuclein is lower in de novo Parkinson patients than in healthy subjects. *Neurosci Lett, 532*, 44-48. doi:10.1016/j.neulet.2012.11.004

Morales, I., Jiménez, J. M., Mancilla, M., & Maccioni, R. B. (2013). Tau oligomers and fibrils induce activation of microglial cells. *J Alzheimers Dis, 37*(4), 849-856. doi:10.3233/jad-131843

Morley, J. F., Brignull, H. R., Weyers, J. J., & Morimoto, R. I. (2002). The threshold for polyglutamine-expansion protein aggregation and cellular toxicity is dynamic and influenced by aging in Caenorhabditis elegans. *Proc Natl Acad Sci U S A, 99*(16), 10417-10422. doi:10.1073/pnas.152161099

Muchowski, P. J., & Wacker, J. L. (2005). Modulation of neurodegeneration by molecular chaperones. *Nat Rev Neurosci, 6*(1), 11-22. doi:10.1038/nrn1587

Nachman, E., Wentink, A. S., Madiona, K., Bousset, L., Katsinelos, T., Allinson, K., . . . Nussbaum-Krammer, C. (2020). Disassembly of Tau fibrils by the human Hsp70 disaggregation machinery generates small seeding-competent species. *J Biol Chem, 295*(28), 9676-9690. doi:10.1074/jbc.RA120.013478

Narasimhan, S., Guo, J. L., Changolkar, L., Stieber, A., McBride, J. D., Silva, L. V., . . . Lee, V. M. Y. (2017). Pathological Tau Strains from Human Brains Recapitulate the Diversity of Tauopathies in Nontransgenic Mouse Brain. *J Neurosci, 37*(47), 11406-11423. doi:10.1523/jneurosci.1230-17.2017

Nies, S. H., Takahashi, H., Herber, C. S., Huttner, A., Chase, A., & Strittmatter, S. M. (2021). Spreading of Alzheimer tau seeds is enhanced by aging and template matching with limited impact of amyloid-β. *J Biol Chem, 297*(4), 101159. doi:10.1016/j.jbc.2021.101159

Nillegoda, N. B., Wentink, A. S., & Bukau, B. (2018). Protein Disaggregation in Multicellular Organisms. *Trends Biochem Sci, 43*(4), 285-300. doi:10.1016/j.tibs.2018.02.003

Nimmerjahn, A., Kirchhoff, F., & Helmchen, F. (2005). Resting microglial cells are highly dynamic surveillants of brain parenchyma in vivo. *Science, 308*(5726), 1314-1318. doi:10.1126/science.1110647

Nixon, R. A. (2013). The role of autophagy in neurodegenerative disease. *Nature Medicine, 19*(8), 983-997. doi:10.1038/nm.3232

Oliveira, A. M. M., Hemstedt, T. J., & Bading, H. (2012). Rescue of aging-associated decline in Dnmt3a2 expression restores cognitive abilities. *Nature Neuroscience, 15*(8), 1111-1113. doi:10.1038/nn.3151

Patino, M. M., Liu, J. J., Glover, J. R., & Lindquist, S. (1996). Support for the prion hypothesis for inheritance of a phenotypic trait in yeast. *Science, 273*(5275), 622-626. doi:10.1126/science.273.5275.622

Patterson, K. R., Ward, S. M., Combs, B., Voss, K., Kanaan, N. M., Morfini, G., . . . Binder, L. I. (2011). Heat shock protein 70 prevents both tau aggregation and the inhibitory effects of preexisting tau aggregates on fast axonal transport. *Biochemistry, 50*(47), 10300-10310. doi:10.1021/bi2009147

Paushkin, S. V., Kushnirov, V. V., Smirnov, V. N., & Ter-Avanesyan, M. D. (1996). Propagation of the yeast prion-like [psi+] determinant is mediated by oligomerization of the SUP35-encoded polypeptide chain release factor. *Embo j, 15*(12), 3127-3134.

Peelaerts, W., & Baekelandt, V. (2023). α-Synuclein Structural Diversity and the Cellular Environment in α-Synuclein Transmission Models and Humans. *Neurotherapeutics, 20*(1), 67-82. doi:10.1007/s13311-023-01365-5

Peelaerts, W., Bousset, L., Van der Perren, A., Moskalyuk, A., Pulizzi, R., Giugliano, M., . . . Baekelandt, V. (2015). α-Synuclein strains cause distinct synucleinopathies after local and systemic administration. *Nature, 522*(7556), 340-344. doi:10.1038/nature14547

Peeraer, E., Bottelbergs, A., Van Kolen, K., Stancu, I. C., Vasconcelos, B., Mahieu, M., . . . Moechars, D. (2015). Intracerebral injection of preformed synthetic tau fibrils initiates widespread tauopathy and neuronal loss in the brains of tau transgenic mice. *Neurobiol Dis, 73*, 83-95. doi:10.1016/j.nbd.2014.08.032

Peng, C., Gathagan, R. J., Covell, D. J., Medellin, C., Stieber, A., Robinson, J. L., . . . Lee, V. M. (2018). Cellular milieu imparts distinct pathological α-synuclein strains in α-synucleinopathies. *Nature, 557*(7706), 558-563. doi:10.1038/s41586-018-0104-4

Phan, J. M., Creekmore, B. C., Nguyen, A. T., Bershadskaya, D. D., Darwich, N. F., & Lee, E. B. (2023). Novel VCP activator reverses multisystem proteinopathy nuclear proteostasis defects and enhances TDP-43 aggregate clearance. *bioRxiv*. doi:10.1101/2023.03.15.532082

Pieri, L., Madiona, K., Bousset, L., & Melki, R. (2012). Fibrillar α-synuclein and huntingtin exon 1 assemblies are toxic to the cells. *Biophys J, 102*(12), 2894-2905. doi:10.1016/j.bpj.2012.04.050

Polydoro, M., Acker, C. M., Duff, K., Castillo, P. E., & Davies, P. (2009). Age-dependent impairment of cognitive and synaptic function in the htau mouse model of tau pathology. *J Neurosci, 29*(34), 10741-10749. doi:10.1523/jneurosci.1065-09.2009

Porta, S., Xu, Y., Lehr, T., Zhang, B., Meymand, E., Olufemi, M., . . . Lee, V. M. (2021). Distinct brain-derived TDP-43 strains from FTLD-TDP subtypes induce diverse morphological TDP-43 aggregates and spreading patterns in vitro and in vivo. *Neuropathol Appl Neurobiol, 47*(7), 1033-1049. doi:10.1111/nan.12732

Porta, S., Xu, Y., Restrepo, C. R., Kwong, L. K., Zhang, B., Brown, H. J., . . . Lee, V. M. (2018). Patient-derived frontotemporal lobar degeneration brain extracts induce formation and spreading of TDP-43 pathology in vivo. *Nat Commun, 9*(1), 4220. doi:10.1038/s41467-018-06548-9

Pothlichet, J., Heidmann, T., & Mangeney, M. (2006). A recombinant endogenous retrovirus amplified in a mouse neuroblastoma is involved in tumor growth in vivo. *Int J Cancer, 119*(4), 815-822. doi:10.1002/ijc.21935

Prusiner, S. B. (1982). Novel proteinaceous infectious particles cause scrapie. *Science, 216*(4542), 136-144. doi:10.1126/science.6801762

Prusiner, S. B. (1998). Prions. *Proc Natl Acad Sci U S A, 95*(23), 13363-13383. doi:10.1073/pnas.95.23.13363

Prusiner, S. B., Woerman, A. L., Mordes, D. A., Watts, J. C., Rampersaud, R., Berry, D. B., . . . Giles, K. (2015). Evidence for α-synuclein prions causing multiple system atrophy in humans with parkinsonism. *Proc Natl Acad Sci U S A, 112*(38), E5308-5317. doi:10.1073/pnas.1514475112

Puangmalai, N., Bhatt, N., Montalbano, M., Sengupta, U., Gaikwad, S., Ventura, F., . . . Kayed, R. (2020). Internalization mechanisms of brain-derived tau oligomers from patients with Alzheimer's disease, progressive supranuclear palsy and dementia with Lewy bodies. *Cell Death Dis, 11*(5), 314. doi:10.1038/s41419-020-2503-3

Rabinovich, E., Kerem, A., Fröhlich, K. U., Diamant, N., & Bar-Nun, S. (2002). AAA-ATPase p97/Cdc48p, a cytosolic chaperone required for endoplasmic reticulum-associated protein degradation. *Mol Cell Biol, 22*(2), 626-634. doi:10.1128/mcb.22.2.626-634.2002

Rahayel, S., Mišić, B., Zheng, Y. Q., Liu, Z. Q., Abdelgawad, A., Abbasi, N., . . . Luk, K. C. (2022). Differentially targeted seeding reveals unique pathological alpha-synuclein propagation patterns. *Brain, 145*(5), 1743-1756. doi:10.1093/brain/awab440

Ramirez, D. M. O., Whitesell, J. D., Bhagwat, N., Thomas, T. L., Ajay, A. D., Nawaby, A., . . . Diamond, M. I. (2023). Endogenous pathology in tauopathy mice progresses via brain networks. *bioRxiv*. doi:10.1101/2023.05.23.541792

Rangel, A., Race, B., Phillips, K., Striebel, J., Kurtz, N., & Chesebro, B. (2014). Distinct patterns of spread of prion infection in brains of mice expressing anchorless or anchored forms of prion protein. *Acta Neuropathol Commun, 2*, 8. doi:10.1186/2051-5960-2-8

Reid, M. J., Beltran-Lobo, P., Johnson, L., Perez-Nievas, B. G., & Noble, W. (2020). Astrocytes in Tauopathies. *Front Neurol, 11*, 572850. doi:10.3389/fneur.2020.572850

Rey, N. L., Bousset, L., George, S., Madaj, Z., Meyerdirk, L., Schulz, E., . . . Brundin, P. (2019). α-Synuclein conformational strains spread, seed and target neuronal cells differentially after injection into the olfactory bulb. *Acta Neuropathol Commun, 7*(1), 221. doi:10.1186/s40478-019-0859-3

Rey, N. L., George, S., Steiner, J. A., Madaj, Z., Luk, K. C., Trojanowski, J. Q., . . . Brundin, P. (2018). Spread of aggregates after olfactory bulb injection of α-synuclein fibrils is associated with early neuronal loss and is reduced long term. *Acta Neuropathol, 135*(1), 65-83. doi:10.1007/s00401-017-1792-9

Rey, N. L., Petit, G. H., Bousset, L., Melki, R., & Brundin, P. (2013). Transfer of human α-synuclein from the olfactory bulb to interconnected brain regions in mice. *Acta Neuropathol, 126*(4), 555-573. doi:10.1007/s00401-013-1160-3

Riemenschneider, H., Guo, Q., Bader, J., Frottin, F., Farny, D., Kleinberger, G., . . . Edbauer, D. (2022). Gel-like inclusions of C-terminal fragments of TDP-43 sequester stalled proteasomes in neurons. *EMBO Rep, 23*(6), e53890. doi:10.15252/embr.202153890

Riemschoss, K., Arndt, V., Bolognesi, B., von Eisenhart-Rothe, P., Liu, S., Buravlova, O., . . . Vorberg, I. M. (2019). Fibril-induced glutamine-/asparagine-rich prions recruit stress granule proteins in mammalian cells. *Life Sci Alliance, 2*(4). doi:10.26508/lsa.201800280

Riera-Tur, I., Schäfer, T., Hornburg, D., Mishra, A., da Silva Padilha, M., Fernández-Mosquera, L., . . . Dudanova, I. (2022). Amyloid-like aggregating proteins cause lysosomal defects in neurons via gain-of-function toxicity. *Life Sci Alliance, 5*(3). doi:10.26508/lsa.202101185

Risold, P. Y., & Swanson, L. W. (1996). Structural evidence for functional domains in the rat hippocampus. *Science, 272*(5267), 1484-1486. doi:10.1126/science.272.5267.1484

Ross, E. D., Edskes, H. K., Terry, M. J., & Wickner, R. B. (2005a). Primary sequence independence for prion formation. *Proc Natl Acad Sci U S A, 102*(36), 12825-12830. doi:10.1073/pnas.0506136102

Ross, E. D., Minton, A., & Wickner, R. B. (2005b). Prion domains: sequences, structures and interactions. *Nat Cell Biol, 7*(11), 1039-1044. doi:10.1038/ncb1105-1039

Saman, S., Kim, W., Raya, M., Visnick, Y., Miro, S., Saman, S., . . . Hall, G. F. (2012). Exosome-associated tau is secreted in tauopathy models and is selectively phosphorylated in cerebrospinal fluid in early Alzheimer disease. *J Biol Chem, 287*(6), 3842-3849. doi:10.1074/jbc.M111.277061

Sanders, D. W., Kaufman, S. K., DeVos, S. L., Sharma, A. M., Mirbaha, H., Li, A., . . . Diamond, M. I. (2014). Distinct tau prion strains propagate in cells and mice and define different tauopathies. *Neuron, 82*(6), 1271-1288. doi:10.1016/j.neuron.2014.04.047

Scheckel, C., & Aguzzi, A. (2018). Prions, prionoids and protein misfolding disorders. *Nat Rev Genet, 19*(7), 405-418. doi:10.1038/s41576-018-0011-4

Scheres, S. H., Zhang, W., Falcon, B., & Goedert, M. (2020). Cryo-EM structures of tau filaments. *Curr Opin Struct Biol, 64*, 17-25. doi:10.1016/j.sbi.2020.05.011

Schöll, M., Lockhart, S. N., Schonhaut, D. R., O'Neil, J. P., Janabi, M., Ossenkoppele, R., . . . Jagust, W. J. (2016). PET Imaging of Tau Deposition in the Aging Human Brain. *Neuron, 89*(5), 971-982. doi:10.1016/j.neuron.2016.01.028

Schröder, R., Watts, G. D., Mehta, S. G., Evert, B. O., Broich, P., Fliessbach, K., . . . Thal, D. R. (2005). Mutant valosin-containing protein causes a novel type of frontotemporal dementia. *Ann Neurol, 57*(3), 457-461. doi:10.1002/ana.20407

Schweighauser, M., Shi, Y., Tarutani, A., Kametani, F., Murzin, A. G., Ghetti, B., . . . Goedert, M. (2020). Structures of α-synuclein filaments from multiple system atrophy. *Nature, 585*(7825), 464-469. doi:10.1038/s41586-020-2317-6

Scialò, C., De Cecco, E., Manganotti, P., & Legname, G. (2019). Prion and Prion-Like Protein Strains: Deciphering the Molecular Basis of Heterogeneity in Neurodegeneration. *Viruses, 11*(3). doi:10.3390/v11030261

Shewmaker, F., Wickner, R. B., & Tycko, R. (2006). Amyloid of the prion domain of Sup35p has an in-register parallel beta-sheet structure. *Proc Natl Acad Sci U S A, 103*(52), 19754-19759. doi:10.1073/pnas.0609638103

Shiber, A., & Ravid, T. (2014). Chaperoning proteins for destruction: diverse roles of Hsp70 chaperones and their co-chaperones in targeting misfolded proteins to the proteasome. *Biomolecules, 4*(3), 704-724. doi:10.3390/biom4030704

Shkundina, I. S., Kushnirov, V. V., Tuite, M. F., & Ter-Avanesyan, M. D. (2006). The Role of the N-Terminal Oligopeptide Repeats of the Yeast Sup35 Prion Protein in Propagation and Transmission of Prion Variants. *Genetics, 172*(2), 827-835. doi:10.1534/genetics.105.048660

Shorter, J. (2011). The mammalian disaggregase machinery: Hsp110 synergizes with Hsp70 and Hsp40 to catalyze protein disaggregation and reactivation in a cell-free system. *PLoS One, 6*(10), e26319. doi:10.1371/journal.pone.0026319

Shorter, J., & Lindquist, S. (2006). Destruction or potentiation of different prions catalyzed by similar Hsp104 remodeling activities. *Mol Cell, 23*(3), 425-438. doi:10.1016/j.molcel.2006.05.042

Sigurdson, C. J., Bartz, J. C., & Glatzel, M. (2019). Cellular and Molecular Mechanisms of Prion Disease. *Annu Rev Pathol, 14*, 497-516. doi:10.1146/annurev-pathmechdis-012418-013109

Sjöstedt, E., Zhong, W., Fagerberg, L., Karlsson, M., Mitsios, N., Adori, C., . . . Mulder, J. (2020). An atlas of the protein-coding genes in the human, pig, and mouse brain. *Science, 367*(6482), eaay5947. doi:doi:10.1126/science.aay5947

Smethurst, P., Franklin, H., Clarke, B. E., Sidle, K., & Patani, R. (2022). The role of astrocytes in prion-like mechanisms of neurodegeneration. *Brain, 145*(1), 17-26. doi:10.1093/brain/awab366

Smethurst, P., Newcombe, J., Troakes, C., Simone, R., Chen, Y. R., Patani, R., & Sidle, K. (2016). In vitro prion-like behaviour of TDP-43 in ALS. *Neurobiol Dis, 96*, 236-247. doi:10.1016/j.nbd.2016.08.007

Sofroniew, M. V., & Vinters, H. V. (2010). Astrocytes: biology and pathology. *Acta Neuropathol, 119*(1), 7-35. doi:10.1007/s00401-009-0619-8

Soto, C. (2003). Unfolding the role of protein misfolding in neurodegenerative diseases. *Nat Rev Neurosci, 4*(1), 49-60. doi:10.1038/nrn1007

Soto, C., Estrada, L., & Castilla, J. (2006). Amyloids, prions and the inherent infectious nature of misfolded protein aggregates. *Trends Biochem Sci, 31*(3), 150-155. doi:10.1016/j.tibs.2006.01.002

Spillantini, M. G., Schmidt, M. L., Lee, V. M., Trojanowski, J. Q., Jakes, R., & Goedert, M. (1997). Alpha-synuclein in Lewy bodies. *Nature, 388*(6645), 839-840. doi:10.1038/42166

Stokholm, M. G., Iranzo, A., Østergaard, K., Serradell, M., Otto, M., Svendsen, K. B., . . . Pavese, N. (2017). Assessment of neuroinflammation in patients with idiopathic rapid-eye-movement sleep behaviour disorder: a case-control study. *Lancet Neurol, 16*(10), 789-796. doi:10.1016/s1474-4422(17)30173-4

Stoyka, L. E., Arrant, A. E., Thrasher, D. R., Russell, D. L., Freire, J., Mahoney, C. L., . . . Volpicelli-Daley, L. A. (2020). Behavioral defects associated with amygdala and cortical dysfunction in mice with seeded α-synuclein inclusions. *Neurobiol Dis, 134*, 104708. doi:10.1016/j.nbd.2019.104708

Tahir, W., Thapa, S., & Schatzl, H. M. (2022). Astrocyte in prion disease: a double-edged sword. *Neural Regen Res, 17*(8), 1659-1665. doi:10.4103/1673-5374.332202

Tanaka, M., Chien, P., Naber, N., Cooke, R., & Weissman, J. S. (2004). Conformational variations in an infectious protein determine prion strain differences. *Nature, 428*(6980), 323-328. doi:10.1038/nature02392

Tanaka, M., Collins, S. R., Toyama, B. H., & Weissman, J. S. (2006). The physical basis of how prion conformations determine strain phenotypes. *Nature, 442*(7102), 585-589. doi:10.1038/nature04922

Tapiola, T., Alafuzoff, I., Herukka, S. K., Parkkinen, L., Hartikainen, P., Soininen, H., & Pirttilä, T. (2009). Cerebrospinal fluid {beta}-amyloid 42 and tau proteins as biomarkers of Alzheimer-type pathologic changes in the brain. *Arch Neurol, 66*(3), 382-389. doi:10.1001/archneurol.2008.596

Taylor, R. C., & Dillin, A. (2011). Aging as an event of proteostasis collapse. *Cold Spring Harb Perspect Biol, 3*(5). doi:10.1101/cshperspect.a004440

Thibaudeau, T. A., Anderson, R. T., & Smith, D. M. (2018). A common mechanism of proteasome impairment by neurodegenerative disease-associated oligomers. *Nature Communications, 9*(1), 1097. doi:10.1038/s41467-018-03509-0

Thierry, A. M., Gioanni, Y., Dégénétais, E., & Glowinski, J. (2000). Hippocampo-prefrontal cortex pathway: anatomical and electrophysiological characteristics. *Hippocampus, 10*(4), 411-419. doi:10.1002/1098-1063(2000)10:4<411::Aid-hipo7>3.0.Co;2-a

Tipton, K. A., Verges, K. J., & Weissman, J. S. (2008). In vivo monitoring of the prion replication cycle reveals a critical role for Sis1 in delivering substrates to Hsp104. *Mol Cell, 32*(4), 584-591. doi:10.1016/j.molcel.2008.11.003

Toyama, B. H., Kelly, M. J., Gross, J. D., & Weissman, J. S. (2007). The structural basis of yeast prion strain variants. *Nature, 449*(7159), 233-237. doi:10.1038/nature06108

True, H. L., & Lindquist, S. L. (2000). A yeast prion provides a mechanism for genetic variation and phenotypic diversity. *Nature, 407*(6803), 477-483. doi:10.1038/35035005

Van der Perren, A., Gelders, G., Fenyi, A., Bousset, L., Brito, F., Peelaerts, W., . . . Baekelandt, V. (2020). The structural differences between patient-derived α-synuclein strains dictate characteristics of Parkinson's disease, multiple system atrophy and dementia with Lewy bodies. *Acta Neuropathol, 139*(6), 977-1000. doi:10.1007/s00401-020-02157-3

van Groen, T., Miettinen, P., & Kadish, I. (2003). The entorhinal cortex of the mouse: organization of the projection to the hippocampal formation. *Hippocampus, 13*(1), 133-149. doi:10.1002/hipo.10037

Varela, C., Kumar, S., Yang, J. Y., & Wilson, M. A. (2014). Anatomical substrates for direct interactions between hippocampus, medial prefrontal cortex, and the thalamic nucleus reuniens. *Brain Struct Funct, 219*(3), 911-929. doi:10.1007/s00429-013-0543-5

Vella, L. J., Sharples, R. A., Lawson, V. A., Masters, C. L., Cappai, R., & Hill, A. F. (2007). Packaging of prions into exosomes is associated with a novel pathway of PrP processing. *J Pathol, 211*(5), 582-590. doi:10.1002/path.2145

Venegas, C., Kumar, S., Franklin, B. S., Dierkes, T., Brinkschulte, R., Tejera, D., . . . Heneka, M. T. (2017). Microglia-derived ASC specks cross-seed amyloid-β in Alzheimer's disease. *Nature, 552*(7685), 355-361. doi:10.1038/nature25158

Wadsworth, J. D., & Collinge, J. (2007). Update on human prion disease. *Biochim Biophys Acta, 1772*(6), 598-609. doi:10.1016/j.bbadis.2007.02.010

Wakabayashi, K., Hayashi, S., Yoshimoto, M., Kudo, H., & Takahashi, H. (2000). NACP/alpha-synuclein-positive filamentous inclusions in astrocytes and oligodendrocytes of Parkinson's disease brains. *Acta Neuropathol, 99*(1), 14-20. doi:10.1007/pl00007400

Wang, F., Wang, X., Yuan, C. G., & Ma, J. (2010). Generating a prion with bacterially expressed recombinant prion protein. *Science, 327*(5969), 1132-1135. doi:10.1126/science.1183748

Wang, Y., & Mandelkow, E. (2016). Tau in physiology and pathology. *Nat Rev Neurosci, 17*(1), 5-21. doi:10.1038/nrn.2015.1

Weissmann, C., Enari, M., Klöhn, P. C., Rossi, D., & Flechsig, E. (2002). Transmission of prions. *Proc Natl Acad Sci U S A, 99 Suppl 4*(Suppl 4), 16378-16383. doi:10.1073/pnas.172403799

Wentink, A. S., Nillegoda, N. B., Feufel, J., Ubartaitė, G., Schneider, C. P., De Los Rios, P., . . . Bukau, B. (2020). Molecular dissection of amyloid disaggregation by human HSP70. *Nature, 587*(7834), 483-488. doi:10.1038/s41586-020-2904-6

Westermark, P. (2005). Aspects on human amyloid forms and their fibril polypeptides. *Febs j, 272*(23), 5942-5949. doi:10.1111/j.1742-4658.2005.05024.x

Wickner, R. B. (1994). [URE3] as an altered URE2 protein: evidence for a prion analog in Saccharomyces cerevisiae. *Science, 264*(5158), 566-569. doi:10.1126/science.7909170

Wickner, R. B., Dyda, F., & Tycko, R. (2008). Amyloid of Rnq1p, the basis of the [PIN+] prion, has a parallel in-register beta-sheet structure. *Proc Natl Acad Sci U S A, 105*(7), 2403-2408. doi:10.1073/pnas.0712032105

Wilson, D. M., 3rd, Cookson, M. R., Van Den Bosch, L., Zetterberg, H., Holtzman, D. M., & Dewachter, I. (2023). Hallmarks of neurodegenerative diseases. *Cell, 186*(4), 693-714. doi:10.1016/j.cell.2022.12.032

Winner, B., Jappelli, R., Maji, S. K., Desplats, P. A., Boyer, L., Aigner, S., . . . Riek, R. (2011). In vivo demonstration that alpha-synuclein oligomers are toxic. *Proc Natl Acad Sci U S A, 108*(10), 4194-4199. doi:10.1073/pnas.1100976108

Wong, Y. C., & Krainc, D. (2017). α-synuclein toxicity in neurodegeneration: mechanism and therapeutic strategies. *Nat Med, 23*(2), 1-13. doi:10.1038/nm.4269

Wulf, M. A., Senatore, A., & Aguzzi, A. (2017). The biological function of the cellular prion protein: an update. *BMC Biol, 15*(1), 34. doi:10.1186/s12915-017-0375-5

Wyss, J. M., & Van Groen, T. (1992). Connections between the retrosplenial cortex and the hippocampal formation in the rat: a review. *Hippocampus, 2*(1), 1-11. doi:10.1002/hipo.450020102

Wyss-Coray, T. (2016). Ageing, neurodegeneration and brain rejuvenation. *Nature, 539*(7628), 180-186. doi:10.1038/nature20411

Xue, C., Lin, T. Y., Chang, D., & Guo, Z. (2017). Thioflavin T as an amyloid dye: fibril quantification, optimal concentration and effect on aggregation. *R Soc Open Sci, 4*(1), 160696. doi:10.1098/rsos.160696

Yang, Y., Shi, Y., Schweighauser, M., Zhang, X., Kotecha, A., Murzin, A. G., . . . Goedert, M. (2022). Structures of α-synuclein filaments from human brains with Lewy pathology. *Nature, 610*(7933), 791-795. doi:10.1038/s41586-022-05319-3

Yoshiyama, Y., Higuchi, M., Zhang, B., Huang, S. M., Iwata, N., Saido, T. C., . . . Lee, V. M. (2007). Synapse loss and microglial activation precede tangles in a P301S tauopathy mouse model. *Neuron, 53*(3), 337-351. doi:10.1016/j.neuron.2007.01.010

Yun, S. P., Kam, T. I., Panicker, N., Kim, S., Oh, Y., Park, J. S., . . . Ko, H. S. (2018). Block of A1 astrocyte conversion by microglia is neuroprotective in models of Parkinson's disease. *Nat Med, 24*(7), 931-938. doi:10.1038/s41591-018-0051-5

Zhang, D., Hu, X., Qian, L., O'Callaghan, J. P., & Hong, J. S. (2010). Astrogliosis in CNS pathologies: is there a role for microglia? *Mol Neurobiol, 41*(2-3), 232-241. doi:10.1007/s12035-010-8098-4

Zhang, H., Cao, Y., Ma, L., Wei, Y., & Li, H. (2021). Possible Mechanisms of Tau Spread and Toxicity in Alzheimer's Disease. *Front Cell Dev Biol, 9*, 707268. doi:10.3389/fcell.2021.707268

Zhang, J., Hu, Y., Hau, R., Musharrafieh, R., Ma, C., Zhou, X., . . . Wang, J. (2019). Identification of NMS-873, an allosteric and specific p97 inhibitor, as a broad antiviral against both influenza A and B viruses. *Eur J Pharm Sci, 133*, 86-94. doi:10.1016/j.ejps.2019.03.020

Zhang, W., Tarutani, A., Newell, K. L., Murzin, A. G., Matsubara, T., Falcon, B., . . . Scheres, S. H. W. (2020). Novel tau filament fold in corticobasal degeneration. *Nature, 580*(7802), 283-287. doi:10.1038/s41586-020-2043-0

Zhang, Y., Chen, K., Sloan, S. A., Bennett, M. L., Scholze, A. R., O'Keeffe, S., . . . Wu, J. Q. (2014). An RNA-sequencing transcriptome and splicing database of glia, neurons, and vascular cells of the cerebral cortex. *J Neurosci, 34*(36), 11929-11947. doi:10.1523/jneurosci.1860-14.2014

Zhang, Z., Zhang, Y., Wang, F., Wang, X., Xu, Y., Yang, H., . . . Ma, J. (2013). De novo generation of infectious prions with bacterially expressed recombinant prion protein. *Faseb j, 27*(12), 4768-4775. doi:10.1096/fj.13-233965

Zheng, Q., Huang, T., Zhang, L., Zhou, Y., Luo, H., Xu, H., & Wang, X. (2016). Dysregulation of Ubiquitin-Proteasome System in Neurodegenerative Diseases. *Front Aging Neurosci, 8*, 303. doi:10.3389/fnagi.2016.00303

Zhu, J., Pittman, S., Dhavale, D., French, R., Patterson, J. N., Kaleelurrrahuman, M. S., . . . Weihl, C. (2022). VCP suppresses proteopathic seeding in neurons. *Mol Neurodegener, 17*(1), 30. doi:10.1186/s13024-022-00532-0

Appendix
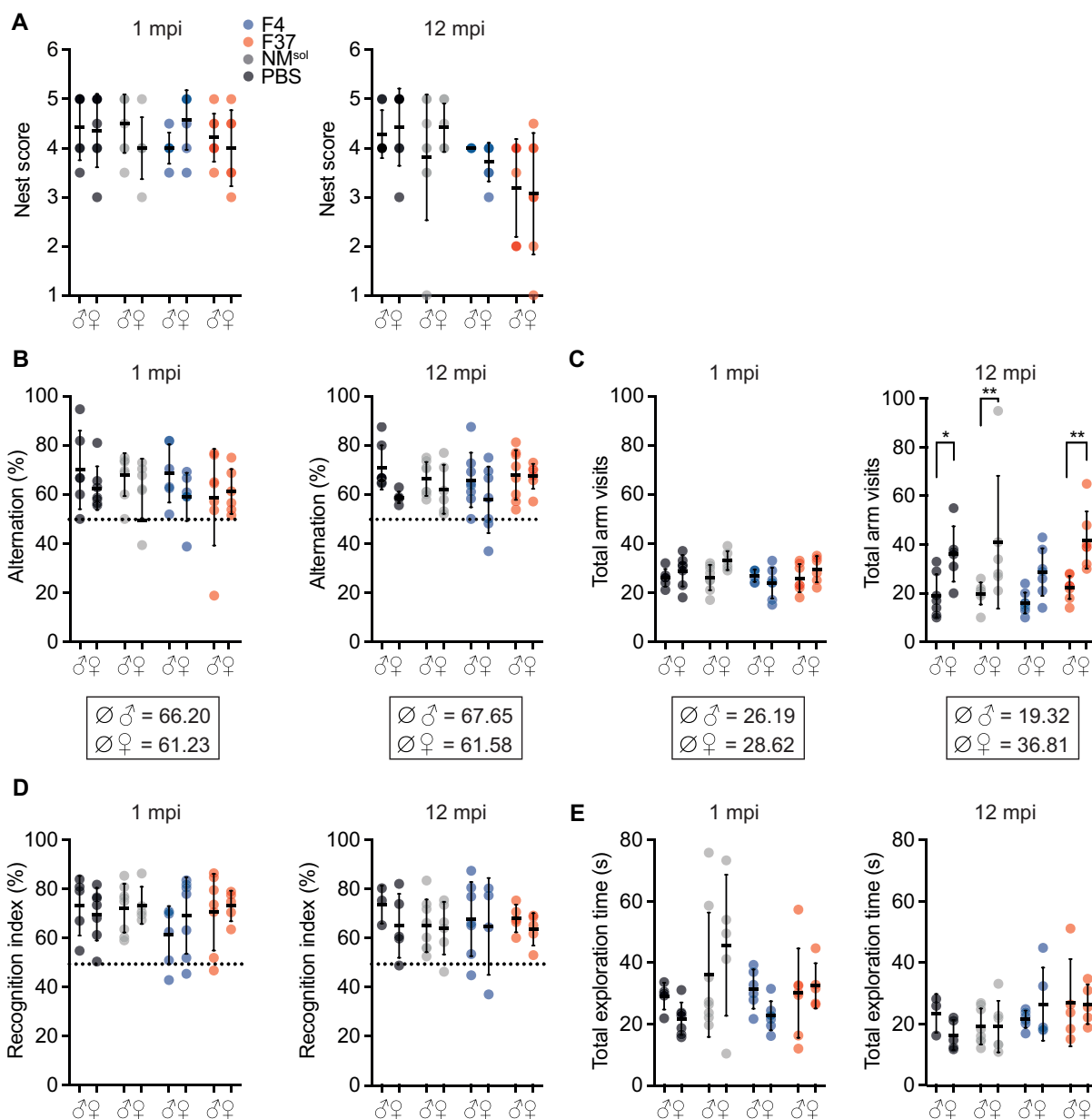
Supplementary figure 1. **Male and female mice behave similar in cognition tests. A** No difference in nest scores of injected male and female NM-HA animals at 1 mpi (left panel) and at 12 mpi (right panel). **B** The alternation rate of males and females in the Y maze was equal at 1 mpi and 12 mpi. The average alternation rate is indicated below graphs. **C** At 1 mpi, the count of total arm visits did not differ between males and females. At 12 mpi, females increased in explorative behavior and visited the arms more often. Males showed decreased explorative behavior at 12 mpi. The average count of total arm visits is indicated below graphs. **D, E** In the novel object recognition test, males and females showed equal ability to recognize the new object and explored the objects equally long. **A-E** 6-8 male and female animals were tested per condition. Data are shown as means ± SD, two-way ANOVA with Bonferroni multiple comparison test. Only significant differences are indicated. *P < 0.0332, **P < 0.0021, ***P < 0.0002, ****P < 0.0001. Dashed lines indicate the chance level.
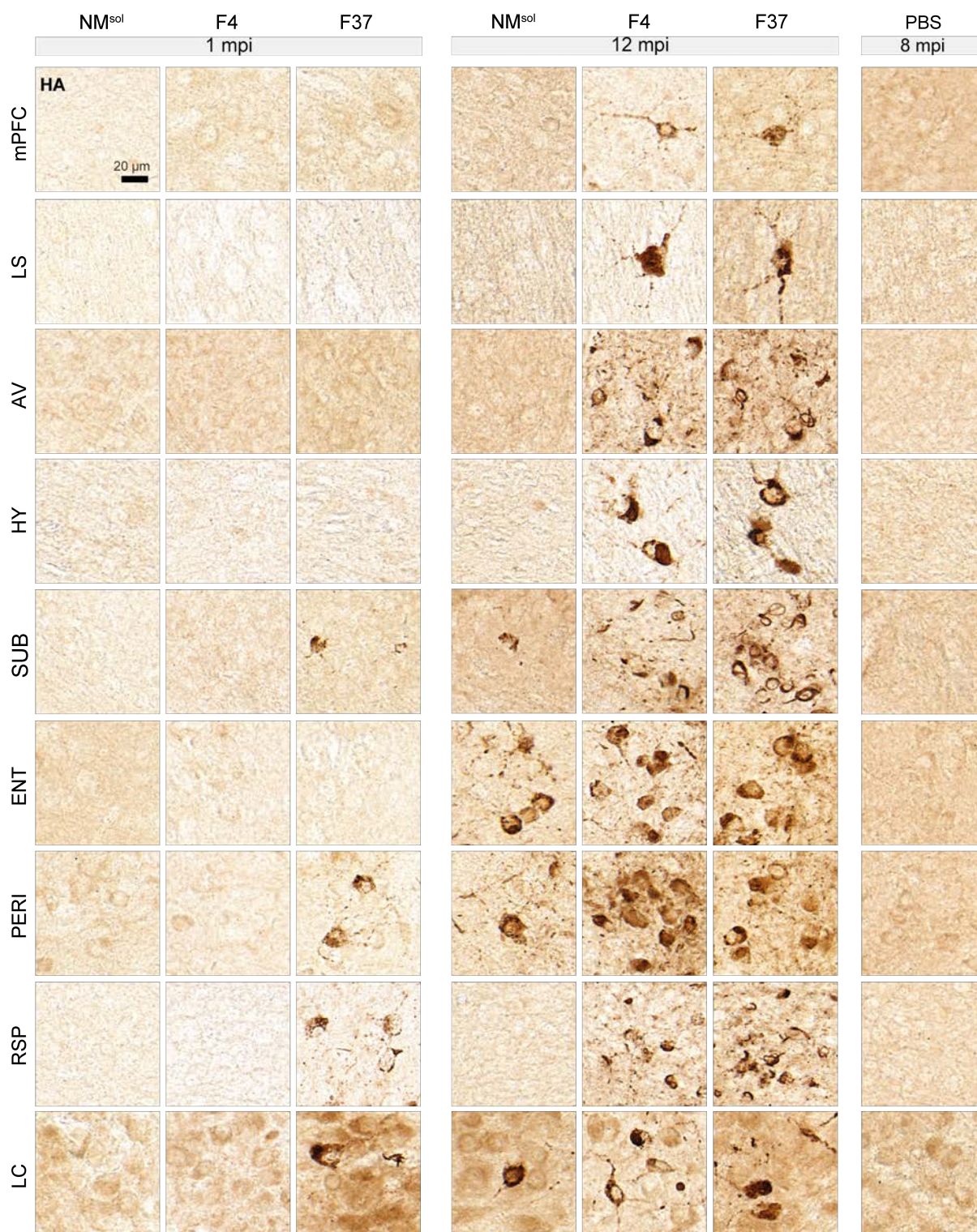
Supplementary figure 2. NM-HA deposits in various brain regions of injected animals. A Representative images of NM-HA aggregates in numerous brain regions from animals injected with F4, F37 and NM^sol at 1 mpi (left) and 12 mpi (middle). Animals injected with PBS served as negative control (right). Brain sections were immunohistochemically stained with anti-HA antibodies.
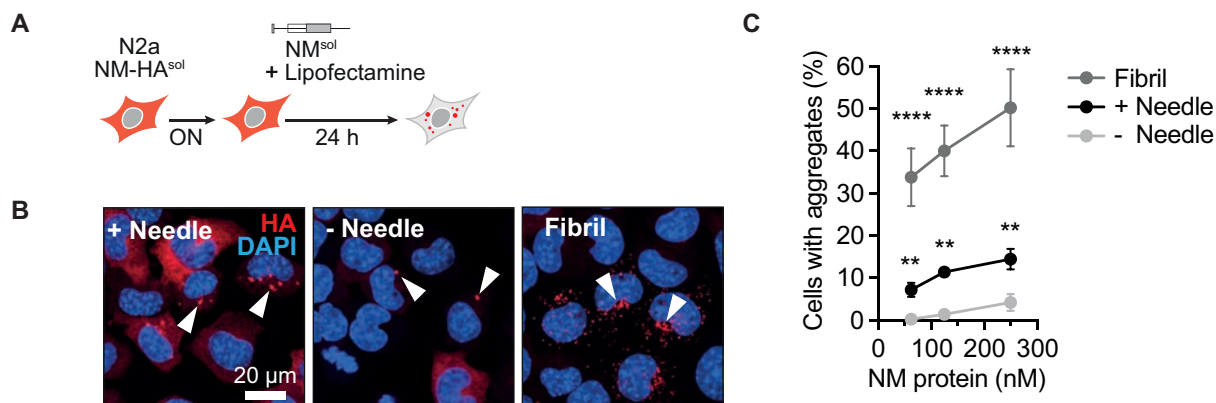
Supplementary figure 3. Recombinant NM processed for injection seeds aggregation in cells. A Experimental design. The procedure of NM monomer preparation for mouse injection was reproduced by forcing monomeric NM through a glass capillary at a speed of 100 nl/min. After an incubation at RT for 90 min, needle-treated and untreated NM was mixed with lipofectamine and added to N2a NM-HA^{sol} cells. **B** Representative confocal images of N2a cells with induced NM-HA aggregates upon exposure to 250 nM (monomer equivalent) soluble NM or NM fibrils (positive control) with and without shearing through the injection capillary. Arrowheads indicate intracellular NM-HA aggregates detected using anti-HA antibodies. **C** Capillary-processed NM induces NM-HA aggregation. Percentage of cells with seeded NM-HA aggregates following exposure to different concentrations of NM fibril or monomer. Data are shown as means ± SD, two-way ANOVA with Tukey's multiple comparison test. 4 replicates are shown. Asterisks indicate comparison to "- Needle" group. **P < 0.0021, ****P < 0.0001.

A

B

Left panel
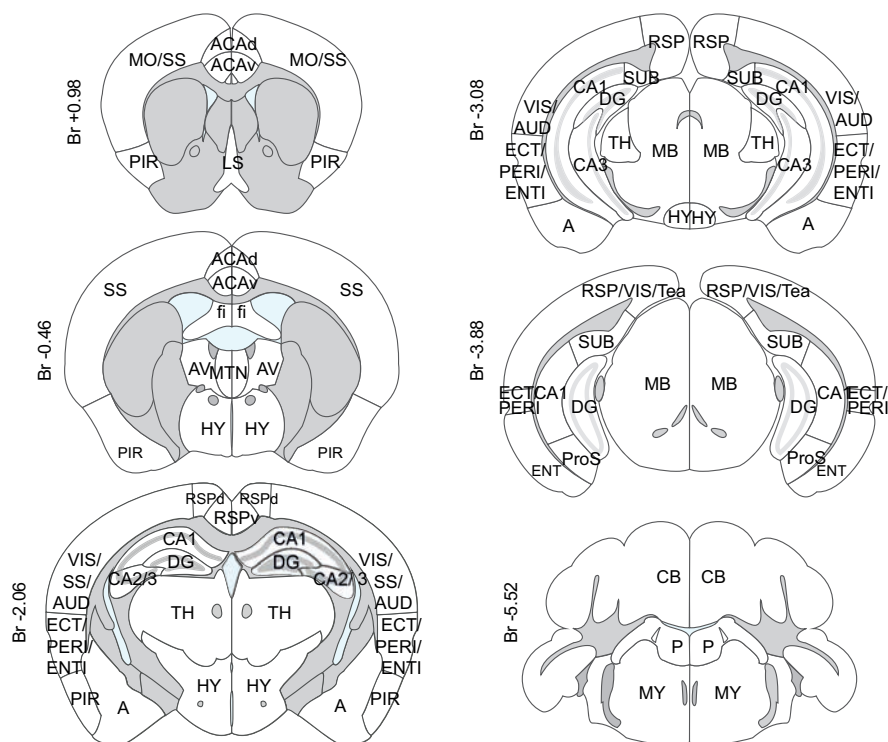
|	1 mpi NM^sol	1 mpi F4	1 mpi F37	12 mpi NM^sol	12 mpi F4	12 mpi F37
Br +0.98						
ACAv	0.219	0.111	0.194	0.259	0.295	0.472
ACAd	0.069	0.046	0.037	0.145	0.054	0.086
MO/SS	0.017	0.032	0.033	0.045	0.028	0.029
PIR	0.023	0.012	0.048	0.092	0.036	0.070
LS	0.036	0.101	0.194	0.261	0.293	0.570
ACAv	0.180	0.055	0.246	0.218	2.920	3.102
ACAd	0.166	0.054	0.117	0.169	0.851	0.551
MO/SS	0.024	0.022	0.041	0.075	0.093	0.080
PIR	0.039	0.043	0.094	0.239	0.190	0.095
LS	0.097	0.108	0.167	0.248	0.994	0.854
Br -0.46						
ACAv	0.183	0.125	0.181	0.170	1.200	1.064
ACAd	0.043	0.033	0.065	0.137	0.461	0.508
SS	0.039	0.037	0.050	0.078	0.077	0.166
fi	0.465	0.514	0.812	0.758	1.954	2.214
HY	0.186	0.658	0.485	0.253	0.385	0.860
MTN	0.073	0.577	0.241	0.132	0.278	0.384
PIR	0.127	0.085	0.064	0.066	0.041	0.097
AV	0.051	0.081	0.149	0.117	0.077	0.136
ACAv	0.184	0.161	0.214	0.198	2.670	3.662
ACAd	0.057	0.043	0.105	0.099	1.684	3.238
SS	0.036	0.049	0.061	0.069	0.195	0.379
fi	0.616	0.647	1.109	0.800	2.948	3.230
HY	0.186	0.580	0.511	0.279	0.390	0.876
MTN	0.056	0.615	0.312	0.194	0.488	0.685
PIR	0.038	0.028	0.055	0.107	0.181	0.161
AV	0.048	0.241	0.252	0.062	6.780	10.667
Br -2.06						
RSPv	0.065	0.017	0.070	0.140	1.300	0.867
RSPd	0.043	0.020	0.042	0.038	0.593	0.547
VIS/SS/AUD	0.014	0.020	0.125	0.058	0.947	0.507
A	0.027	0.053	0.078	0.078	0.150	0.042
CA1	0.088	0.033	0.131	0.133	3.652	2.644
CA3	0.018	0.045	0.652	0.172	9.299	6.145
DG	0.032	0.034	0.184	0.606	4.991	2.113
ECT/PERI/ENTI	0.032	0.024	0.268	0.145	0.931	0.274
HY	0.106	0.112	0.142	0.174	0.142	0.105
PIR	0.013	0.005	0.061	0.052	0.029	0.029
TH	0.066	0.042	0.053	0.079	0.074	0.048
RSPv	0.095	0.138	0.081	0.320	5.241	5.087
RSPd	0.097	0.007	0.510	0.074	4.999	4.696
VIS/SS/AUD	0.041	0.110	0.708	0.111	3.293	2.779
A	0.023	0.030	0.066	0.050	1.124	0.312
CA1	0.074	1.279	7.927	0.445	16.793	12.283
CA3	0.014	1.901	6.308	0.352	22.602	24.002
DG	0.110	5.015	15.924	1.385	17.410	13.006
ECT/PERI/ENTI	0.025	0.048	0.491	0.178	1.448	0.719
HY	0.066	0.118	0.151	0.108	0.187	0.194
PIR	0.021	0.021	0.046	0.143	0.529	0.335
TH	0.069	0.042	0.083	0.076	0.182	0.301

Right panel

|	1 mpi NM^sol	1 mpi F4	1 mpi F37	12 mpi NM^sol	12 mpi F4	12 mpi F37
Br -3.08						
RSP	0.041	0.032	0.103	0.066	1.813	2.243
VIS/AUD	0.191	0.035	0.144	0.062	1.707	0.528
ECT/PERI/ENTI	0.167	0.052	0.107	0.067	0.401	0.282
A	0.107	0.050	0.093	0.091	0.112	0.096
CA1	0.050	0.045	0.069	0.049	0.217	0.237
CA3	0.038	0.021	0.113	0.054	2.709	3.077
DG	0.036	0.044	0.267	0.578	9.805	5.188
HY	0.055	0.183	0.145	0.121	0.321	0.807
MB	0.061	0.081	0.135	0.090	0.096	0.159
SUB	0.022	0.222	0.483	0.053	1.684	1.262
TH	0.058	0.600	0.347	0.147	0.404	0.261
RSP	0.048	0.154	0.941	0.133	12.972	13.723
VIS/AUD	0.055	0.017	0.201	0.044	4.546	2.101
ECT/PERI/ENTI	0.045	0.053	0.183	1.191	6.402	5.953
A	0.050	0.077	0.122	0.118	0.112	0.199
CA1	0.054	0.037	0.564	0.058	1.559	3.040
CA3	0.016	0.103	2.485	0.027	4.325	8.050
DG	0.141	1.357	11.008	0.772	18.314	19.272
HY	0.100	0.123	0.208	0.134	0.925	1.835
MB	0.075	0.103	0.132	0.096	0.228	0.205
SUB	0.087	2.443	7.841	0.827	22.100	17.826
TH	0.102	0.672	0.386	0.126	0.296	0.317
Br -3.88						
RSP/VIS/Tea	0.075	0.031	0.112	0.056	0.962	0.649
ProS	0.153	0.036	0.115	0.060	0.108	0.056
CA1	0.231	0.131	0.133	0.083	0.191	0.172
DG	0.050	0.075	0.334	0.475	5.357	8.168
ECT/PERI	0.190	0.152	0.268	0.196	1.974	1.628
ENT	0.117	0.189	0.116	0.059	0.124	0.254
MB	0.090	0.098	0.147	0.142	0.100	0.091
SUB	0.034	0.202	0.122	0.144	1.686	1.391
RSP/VIS/Tea	0.048	0.035	0.193	0.066	3.483	4.447
ProS	0.115	0.059	0.256	0.060	0.200	0.172
CA1	0.052	0.106	0.475	0.130	1.284	2.065
DG	0.033	0.200	3.049	1.095	13.437	16.971
ECT/PERI	0.079	0.028	0.810	1.928	14.629	8.841
ENT	0.035	0.035	0.149	0.933	1.685	3.717
MB	0.070	0.077	0.127	0.114	0.143	0.126
SUB	0.044	0.185	0.700	0.229	8.359	19.256
Br -5.52						
CB	0.050	0.031	0.056	0.162	0.047	0.070
MY	0.084	0.046	0.117	0.164	0.089	0.096
P	0.134	0.141	0.266	0.244	0.193	0.263
CB	0.039	0.046	0.085	0.148	0.058	0.054
MY	0.063	0.044	0.069	0.147	0.077	0.079
P	0.132	0.147	0.387	0.335	0.465	0.611

Aggregate area fraction [‰] 5 10 15 20 25

Supplementary figure 4. Quantification of NM-HA aggregates in the mouse brain. A Designation of analyzed brain regions (white) defined in each coronal section according to the Allen Reference Atlas – Mouse Brain (atlas.brain-map.org). The position of each coronal section is given in mm relative to Bregma. Ventricles are coloured in blue, grey regions were excluded from analysis. **B** Quantification of NM-HA aggregates in defined

brain regions 1 mpi and 12 mpi. Values represent the mean from 4-5 analyzed animals. Values < 0.3 are shown in white. The names of contralateral and ipsilateral brain regions are written in light grey and black. A: amygdala, ACAd/v: dorsal/ ventral anterior cingulate cortex, AUD: auditory cortex, AV: anteroventral nucleus of thalamus, CA1: cornu ammonis 1, CA3: cornu ammonis 3, CB: cerebellum, DG: dentate gyrus, ECT: ectorhinal area, ENT: entorhinal cortex, fi: fimbria, HY: hypothalamus, LS: lateral septal nucleus, MB: midbrain, MO: motor cortex, MSC: medial septal complex, MTN: Midline group of the dorsal thalamus, MY: Medulla, P: Pons, PERI: Perirhinal area, PIR: Piriform area, ProS: prosubiculum, RSPd/v: dorsal/ ventral retrosplenial cortex, RT: reticular nucleus of thalamus, SS: somatosensory cortex, SUB: subiculum, Tea: temporal association cortex, TH: thalamus, VIS: visual cortex.

A

LS ipsi
Br. +0.98

ACA ipsi
Br. -0.46

AV ipsi
Br. -0,46

HY ipsi
Br. -3.08

RSP ipsi
Br. -3.08

F4
F37
NM^sol

ECT/ PERI ipsi
Br. -3.88

SUB ipsi
Br. -3.88

ENT ipsi
Br.-3.88

P ipsi
Br.-5.52

B

LS contra
Br. +0.98

ACA contra
Br.- 0.46

AV contra
Br. -0,46

CA1 contra
Br. -2.06

CA2/3 contra
Br. -2.06

DG contra
Br. -2.06

HY contra
Br. -3.08

RSP contra
Br. -3.08

ECT/ PERI contra
Br. -3.88

SUB contra
Br. -3.88

ENT contra
Br.-3.88
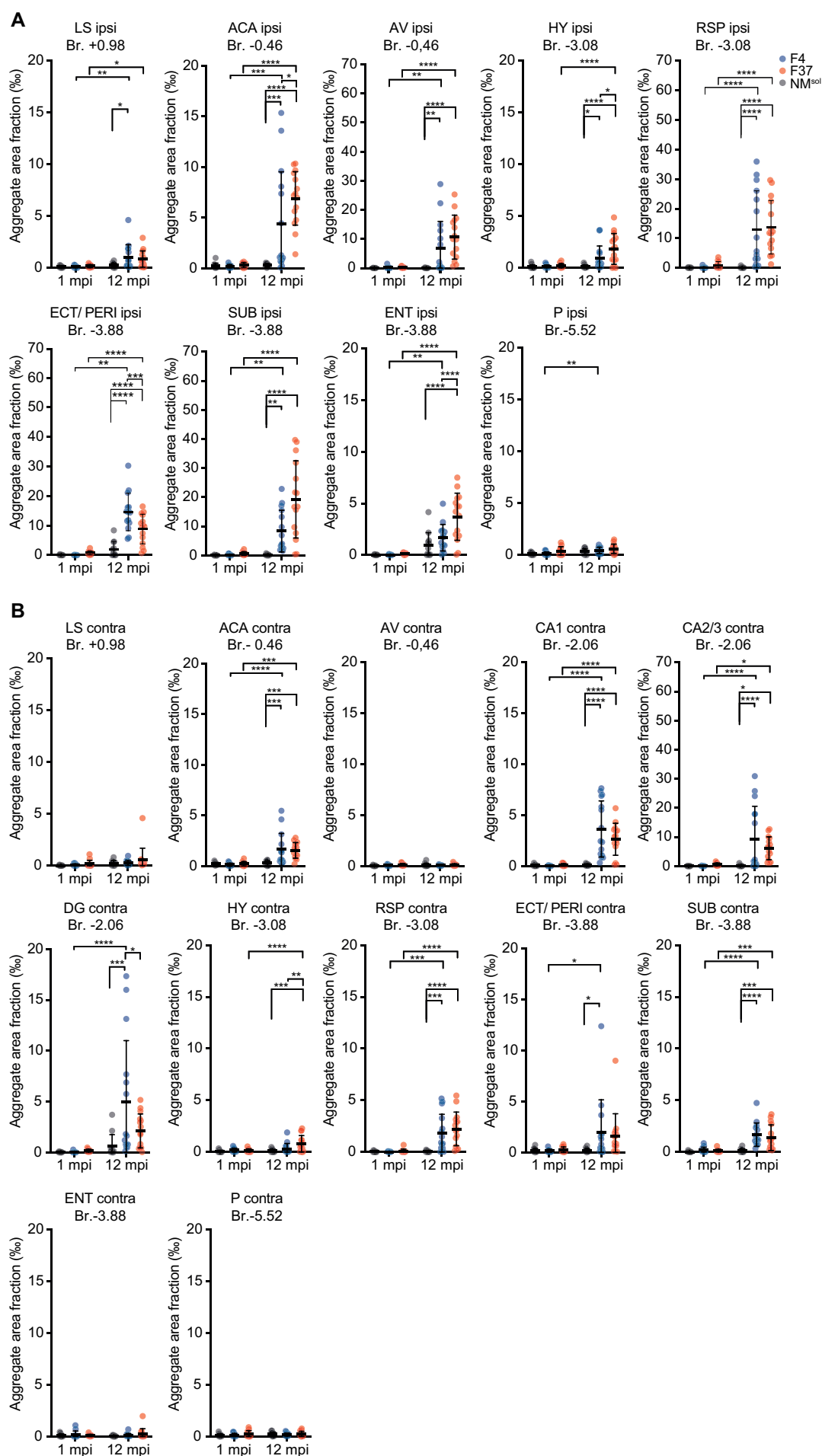
P contra
Br.-5.52

Supplementary figure 5. Quantification of F4 and F37-induced NM-HA pathology in different brain regions.
NM-HA aggregate quantification in selected ipsilateral (**A**) and contralateral (**B**) brain regions at 1 mpi and 12 mpi. Data are shown as means ± SD, 3 sections/ animal, n= 4-5 animals/ condition. Two-way ANOVA with Tukey post-hoc test. Significant changes are indicated *P < 0.0332, ** P < 0.0021, ***P < 0.0002, ****P < 0.0001. ACA: anterior cingulate cortex, AV: anteroventral nucleus of thalamus, CA1-3: cornu ammonis 1-3, DG: dentate gyrus, ECT: ectorhinal area, ENT: entorhinal cortex, HY: hypothalamus, LS: lateral septal nucleus, P: pons, PERI: perirhinal area, RSP: retrosplenial cortex, SUB: subiculum.
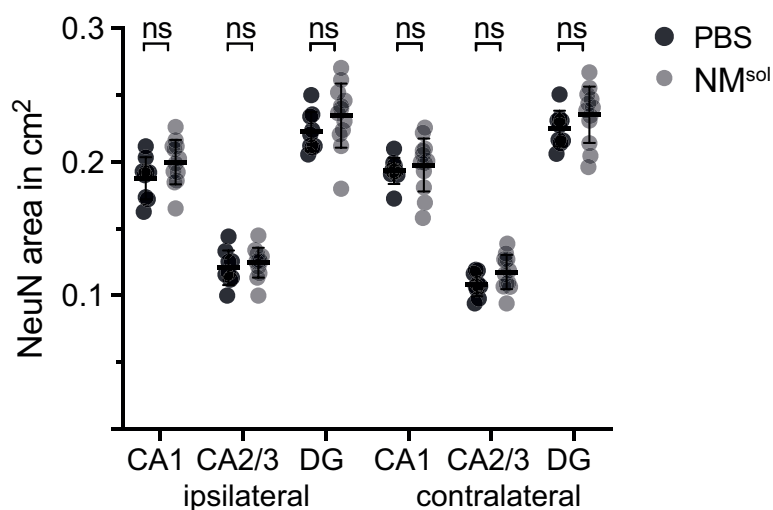
Supplementary figure 6. Injection of soluble NM and PBS has no effect on hippocampal neurons 12 mpi.
Quantification of NeuN-positive area in hippocampal CA1, CA3, and DG after injection of soluble NM (NM^{sol}) and PBS. Data are shown as means ± SD, n= 4-5 animals/ condition, 3 sections/ animal, two-way ANOVA with Tukey post-hoc test. ns indicates p > 0.05. mpi: months post injection. CA1-3: cornu ammonis 1-3, DG: dentate gyrus.
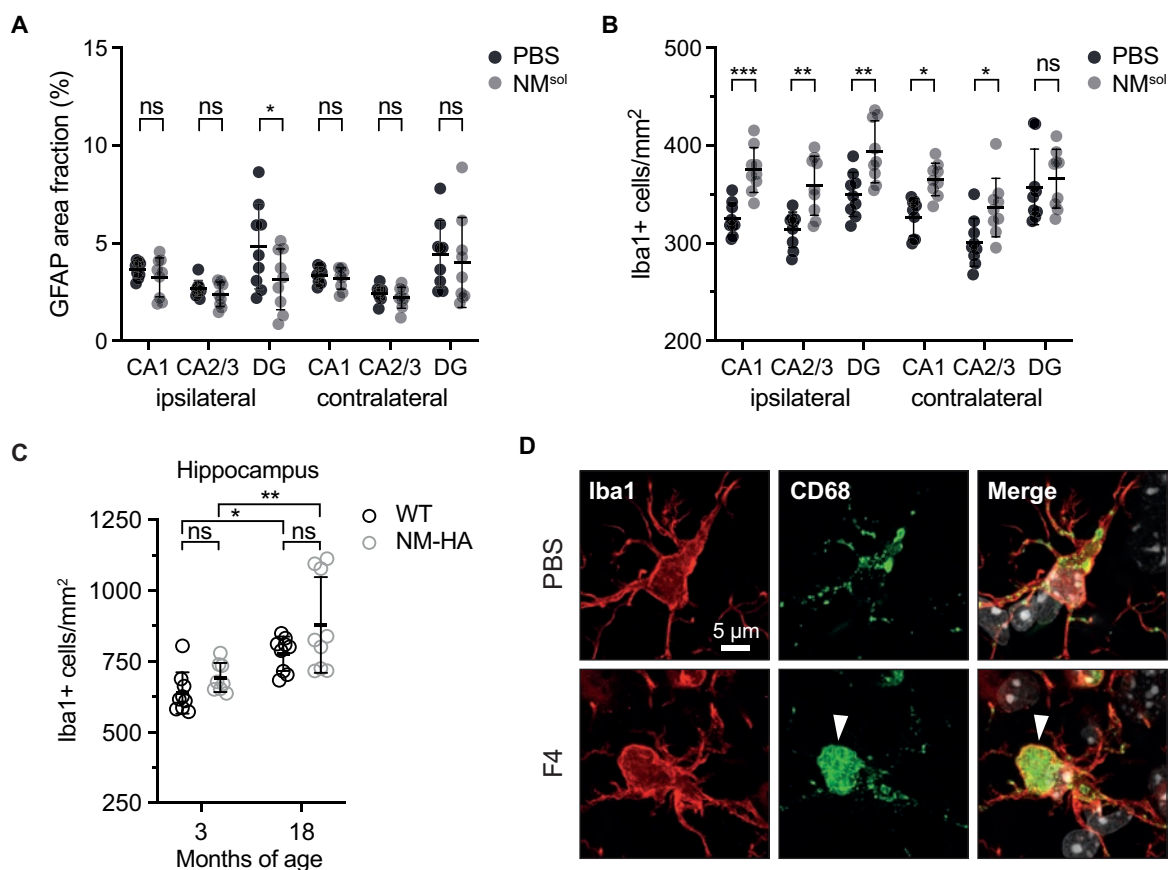
Supplementary figure 7. Activated microglia in fibril-injected animals. A No changes in astroglial activation upon PBS and NM injection after 12 months. Brain sections were stained with astroglial marker GFAP. GFAP-positive area was automatically quantified and normalized to the area of the brain region. **B** Quantification of microglia in the hippocampus of PBS and NM^{sol}-injected animals revealed increased microglia numbers upon NM injection after 12 months. In a separate control experiment, brain sections were stained with Iba1 and microglia were automatically quantified. **C** Untreated WT and NM-HA animals show similar increase in microglia numbers during aging. Microglia were quantified as described in **B** in the full hippocampus at 3 months and 18 months of age. **D** Representative images of brain sections stained with microglial marker Iba1 and CD68 associated with phagocytically active microglia. Microglia were imaged in the ipsilateral CA1 region. **A, B, C** 3 sections per animal were analyzed from 3 animals per condition. Data are shown as means ± SD, two-way ANOVA with Bonferroni multiple comparison test. ns indicates $p > 0.05$, *$P < 0.0332$, ** $P < 0.0021$, ***$P < 0.0002$. CA1-3: cornu ammonis 1-3, DG: dentate gyrus.